

# **An Artificial Rubidium Atom**

## **Inauguraldissertation**

zur  
Erlangung der Würde eines Doktors der Philosophie  
vorgelegt der  
Philosophisch-Naturwissenschaftlichen Fakultät  
der Universität Basel

von

**Jan-Philipp Jahn**

aus Deutschland

Basel, 2018

The original document is saved on the university of Basel document server  
<http://edoc.unibas.ch>



This work is licensed under a Creative Commons  
Attribution-NonCommercial-NoDerivatives 4.0 International License.

The complete text may be reviewed here:

<http://creativecommons.org/licenses/by-nc-nd/4.0/>

Genehmigt von der Philosophisch-Naturwissenschaftlichen Fakultät  
auf Antrag von  
Prof. Dr. Richard J. Warburton  
Prof. Dr. Armando Rastelli

Basel, den 26. Juni 2018

Prof. Dr. Martin Spiess  
Dekan

# Preface

Harnessing quantum mechanics to revolutionize various fields of established technology has fueled research activities in recent years. Especially the prospect of inherently secure quantum communication channels has become increasingly desirable to businesses, politicians and society as a whole to protect sensitive information.

At heart, quantum communication relies on the distribution of entangled quantum states that make the communication impervious to eavesdroppers. Naturally single photons or photon pairs are an excellent choice for distributing entangled states at the speed-of-light through existing fiber-networks [1].

One of the most promising quantum light sources constitute epitaxial quantum dots [2, 3, 4, 5]. The high oscillator strength renders them exceptionally bright, while still emitting nearly indistinguishable single photons with quantum efficiencies close to unity, an important prerequisite for high-fidelity photonic quantum applications [6, 7]. By carefully manufacturing the semiconductor hetero-structure, the optical environment can be individually tailored, utilizing Purcell enhancement, by embedding the emitter in a semiconductor cavity or exploiting wave guiding properties in form of micropillars or nanowires to enhance the extraction efficiency [6, 8].

Inevitable optical attenuation in fiber networks however necessitates the overall communication channel length to be divided into subsections with nodes that can temporarily store the quantum information [9, 10]. Naturally this requires a quantum memory which can efficiently store the quantum state for a sufficiently long time and subsequently recreate the stored photon on demand [11].

In this framework, atomic memories represent the established benchmark, unrivaled by quantum dots spin states which remain intrinsically limited by the decoherence-inducing interaction with the solid state environment [12, 13]. Combining the excellent single-photon source of a quantum dot with the superior coherence properties of alkali quantum memories in a hybrid system at each quantum node offers the best of both worlds, promising exponential speed-up of truly secure communication [10, 11, 13].

---

This PhD thesis focuses on the requirements imposed on the quantum dot in such a hybrid quantum network and shows how these challenges can be overcome.

The first part of the introduction aims to give a detailed overview on the underlying quantum communication protocol of a hybrid quantum network and how it fares against the more established DLCZ protocol. Next, single-photon sources, and quantum dots in particular, will be outlined and the growth mechanism and optical properties of epitaxial GaAs quantum dots discussed in detail. Lastly, to illustrate the framework in which a quantum dot can efficiently be paired with alkali atoms and to understand the challenges that arise, the mode of operation and attributes of the state-of-art broadband quantum memory will be summarized in chapter 2.

The third chapter investigates the optical properties of an epitaxial GaAs quantum dot spectrally matched to rubidium. By means of strain-tuning, the quantum dot can address all hyperfine transitions of the rubidium D2 line and a first interaction with atomic vapors is shown in a transmission measurement. In conjunction with other optical measurements, true Fourier-limited emission of single photons is demonstrated. Furthermore, we establish a possible route to overcome the bandwidth mismatch of the two systems in form of the coherent-scattering regime.

While this coherent-scattering regime offers quantum dot single-photons with sub-natural bandwidths, in form of elastically scattered single photons that predominately retain the small linewidth of the excitation laser, the emission is highly probabilistic and relies on continuous-wave excitation or weak, resonant laser pulses of durations exceeding the exciton lifetime [14]. The fourth chapter demonstrates the generation of true on-demand single-photons with tailored temporal waveform envelopes between 14 and 245 ns, overcoming the temporal limitations imposed by the exciton two-level system. The photonic bandwidth is reduced by almost one order of magnitude.

In the following, the decay dynamics of a positively charged exciton in an GaAs quantum dot will be investigated by time-resolved photoluminescence and resonance fluorescence measurements (chapter 5). In Chapter 6 the optical properties of GaAs quantum dots in 500 nm thick membranes are characterized. Finally, an outlook into future developments and the solutions to remaining challenges will be presented.



# Contents

<b>1</b>	<b>Introduction</b>	<b>1</b>
1.1	A Hybrid approach to Quantum Communication . . . . .	1
1.2	Single photon sources . . . . .	8
1.2.1	Quantum dots . . . . .	10
1.2.2	Growth of epitaxial GaAs quantum dots . . . . .	11
1.2.3	Level structure of epitaxial GaAs quantum dots . . . . .	12
1.2.4	Single photon emission from a quantum dot . . . . .	16
1.2.5	A quantum dot exciton as a two level system . . . . .	18
<b>2</b>	<b>Interfacing GaAs quantum dots and atomic quantum memories</b>	<b>23</b>
2.1	Simple atomic quantum memory suitable for semiconductor quantum dot single photons . . . . .	24
2.2	Prospect of quantum dot single photon storage in the atomic quantum memory	30
<b>3</b>	<b>An artificial Rb atom in a semiconductor with lifetime-limited linewidth</b>	<b>31</b>
3.1	Summary . . . . .	31
3.2	Introduction . . . . .	32
3.3	Sample . . . . .	33
3.4	Resonance fluorescence on a single QD . . . . .	34
3.5	Spectroscopy of the Rubidium atomic ensemble with QD photons . . . . .	36
3.6	Blinking in the QD signal . . . . .	39
3.7	Conclusion . . . . .	40
3.8	Appendix A: Vapor cell absorption spectrum . . . . .	42
3.8.1	Theory . . . . .	42
3.8.2	Experiment . . . . .	43
3.9	Appendix B: Theory of the QD response to a resonant field . . . . .	43
3.9.1	First order coherence $g^{(1)}(\tau)$ and power spectrum $S(\omega_{sc})$ . . . . .	43

3.9.2	Second order coherence $g_{\text{TLS}}^{(2)}(\tau)$ . . . . .	46
3.10	Appendix C: Experimental determination of the QD spontaneous emission rate and dephasing rate . . . . .	46
3.10.1	Results from the resonant excitation . . . . .	46
3.10.2	Decay-time measurements under non-resonant excitation . . . . .	48
3.11	Appendix D: Complementary information on the blinking in the QD signal . . . . .	49
3.11.1	QD1 second order correlation function at long delays . . . . .	49
3.11.2	Effect of the non-resonant contribution on the RF signal . . . . .	50
<b>4</b>	<b>On-demand semiconductor source of 780-nm single photons with controlled temporal wave packets</b>	<b>53</b>
4.1	Abstract . . . . .	53
4.2	Introduction . . . . .	54
4.3	Scheme . . . . .	56
4.4	Experimental setup and methods . . . . .	57
4.5	QD spin dynamics . . . . .	58
4.6	Raman single-photon pulse shaping . . . . .	61
4.7	Spectral properties of Raman photons . . . . .	64
4.8	Conclusion and outlook . . . . .	65
<b>5</b>	<b>Exciton decay dynamics of a positively charged exciton <math>X^+</math> in an epitaxial GaAs quantum dot in pulsed resonant and above-band excitation</b>	<b>67</b>
5.1	Experimental setup and methods . . . . .	69
5.2	Decay dynamics . . . . .	70
5.3	Conclusion and Outlook . . . . .	75
<b>6</b>	<b>GaAs quantum dots in a membrane</b>	<b>77</b>
<b>7</b>	<b>Outlook: Tuning of the quantum dot emission energy</b>	<b>83</b>
7.1	A simple low-voltage high-strain tuning device . . . . .	83
7.2	Charge tuning in a GaAs QD . . . . .	86
<b>8</b>	<b>Outlook: Enhancing the outcoupling efficiency of quantum dot photons</b>	<b>91</b>
<b>9</b>	<b>Conclusion and Outlook</b>	<b>95</b>
	<b>Bibliography</b>	<b>103</b>
	<b>Curriculum Vitae</b>	<b>119</b>

# Chapter 1

## Introduction

### 1.1 A Hybrid approach to Quantum Communication

Quantum entanglement at first glance appears to defy all logic and even infamously puzzled the minds of Einstein, Podolski and Rosen. They drew the conclusion that quantum mechanics had to be incomplete and “local hidden variables” were at play, which predetermine the outcome of a measurement on entangled states [15, 16]. As a consequence of the constraints that the local hidden variable model (LHVM) imposes on statistical correlations of a bipartite systems, John Bell formulated the Bell inequality in 1964 [17]. A violation of the Bell inequality therefore contradicts at least one of the assumptions made in the LHVM. Finally in 1981, Aspect et al. showed the first experimental results convincingly contradicting the Bell inequality, disproving the LHVM [16, 18].

The most simple manifestations of entanglement consists of an entangled bipartite system, which can be expressed by the well-known Bell states:

$$|\Psi^{+,-}\rangle = \frac{1}{\sqrt{2}}(|0\rangle|0\rangle \pm |1\rangle|1\rangle) \quad (1.1)$$

$$|\Phi^{+,-}\rangle = \frac{1}{\sqrt{2}}(|0\rangle|1\rangle \pm |1\rangle|0\rangle) \quad (1.2)$$

A fundamental characteristic of an entangled state is that it cannot be separated into a product of its constituents [16], but rather a measurement on one particle projects both particles simultaneously into one of the two parts of the coherent superposition in Eq. 1.1(1.2) with equal probability, providing a perfect correlation (anti-correlation) between the measurement outcome. Ekert et al. were the first to recognize that by distributing a string of entangled pairs, a shared quantum key could be obtained by Alice and Bob [16, 19]. An

attempt to eavesdrop requires intersecting the quantum key distribution by measuring one state, which would inevitably destroy the superposition and therefore the (anti-)correlation of the measurement outcome. Alice and Bob can verify the security of the communication channel by checking for a Bell inequality violation on selected parts of the distributed states [16].

Over the years, quantum communication protocols have evolved with an increasing level of sophistication. However already the first protocols recognized photons as suitable vectors to transfer quantum states at the speed-of-light via existing fiber networks [16, 19, 20].

In practice, fiber networks suffer from photon losses, restricting the communication fidelity and the possible communication rates. Even at the close-to-ideal 1.55  $\mu\text{m}$  wavelength, losses and decoherence grow exponentially at a rate of 0.2 dB/km. Assuming a source that emits at a rate of 10 GHz, the communication speed already decreases to around 1 Hz at a distance of 500 km [10].

In classical networks, repeaters positioned in between Alice and Bob are used to read out the attenuated signal, amplify it and send it off to the receiver. Due to the no-cloning theorem, quantum states prohibit the use of a classical amplifier since it would destroy the superposition. In analogy, the quantum repeater was proposed by Briegel et al. in 1998 to overcome this challenge [21, 22].

In essence, the overall distance  $L$  is segmented into  $n$  subsections each containing a quantum node spaced by  $L/n$ . In order to eventually distribute entanglement between the two final nodes, entanglement is first created simultaneously between  $n$  adjacent nodes, i.e. A and B, C and D (and so forth). In a next step the entanglement is swapped between B and C using linear optical elements and joint photon detection, establishing entanglement between node A and D. This practice can be extended to eventually entangle node A with node Z after  $\log(n)/\log(2)$  entanglement swapping operations, as schematically depicted in Fig. 1.1. In principle this allows for an overall communication speed that only decreases polynomially with distance [1, 10].

The inevitable photon losses in the process of entanglement generation between adjacent nodes render the process stochastic. When entanglement between A and B has been successfully established, nodes C and D might not be entangled yet. Continuing with the subsequent entanglement swapping therefore can only yield positive results if all adjacent nodes are successfully entangled. As a consequence, entanglement operation needs to be realized in a heralded fashion, i.e. one has to know when entanglement between nodes has been established. For the presented communication protocols, this role falls on the detection of a single photon on one detector. Naturally several rounds of entanglement swapping on one level of nodes are required due to imperfections in the process. In the meantime, the

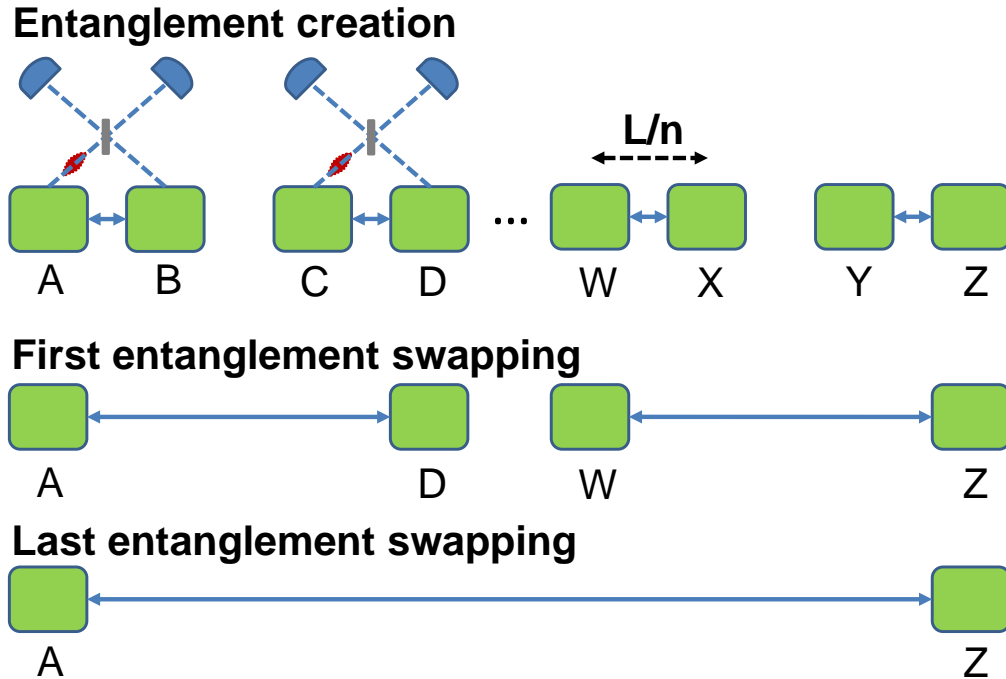


Figure 1.1: Schematic distribution of entanglement through entanglement swapping. In a first step, entanglement is created between adjacent nodes A-B, C-D,...,Y-Z. Subsequently, the entanglement is first swapped between the closest nodes of adjacent entangled node pairs (e.g. B-C) through joint photon detection to extend the entanglement (e.g. to node A-D). This practice is continued through multiple entanglement swapping operations until the final nodes are successfully entangled. Illustration derived from [10].

already established entanglement needs to be stored for sufficiently long times in one of the long-lived quantum memories, one positioned at each node [10].

A highly influential communication protocol was proposed in 2001 by Duan, Lukin, Cirac and Zoller which became widely known in abbreviated form as the DLCZ protocol [1].

Each elementary link consists of an atomic memory containing ensembles of  $N_a$  identical atoms, for instance alkali-metal atoms, which can be pictured as a  $\Lambda$ -system, depicted in Fig. 1.2. The system comprises two ground states,  $|g\rangle$  and  $|s\rangle$ , separated by a few GHz with a common upper state  $|e\rangle$  [1]. With all atoms initialized in ground state  $|g\rangle$ , an off-resonant write pulse creates a single Raman photon on the  $|s\rangle$ - $|e\rangle$  transition, usually referred to as a Stokes photon. The detection of such a Stokes photon creates a delocalized excitation

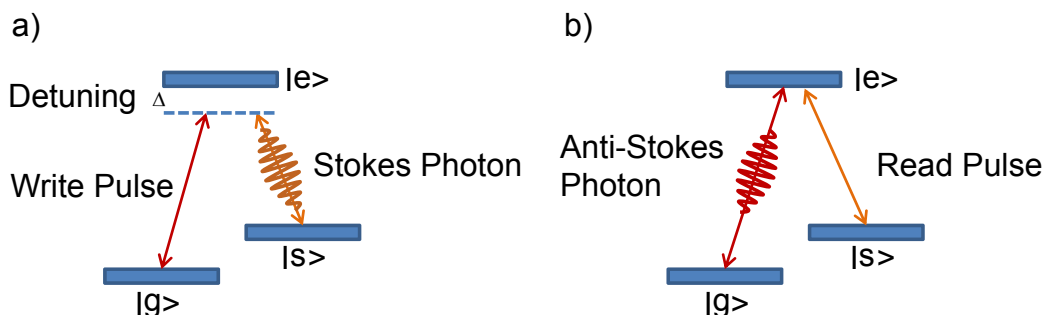


Figure 1.2: a) Schematic generation of a Stokes photon and subsequent delocalized excitation in ground state  $s$ . b) A read pulse recreates the storage process by emitting an Anti-Stokes photon. Derived from [10, 23].

arising from a superposition of  $N_a$  atoms in  $|g\rangle$  and a single atom in state  $|s\rangle$ . Provided the exact atom from which the photon originated is unknown, such a superposition can be envisioned as a spin-wave inside an atomic ensemble that can exhibit long coherence and thus long storage times [10, 13, 23].

In the DLCZ protocol, two adjacent memories (A, B) are simultaneously excited by an off-resonant laser pulse, as depicted in Fig. 1.3. The probability  $p_{exc}/2$  to excite a single Raman photon and corresponding spin-wave at each node is controlled by the laser intensity and the detuning from the excited state, creating the corresponding state:

$$\left(1 + \sqrt{\frac{p_{exc}}{2}}(a^\dagger a'^\dagger + b^\dagger b'^\dagger) + \mathcal{O}(p)\right) |0\rangle \quad (1.3)$$

with  $a^\dagger(b^\dagger)$  denoting the spin-wave creation operator and  $a'^\dagger(b'^\dagger)$  representing the photon creation operator at node A(B). Acquired phase differences are neglected for simplicity [24].

Subsequently, the modes  $a'^\dagger(b'^\dagger)$  are coupled into optical fibers and combined on a beam splitter with photon detectors at each output.

A detected photon event represents the creation of a single excitation and consequential projection of the two memories into an entangled state with one delocalized ground-state spin-wave excitation shared between node A and B:

$$|\Psi_{ab}\rangle = \frac{1}{\sqrt{2}}(|1\rangle_A |0\rangle_B + |0\rangle_A |1\rangle_B). \quad (1.4)$$

When this state is successfully created between two adjacent node pairs, for instance A-B and C-D, the neighboring quantum memories, B-C, can be read out by optically addressing

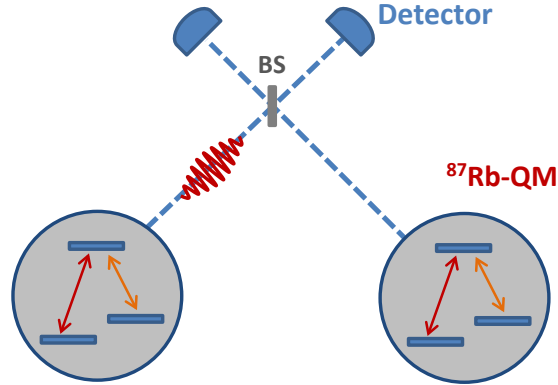


Figure 1.3: Schematic entanglement creation between two adjacent quantum memories via joint single photon detection as part of the DLCZ communication protocol. The detection of one single photon erases the “which path” information and heralds the entanglement creation. BS: beam splitter

the  $|s\rangle - |e\rangle$  transition (see Fig. 1.2b), reversing the storage process by emitting an Anti-Stokes photon associated with the modes  $b'$  and  $c'$  (see Fig. 1.4). The detection of a single photon after combining the two modes on a beam splitter projects the nodes A and D into an entangled state of one shared delocalized excitation [24]. A fundamental limitation of the DLCZ protocol is the finite probability  $p_{\text{exc}}^2/4$  to emit more than 1 photon at a time. Two photon emission introduces the possibility of ending up with both quantum memories containing a single atomic excitation, i.e. a  $|1\rangle_A |1\rangle_B$ -state. This configuration is detrimental to the overall fidelity as well as communication speed, since it limits the operation of each node to a low emission probability  $p_{\text{exc}} \ll 1$  [23, 24]. Consequently most operations do not produce any excitation and the system remains in a vacuum state, whose contribution approximately doubles through every entanglement swapping operation [10].

In order to overcome this inherent flaw, Sangouard et al. proposed to use a dedicated single photon source in conjunction with an atomic memory positioned at each node, as schematically outlined in Fig. 1.4 [24]. A single photon source, a quantum dot (QD) for instance, emits a triggered single photon of high temporal and spectral purity [6, 25]. This photon propagates through a beam splitter with specific transmission ( $\alpha$ ) and reflection coefficients ( $\beta$ ) (with  $|\alpha|^2 + |\beta|^2 = 1$ ), that are identical at each node. If reflected, the photon is stored in the quantum memory, formally described by the creation operator  $a^\dagger$  ( $b^\dagger$ ), otherwise it is coupled into an optical fiber ( $a'^\dagger$  ( $b'^\dagger$ )), which combines the two modes on a 50:50 beam splitter that is located in between, creating the two new modes  $\tilde{a}$  and  $\tilde{b}$ . Similar to the DLCZ protocol each beam splitter output is equipped with a single photon detector.

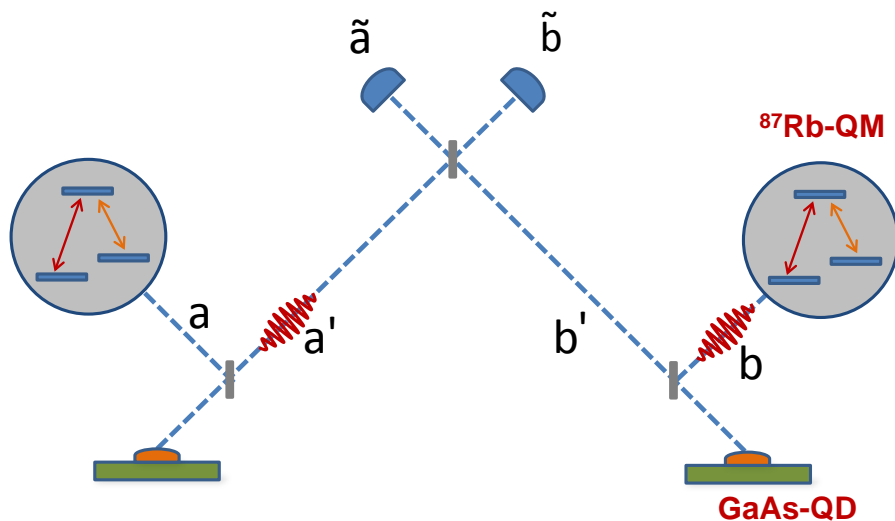


Figure 1.4: A hybrid communication protocol: each node contains a quantum memory and a dedicated single photon source. Entanglement between nodes is created in analogy to the DLCZ protocol by joint detection of single photons. Illustration derived from [24]

The corresponding state of the two photons at the inputs of the second beam splitter is given by [24]

$$[\alpha^2 a^\dagger b^\dagger + \alpha\beta(a'^\dagger b^\dagger + a^\dagger b'^\dagger) + \beta^2 a'^\dagger b'^\dagger] |0\rangle, \quad (1.5)$$

which contains three parts corresponding to different possible scenarios:  $\alpha^2 a^\dagger b^\dagger |0\rangle$  creates an excitation at each quantum memory, which goes undetected since no photon can trigger either of the detectors. The second term,  $\alpha\beta(a'^\dagger b^\dagger + a^\dagger b'^\dagger) |0\rangle$ , will induce an event at one of the photon detectors, creating the desired entangled state  $|\Psi\rangle = \frac{1}{\sqrt{2}} (a^\dagger + b^\dagger) |0\rangle$ . The third part of the equation,  $\beta^2 a'^\dagger b'^\dagger |0\rangle$ , creates no excitation in either of the memories, since both emitted photons are detected by the detectors. In this case, the detection will leave the system in a vacuum state [24].

A single detector event in  $\tilde{a}$  ( $\tilde{b}$ ) does not allow to distinguish the second and third part, since in two-photon-coalescence, both photons exit the beam splitter through the same output and are registered as a single event by the detector. A registered photon event creates the following state

$$\beta^2 |0\rangle \langle 0| + \alpha^2 |\Psi\rangle \langle \Psi|, \quad (1.6)$$

with  $|\Psi\rangle$  expressing a delocalized excitation shared by quantum memory A and B.

Due to the absence of fundamental errors induced by the occurrence of  $|1\rangle_A |1\rangle_B$ -states, the probability of entanglement creation at each link can be significantly higher in comparison



to the DLCZ protocol [10]. Entanglement swapping operations are used to eventually create entanglement at distant locations A and Z in analogy to the DLCZ protocol.

To quantify the advantage of this protocol, one has to consider the overall time to successfully create entanglement between distant nodes A and Z, given by:

$$T_{Total} = \left(\frac{3}{2}\right)^{n+1} \frac{L_0}{c} \frac{1}{P_0 P_1 \dots P_n P_{n+1}} \quad (1.7)$$

The total length  $L$  is divided into subsections of lengths  $L_0 = L/2^n$ . The probability of successful entanglement creation in an elementary link is given by  $P_0 = 2p_1\beta^2\eta_t\eta_d$  for the single-photon source protocol, in which  $p_1$  denotes the probability of single photon emission per trigger pulse.  $P_i$  represents the success probability of entanglement swapping at the  $i^{th}$  level. Photon losses and detector efficiencies are factored in as  $\eta_t$  and  $\eta_d$  respectively. This probability can be considerably higher compared to  $p_{DLCZ} = p_{exc}\eta_t\eta_d$  since  $p \ll 1$  needs to be fulfilled.

Assuming close-to-ideal single photon sources ( $p_1 = 0.95$ ) and photon detectors ( $\eta_d = 0.90$ ) Sangouard et al. concludes a potential communication speed-up of a factor of 18 at a communication distance of 1000 km, which even increases to a factor of 42 at 2500 km [24]. Despite the optimistic assumptions made on the single photon source fidelity, an advantage over the DLCZ protocol is expected as soon as  $p_1$  exceeds 0.67, a value already achieved by state-of-the-art single photon sources [6, 8, 26, 27].

## 1.2 Single photon sources

Photon sources that deterministically emit single photons or entangled photon pairs constitute major building blocks for emerging quantum technological applications, enabling the speed of light distribution of quantum states in the framework of quantum networks [10, 26, 28]. Such quantum networks facilitate the realization of large-scale quantum computers which in turn present the prospect of an exponential speed-up in computational applications [29, 30, 31]. Furthermore, non-classical photonic states provide a route of enhanced sensing schemes through the realization of multi-photon states [32, 33].

One building block of the previously introduced hybrid quantum communication protocol is a designated single photon source, motivating a closer look at single photon sources in general, and quantum dots in particular.

The requirements imposed on single photon sources are broadly similar independent of the quantum application. A single photon source should, as the name suggests, emit no more than one single photon at a time. After the emission, the quantum system is no longer excited and is inhibited from emitting another photon [2]. Single photon emission is characterized by a vanishing probability of multi-photon emission, expressed by the so called single photon purity, which can be inferred from a second-order correlation measurement. By splitting up the signal beam into two separate beams, in the framework of a Hanbury Brown-Twiss interferometer, and detecting arrival times of photon events of each beam on identical single photon detectors, one accumulates a histogram of relative time delays between consecutive photon events. Such a measurement reveals the second order correlation function defined as:

$$g^2(t) = \frac{\langle a^\dagger(t)a^\dagger(t+\tau)a(t)a(t+\tau) \rangle}{\langle a^\dagger(t)a(t) \rangle^2} \quad (1.8)$$

with  $a^\dagger(t)$  and  $a(t)$  denoting the creation and annihilation operator of a photon at time  $t$  [34, 35].

A perfect single-photon purity manifests in the absence of histogram events at relative time delay  $t = 0$ , i.e.  $g^2(0) = 0$ , meaning a vanishing probability of emitting more than one single photon at a time. This antibunching behavior verifies the quantum nature of the generated light and thereby differs greatly from classical light sources such as a laser or thermal light, which show Poissonian ( $g^2(0) = 1$ ) and super-Poissonian ( $g^2(0) = 2$ ) statistics, respectively [36, 37].

Since photons interact very weakly with each other in vacuum, logical operations involving two photons are carried out by projective measurements via photon interference [2]. The performance is critically affected by the degree of coalescence of the participating,

frequency-matched photons, which predominately depends on the coherence and the spatio-temporal overlap. Two single photons identical in frequency, polarization and temporal envelope are considered indistinguishable. If these two photons simultaneously enter a beam splitter through different input ports, both will always exit the beam splitter in the same output.

Experimentally, photon indistinguishability is measured in a Hong-Ou-Mandel measurement. A stream of single photons originating from the same single photon source, spaced in time by constant intervals, are split up into two paths. One path length is chosen to be longer by an integer number of time intervals, in order to coalesce two photons, emitted at different points in time, on a beam splitter. Single photon detectors at each beam splitter output register arrival times. An absence of coinciding events of the two detectors stems from perfectly indistinguishable photons that always exit the beam splitter through the same output and are therefore registered by the same detector. Indistinguishable photons are directly related to a Fourier-transform limited emission from a single photon source, since in this case no variation in emission frequency, polarization or temporal envelope can occur [26, 38].

For most quantum photonic applications, the operational speed is critically affected by the overall photon flux. Consequently, as the third requirement, an ideal single photon source exhibits a strong light-matter interaction, expressed by a high oscillator strength [35]. Furthermore outcoupling of the emitted photons out of the solid-state environment into free space needs to be efficient. This can be achieved by specific manipulation of the photonic environment. Placing the emitter inside a cavity achieves a preferential emission into a highly-directional mode, further increasing the rate of usable photons, by minimizing photon losses [6, 7].

With the possibilities photonic quantum application opened up, a range of single photon sources of various strengths and weaknesses have emerged.

Pioneering experiments involving single neutral atoms revolved around enhancing single-photon emission into a defined cavity mode. Especially alkali atoms, such as Rb and Cs with  $\Lambda$ -type energy levels, have proven to be viable single photon sources of near unity efficiency.

Limitations to the single atom systems are the finite trapping time and the fluctuating atom-cavity mode coupling, resulting in decoherence and possible multi-atom effects. On the other hand, single ions circumvent such disadvantages through stable radio-frequency ion traps localizing single ions for longer time scales, ensuring continuous operation [39].

The experimental complexity involved in single atom/ion photon source operation brought solid-state systems on the map. As the solid-state environment spatially confines the emitter, drifts in localization are eliminated. Additionally, cooling of the bulk material removes

the need for optical cooling techniques, significantly reducing experimental difficulty. By means of standard confocal microscopy techniques such localized solid-state emitters can be investigated and manipulated optically [40].

In the following the focus will be on one specific type of emitter, quantum dots. However, there are many other solid-state emitters that are subject of active research. Color-centers, most famously the nitrogen vacancy (NV) center in diamond, have gained interest in recent years due to their high spin coherence and ability to manipulate optically the highly coherent spin state. By substituting two adjacent lattice sites in high-purity diamond with a nitrogen atom and a vacancy, an optically active impurity is formed [39, 40]. The two unpaired electrons give rise to a triplet spin configuration. The  $m_s = 0$ -spin configuration ( $\frac{1}{\sqrt{2}}(|\uparrow\downarrow\rangle + |\downarrow\uparrow\rangle)$ ) is energetically lower by 2.88 GHz due to spin-spin interaction than the  $m_s = \pm 1$ -configuration ( $|\downarrow\downarrow\rangle$  and  $|\uparrow\uparrow\rangle$ ). By applying a magnetic field, the degeneracy of the  $m_s = \pm 1$ -states is lifted and each  $m_s = \pm 1$  spin state can act as the upper state of an individual qubit with  $m_s = \pm 0$  representing the ground state. Harnessing the coherence of this qubit in isotopically pure diamond enabled the spin-spin entanglement of two remote NV-centers and therefore establishing a true quantum communication channel [41]. However, extraction of photons out of the high-index diamond is inefficient and photonic engineering based on nanofabrication proves to be difficult [42].

### 1.2.1 Quantum dots

A hybrid approach to quantum communication, as described in chapter 1.1, requires a single photon source that is spectrally matched to the alkali-based atomic memory, a trait that is difficult to achieve in color centers. Naturally a single alkali atom can act as a single photon source. However, the high complexity of single photon generation from a single atom introduces unnecessary challenges.

An alternative, solid-state-based “artificial atom” should allow a significant reduction of the experimental demands while exhibiting excellent photonic properties, such as a higher oscillator strength and therefore brightness.

Possibly the most versatile solid-state single photon source is a semiconductor quantum dot. By confining a cluster of  $\approx 10^4$ - $10^5$  atoms of a semiconductor material in a higher band gap matrix, a nanoscale potential trap is formed. The electron wavefunction is confined in all three dimensions manifesting in a delta-function density of states, which results in the formation of discrete energy levels [43].

Before detailing the optical and band-structure properties of quantum dots, the growth process of quantum dots and specifically epitaxial GaAs quantum dots will be discussed.

## 1.2.2 Growth of epitaxial GaAs quantum dots

Most prominently, InGaAs quantum dots have proven to be a versatile quantum system that can be manipulated and investigated optically [44, 45], and therefore have become the “work-horse” of quantum dot research.

Through layer-by-layer deposition of InAs on GaAs in molecular beam epitaxy (MBE), the lattice mismatch of about 7% leads to a build-up of strain, which eventually relaxes by the formation of InAs islands, after the deposition of just 1.5 monolayers. Subsequent capping with GaAs confines the InAs cluster forming InAs-quantum dots, which emit photons of  $\approx 1200$  nm wavelength. This self-assembled growth process is widely known as Stranski-Krastanov-growth [43]. A blue-shift in emission energy is typically achieved by an in-situ annealing processes, in which the higher temperatures promotes alloying of the InAs with the surrounding GaAs, forming ternary InGaAs quantum dots.

This alloying process is capable of blueshifting the InGaAs quantum dots to emit as low as 895 nm, spectrally matching atomic transitions of Cs [46].

The presented work aims to achieve an efficient interface between epitaxial quantum dots and the  $^{87}\text{Rb}$  D1 and D2 transitions, residing higher in energy than Cs, at 794.978 nm (1.559 eV) and 780.241 nm (1.589 eV) respectively [47]. Both Rb transitions are energetically higher than the band gap of GaAs of 1.52 eV [48], consequently rendering it unsuitable as a barrier material for a compatible quantum dot.

However, as quantum dot material, the GaAs band gap is close enough to the desired energy, that by spatial confinement the emission can be shifted into resonance with Rb. As a suitable barrier material,  $\text{Al}_x\text{Ga}_{1-x}\text{As}$  constitutes an obvious choice, since it is readily available in most MBE systems. By changing the aluminium content of the ternary material the energy gap can be tailored to the desired level of confinement.  $\text{Al}_x\text{Ga}_{1-x}\text{As}$  can be widely found in III-V semiconductor structures, where it is for instance used as a barrier material for GaAs quantum wells or as part of  $\lambda/4$ -layers of alternating refractive index in Bragg mirror structures [49].

The aforementioned applications are only possible by strain-free heterolayer growth of GaAs and  $\text{Al}_x\text{Ga}_{1-x}\text{As}$  of varying Al-concentration, which stems from a near-perfect match in lattice constant. Consequently self-assembled Stranski-Krastanov growth of GaAs quantum dots does not occur by simple epitaxial deposition of GaAs on an  $\text{Al}_x\text{Ga}_{1-x}\text{As}$  host material.

An alternative growth process, illustrated in Fig. 1.5, represents the formation of quantum dots by subsequent filling of droplet-etched nanoholes with GaAs [50, 51]. In a first step, a thick layer (120 nm) of  $\text{Al}_{0.4}\text{Ga}_{0.6}\text{As}$  is deposited on the GaAs-(001) substrate as the bottom half of the quantum dot confining barrier. A subsequently deposited thin layer of

Al is inhibited from crystallizing due to a discontinued or highly reduced arsenic flux. Al droplets form by means of atomic migration on the hot surface ( $T \approx 600$  K). The interaction with the underlying material promotes diffusion of arsenic atoms from the  $\text{Al}_{0.4}\text{Ga}_{0.6}\text{As}$  into the droplet, liquefying the substrate below [52]. As-atoms diffuse out of the droplet and escape the surface altogether or can migrate to the boundary of the droplet, where the droplet partially crystallizes to form a small outer ring, while unbound material can desorb from the surface. This process etches nanoscopic holes with walls surrounding the opening [52, 53, 54]. A low arsenic atmosphere during the process promotes the etching of nanoscopic holes with typical depths of 5-10 nm, which are subsequently filled with GaAs and capped with a thick layer of  $\text{Al}_{0.4}\text{Ga}_{0.6}\text{As}$ . During the filling process the GaAs assumes the shape of the nanohole, due to only limited intermixing of AlGaAs and GaAs at the interface. High quality GaAs quantum dots are formed with a typical quantum dot density of  $0.3 \mu\text{m}^{-2}$  [53].

A clear distinction from InGaAs quantum dots constitutes the intrinsically strain-free nature of epitaxial GaAs quantum dots. Consequently, an inhibition of strain-related effects is expected [57]. Furthermore, owing to the different growth technique and mode of quantum dot assembly, no wetting layer is formed in the process. Typically observed interaction of the quantum dot with the wetting layer is assumed to disappear [58, 59]. Notably, another growth technique of epitaxial quantum dots emerged which does not require the etching of nanoscopic holes. By deposition of Ga onto the AlGaAs in an As-deprived environment Ga droplets are formed which subsequently crystallize upon reinstating of the arsenic flux [60]. The grown GaAs quantum dots are also strain-free. However, a low process temperature ( $T \approx 300$  K) make the formation more prone to incorporation of crystal defects and impurities [56].

### 1.2.3 Level structure of epitaxial GaAs quantum dots

In a semiconductor, the periodically repeating wavefunctions of each individual atoms in a lattice overlap to form a Bloch state. Due to Pauli's exclusion principle, atomic states experience a Pauli repulsion resulting in a closely spaced state-manifold, generally viewed as continuous energy bands. The lowest unoccupied band, the "conduction band", and the highest occupied band, the "valence band", are separated by a material specific energy gap (1.52 eV in GaAs) [48].

The dispersion relation, which is described by  $\mathbf{k}\cdot\mathbf{p}$  theory, can be approximated by a parabola in  $k$ -space around the  $\Gamma$ -point (depicted in Fig. 1.6b) given by  $E = \frac{\hbar^2 k^2}{2m^*}$ , where  $m^*$  denotes the effective mass, characterizing the mobility of a charge in the lattice [43, 61]. The three

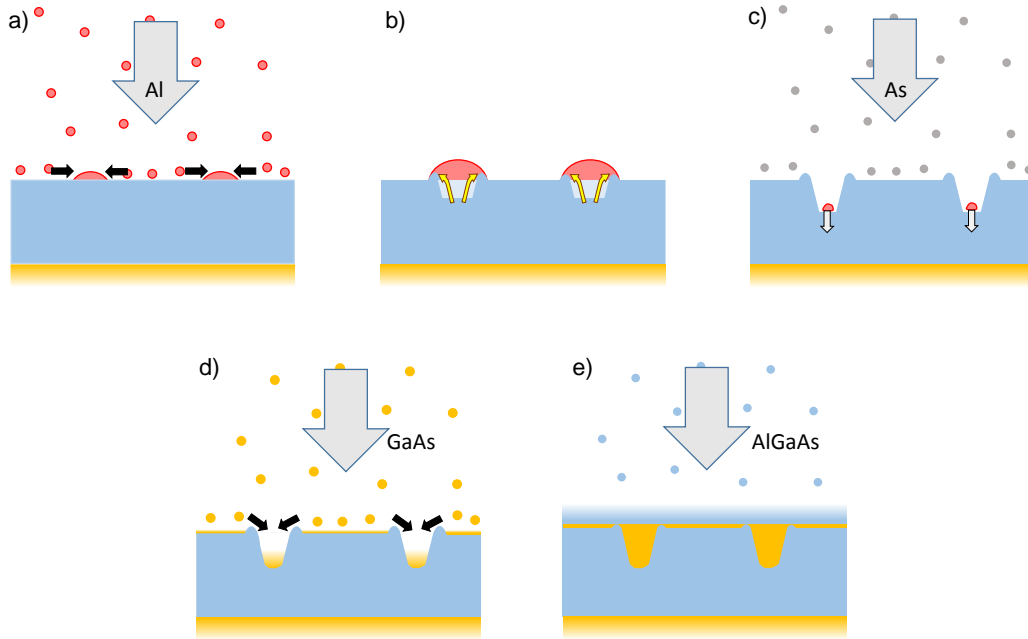


Figure 1.5: Growth process of epitaxial GaAs quantum dots by local droplet etching and subsequent filling of nanoholes with GaAs. a) Deposition of Al in absence of (or greatly reduced) arsenic atmosphere leads to the formation of small Al droplets on the surface. b) As atoms dissolve into the Al, beginning the etching process of nanoscopic holes. c) A small amount of arsenic atmosphere promotes the etching processes of typically 5-10 nm deep holes. d) Subsequently the nanoholes are filled with GaAs and e) overgrown with AlGaAs, capping the epitaxial GaAs quantum dot [52, 54, 55, 56]

dimensional confinement of the Bloch wave function in a quantum dot imposes boundary conditions on the  $k$ -vector resulting in equidistant discrete energy levels. In the lowest (highest) conduction-band (valence-band) state the boundary conditions result in a Gaussian envelope function of the Bloch state [55, 62].

By means of controlling the exact size of the quantum dot as well as the barrier material composition, the level of confinement can be adjusted to tune the quantum dot transition frequencies.

The excited state exhibits a total spin of  $J_e = 1/2$  and can therefore be occupied by two electrons of opposing spin projection of  $J_z = \pm 1/2$ . Lifting an electron into an excited state depletes the lattice of a negative charge, creating a positive virtual particle, a hole. The hole state arises from p-type atomic orbitals with  $J_h = 3/2$ . An illustration of the s-type (p-type) electron (hole) Bloch functions is given in Fig. 1.6a. Note that the envelope function is dictated by the boundary conditions of the confining potential, while the individual atomic

## 1.2. Single photon sources

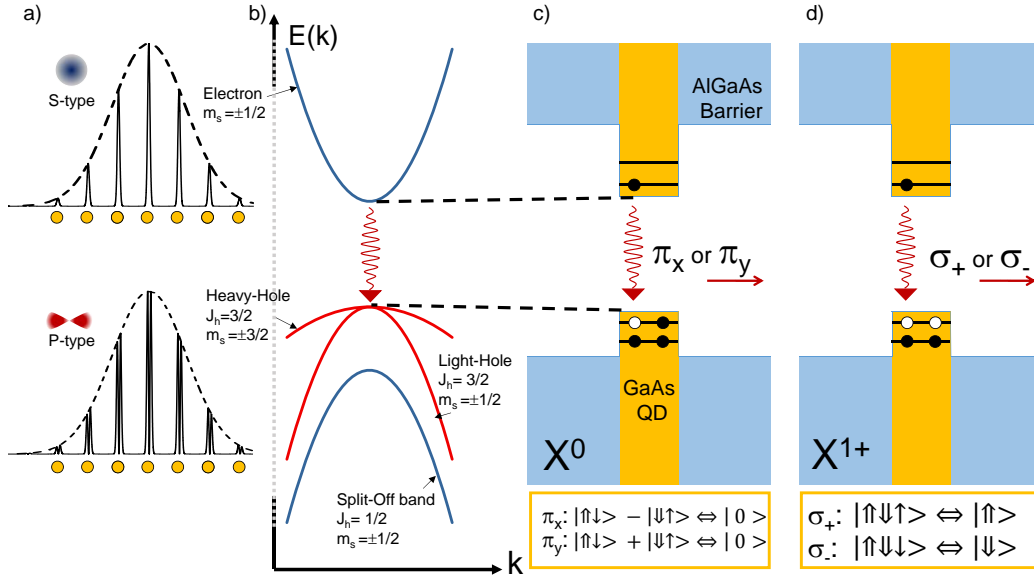


Figure 1.6: Electronic properties of epitaxial GaAs quantum dots. a) s-type electron and p-type hole Bloch wave function, with Gaussian envelope function. b) Parabolic dispersion relation of conduction band and valence band at the  $\Gamma$ -point in bulk GaAs. c) Abiding the boundary conditions of the confining potential allows for only discrete k-vectors, leading to the formation of discrete energy levels. Recombination of an exciton yields linearly polarized single photon emission from either a singlet or a triplet spin configuration. The two possible decay paths exhibit perpendicular polarization. d) Positively charged exciton form two degenerate trion states, that recombine by emitting circular-polarized single photons.

orbitals remain unchanged.

The interaction with the lattice results in a comparably higher effective mass for the  $J_z = \pm 3/2$  hole state with respect to the  $J_z = \pm 1/2$  hole state, coining the term heavy-holes and light-hole respectively. While light-hole and heavy-hole energies are degenerate at the  $\Gamma$ -point in bulk material, this degeneracy is lifted in a confined structure and the heavy hole states reside several tens of meV higher in energy. The spin-orbit split-off band lies several hundreds of meV lower in energy due to spin-orbit interaction and can be disregarded [35, 43, 63]. By absorbing a photon of sufficient energy an electron-hole pair, a so called exciton ( $X^0$ ), is created. The two charges are bound by an attractive Coulomb interaction, lowering their total energy by the excitonic binding energy. In an unstrained GaAs quantum dot, the transition dipole moment lies perpendicular to the growth direction (z-axis) in the (x-y)-plane, coupling efficiently to optical fields propagating along z.

After a time scale of  $T_1 < 1$  ns the exciton recombines radiatively, emitting a single photon



of a frequency corresponding to the exciton energy (see Fig. 1.6c)

Emission of a photon requires adherence to conservation of angular momentum. Consequently only excitons with angular momentum  $\Delta M_z = \pm 1$  can partake in the process, while the two possible transition of  $\Delta M_z = \pm 2$ ,  $|X_d\rangle = \frac{1}{\sqrt{2}}(|\uparrow\uparrow\rangle - |\downarrow\downarrow\rangle)$  and  $|Y_d\rangle = \frac{1}{\sqrt{2}}(|\uparrow\uparrow\rangle + |\downarrow\downarrow\rangle)$ , are forbidden and therefore considered dark excitons [63].

The unstrained nature of epitaxial GaAs quantum dots yields highly symmetric structures. However the non-equivalency of the  $[110]$ - and  $[1\bar{1}0]$ -axis in zinc-blende structures lowers the symmetry to  $C_{2v}$  even for cylindrical quantum dots. As a consequence the bright exciton eigenstates hybridize to a singlet state ( $|X_b\rangle = |\uparrow\downarrow\rangle - |\downarrow\uparrow\rangle$ ) and a triplet state ( $|Y_b\rangle = |\uparrow\downarrow\rangle + |\downarrow\uparrow\rangle$ ), splitting the bright transition by the electron-hole exchange interaction into a doublet which is separated in energy by the fine structure splitting (FSS). The polarization of the emitted photons becomes linear with orthogonal polarizations for  $|X_b\rangle$  and  $|Y_b\rangle$  [35, 62, 63]. In contrast to InGaAs-QD the symmetric shape of GaAs QDs lowers the FSS by almost an order of magnitude to approximately 1 GHz, which can even be eliminated by tailored multi-directional strain fields [64].

When two excitons are present in such a QD, the two cascaded decay channels of this biexciton (XX) state first emit a red-shifted linear polarized photon and a subsequent photon of orthogonal polarization originating from the  $X^0$  state. The cascaded biexciton decay channels are indistinguishable by color due to the degeneracy of the  $X^0$  state but orthogonal in polarization. Therefore a FSS-free GaAs QD constitutes an on-demand source of entangled photon pairs [28, 65].

Fig. 1.7 shows the typical spatial distribution of GaAs quantum dots obtained from a position-resolved photoluminescence measurement of a  $24 \times 24 \mu\text{m}^2$  section of sample piece O820 (sample provided by Y. Huo, O.G. Schmidt and A. Rastelli of the IFW Dresden).

Residual doping or optically gated structures enable injection of additional charge carriers into the QD [5, 66]. In the simplest configuration, an additional single electron or hole is present, forming a trion with the exciton; denoted as  $X^{1-}$  and  $X^{1+}$ , respectively. The attractive Coulomb interaction between the electron and hole outweighs the repulsive electron-electron interaction, effectively lowering the trion state energy over the neutral exciton typically by several meV. Notably, this effect is strongly dependent on the exact quantum dot shape [62]. In contrast to neutral excitons, the trion state are degenerate in zero magnetic field and decay by emitting a circularly polarized photon, as depicted for the  $X^{1+}$  in Fig. 1.6d.

While each quantum dot shows similar emission patterns, the exciton energies vary from quantum dot to quantum dot within the ensemble due to size differences, which stem from the self-assembled nature of the growth mechanism. Provided sufficiently low quantum dot

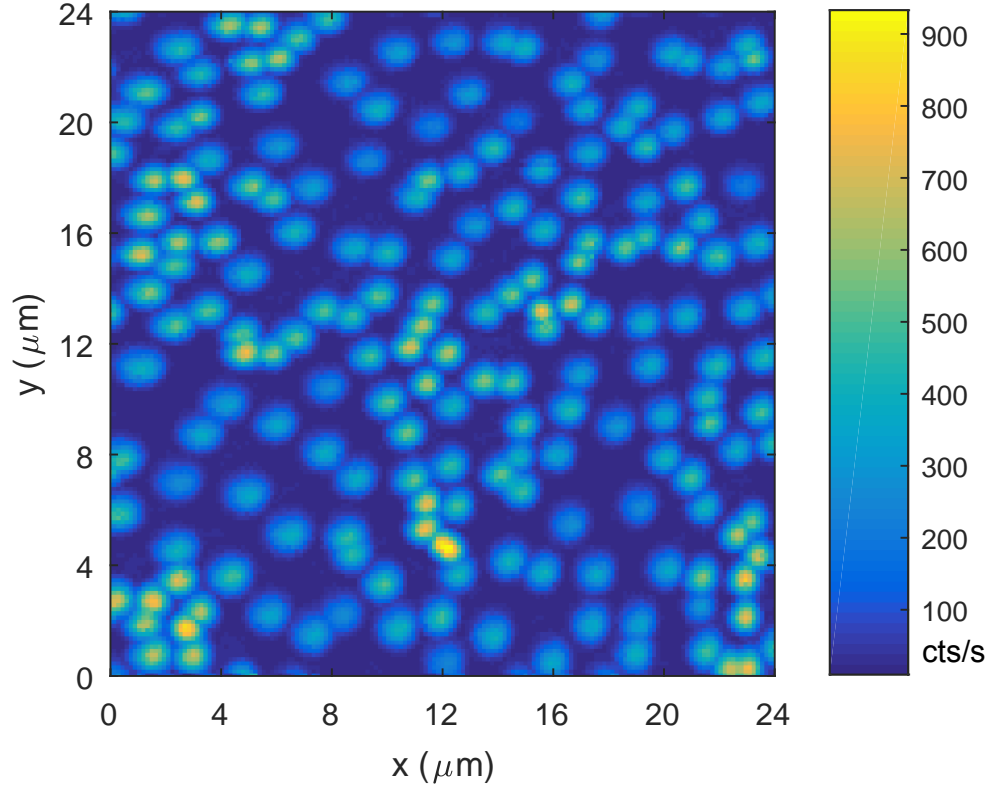


Figure 1.7: Spatially-resolved photoluminescence measurement of epitaxial GaAs quantum dots (sample O820) shows the random spatial distribution of emitters. A quantum dot density of  $0.34 \mu\text{m}^{-2}$  is measured. (Figure provided by M.Löbl)

densities, a single quantum dot can be isolated spatially in the confocal detection spot. In order specifically to investigate one individual exciton transition of a specific dot, spectral filtering or resonant excitation is required.

#### 1.2.4 Single photon emission from a quantum dot

Generally, each quantum state of an electron (hole) in the conduction band (valence band) is composed of the product of the envelope wave function  $|F_{c/v}\rangle$ , the electronic Bloch function at the  $\Gamma$ -point  $|u_{c/v}\rangle$  and the spin state  $|a_{c/v}\rangle$ . The key property characterizing the dipole transition is the transition matrix element between the excited state and the ground state,

which can be expressed as

$$\mathbf{P} = \langle F_v | F_c \rangle \langle u_v | \mathbf{p} | u_c \rangle \langle a_v | a_c \rangle \quad (1.9)$$

with  $\mathbf{p}$  denoting the momentum operator. Therefore, a non-zero transition matrix element requires a finite envelope function overlap, Bloch functions to have opposite parity and the charge carrier spin conservation in the process [35]. The transition matrix element  $\mathbf{P}$  not only imposes the selection rules, but the magnitude describes the strength of the transition. This strength is commonly quantified by the dimensionless oscillator strength

$$f = \frac{2}{\hbar\omega_0 m_0} |\mathbf{P}|^2 = \frac{E_P}{\hbar\omega_0} |\langle F_v | F_c \rangle|^2, \quad (1.10)$$

in which  $\hbar\omega_0$  denotes the transition energy,  $m_0$  denotes the rest mass of the electron and  $E_P$  is the Kane energy, a material specific parameter (28.8  $\mu\text{eV}$  for GaAs). Assuming a perfect envelope function overlap ( $|\langle F_v | F_c \rangle|^2=1$ ), the maximum oscillator strength for a GaAs QD is 18.1, an order of magnitude higher than atoms or NV centers [67].

A high oscillator strength directly equates to a short exciton lifetime, due to the inverse proportionality:

$$\Gamma_{\text{rad}} = 1/T_1 = \frac{nq^2\omega^2}{6\pi m_0 \epsilon_0 c^3} \cdot f, \quad (1.11)$$

with the refractive index of GaAs  $n$ , electron charge  $q$ , permittivity  $\epsilon_0$  respectively, and speed of light  $c$  [67].

Depending on the growth conditions, the lateral extent of GaAs quantum dots can be multiple times higher than the extent in the growth direction, giving the QD a lens- or disc-like shape [68]. Considering an exciton Bohr radius of  $a_0 = 10.3$  nm in GaAs, the implicitly assumed strong-confinement of the wavefunction in 1.10 can break down for lateral dimensions  $\gg 10$  nm. In this case, the underlying potential trap only weakly confines the exciton, constituting a hydrogen-like state. The weak-confinement (WC) regime leads to an oscillator strength that is proportional to the exciton area, defined as [35, 67]:

$$f_{\text{WC}}^{\text{max}} = 2 \frac{E_P}{\hbar\omega_0} \left( \frac{L}{a_0} \right)^2. \quad (1.12)$$

This ‘‘giant oscillator strength’’ can be envisioned as the sum of all oscillator strengths of all lattice sites the oscillator occupies, giving rise to an exceptionally bright single photon source.

## 1.2. Single photon sources

---

Notably, pronounced non-radiative decay channels described by the non-radiative transition rate  $\Gamma_{\text{nrad}}$  can mask the actual radiative decay rate ( $\Gamma_{\text{rad}}$ ), due to an accelerated total decay of the excited state. The overall ratio of radiative decay rate over the total decay rate defines the total quantum efficiency of the emitter

$$QE = \frac{\Gamma_{\text{rad}}}{\Gamma_{\text{rad}} + \Gamma_{\text{nrad}}}. \quad (1.13)$$

Generally, the high oscillator strength of quantum dots constitutes a great asset. However, they are embedded in a material of high-refractive index ( $n = 3.6$  for GaAs) diminishing the overall collection efficiency due to total internal reflection at the interface to vacuum, which impedes outcoupling out of the solid-state matrix.

The optical properties of the surrounding material can be harnessed, however, by carefully tailoring the photonic environment that the QD is embedded in. Incorporating distributed Bragg reflectors to form a cavity around the QD in the growth process, modifies the photonic density of states and defines an optical mode that the emitter couples to preferentially. Furthermore, the lateral extent can be confined by etch-defined micropillar structures acting as a waveguide. In conjunction with a close to unity quantum efficiency an on-demand single photon source of efficiencies greater than 65% have been reported, while still maintaining high indistinguishability on the single-photon level [6, 26].

### 1.2.5 A quantum dot exciton as a two level system

A quantum dot exciton strikes strong resemblance to a quantum mechanical two-level system, exhibiting trademark properties well-known from atom experiments. In this picture the exciton state constitutes the excited state, which by means of spontaneous emission decays in sub-ns time scales to the two-level ground state, i.e. the empty quantum dot. Coherently driving the two level-system with a resonant laser gives rise to a variety of phenomena, such as Rabi oscillations, coherent light-scattering, the Mollow-triplet and induced transparency, that can be described in a quantum mechanical formalism [43].

The off-diagonal elements  $\rho_{12} = \rho_{21}^*$  of the  $2 \times 2$  density matrix represent coherence properties of the system, while the diagonal elements  $\rho_{22}$  and  $\rho_{11}$  on the other hand denote the population of the excited state and ground state respectively.

Due to the strong resemblance to Zeeman-split nuclear spin states, two level systems can be

described mathematically in analog, by the optical Bloch equations. In the rotating-wave approximation the dynamics of each matrix element is described by a differential equation [34]:

$$\dot{\rho}_{22} = -\dot{\rho}_{11} = -\frac{1}{2}i\Omega \cdot (e^{i(\omega_0-\omega)t}\rho_{12} - e^{-i(\omega_0-\omega)t}\rho_{21}) \quad (1.14)$$

$$\dot{\rho}_{12} = -\dot{\rho}_{21}^* = \frac{1}{2}i\Omega \cdot e^{-i(\omega_0-\omega)t}(\rho_{11} - \rho_{22}) \quad (1.15)$$

In this formalism  $\omega_0$  and  $\omega$  denote the two-level frequency and the drive frequency respectively. The Rabi frequency  $\Omega$  is a direct measure for the drive strength of the two-level system. The name stems from the equivalence to the actual frequency at which Rabi oscillations occur, provided spontaneous emission and dephasing processes are sufficiently slow [34].

Generally, the Rabi frequency constitutes an important parameter, since it drastically changes the response of the two-level system and thereby its emission spectrum, ranging from predominantly coherently scattered laser light to the formation of emission side-bands at high drive strengths [14, 69].

Experimentally the Rabi frequency is directly controlled via the resonant laser intensity  $I$ , arising from the following relation:

$$\Omega = \sqrt{\frac{2q^2}{\epsilon_0 c \hbar^2} (\mathbf{e} \cdot \mathbf{D})^2 \cdot I} \quad (1.16)$$

in which  $\mathbf{D}$  denotes the dipole moment in the dipole approximation and  $\mathbf{e}$  the polarization vector of the incident light [34]. The dynamics of the system can be visualized neatly in the Bloch sphere, as depicted in Fig. 1.8. The two poles represent population in the excited or ground state. Any point on the surface of the sphere describes any possible pure state in terms of the state population as the projection onto the vertical axis, as well as the coherence terms that span the x-y-plane.

Real-world systems are subjected to the interaction with the environment. For quantum dots the incorporation into a solid-state matrix exposes the emitter to interaction with the lattice in form of elastic and inelastic scattering processes. Elastic scattering, through phonons for instance, disrupts the phase of the wavefunction and therefore decoheres the system from a pure state, projecting the system onto the vertical axis of the Bloch sphere with a characteristic time scale  $T_2^*$ , as illustrated in Fig. 1.8a. This process however retains the total population and therefore system energy, coining the term “pure dephasing” [55]. On the

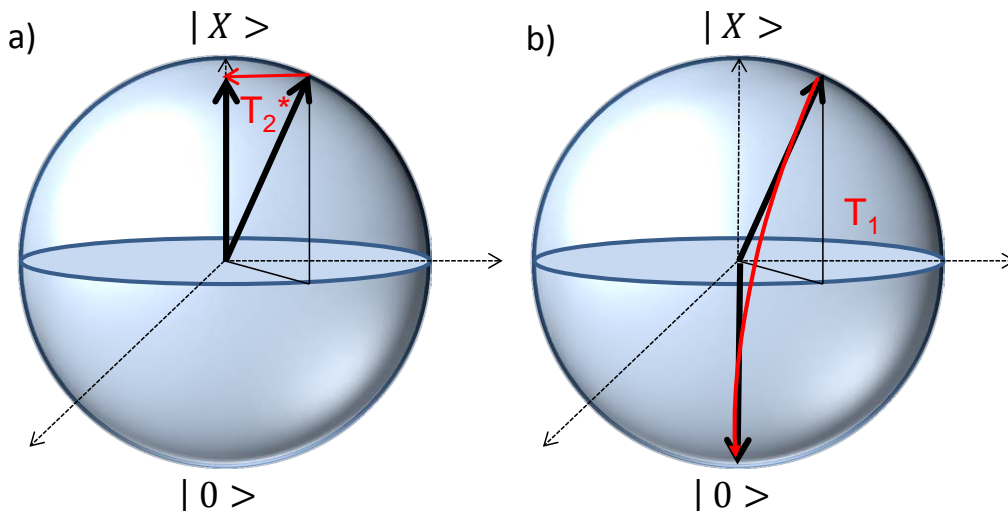


Figure 1.8: The Bloch sphere. The poles represent the excited state and the ground state. a) Illustration of energy-conserving decoherence with characteristic time scale  $T_2^*$ . b) Illustration of the population decay mechanism with characteristic time scale  $T_1$ .

other hand a decay on the vertical axis is equivalent to population decay and therefore loss of energy. For a quantum dot, energy is predominately dissipated by spontaneous emission of photons with the oscillator-strength related time-scale  $T_1$ . Furthermore, inelastic scattering processes in the lattice can lead to a non-radiative decay, acting as another possible population decay mechanism, which results in a reduced quantum efficiency.

Scattering processes are pronounced in bulk GaAs or quantum well structures even at cryogenic temperatures. The discrete energy levels of quantum dots however greatly reduce phonon-mediated exciton decay processes [70].

The overall usability of quantum dot photons relies on the indistinguishability of each emitted photon. In order to maximize two-photon coalescence on a beam splitter, the temporal envelope, frequency and phase relation need to be identical. A spontaneously emitted single photon is described by an exponentially decaying envelope function of a radiative decay time  $T_1$ , with a carrier frequency given by the energy of the two level system. Dephasing within this envelope can be envisioned as discontinuities in the oscillation, decreasing the overall total coherence time  $T_2$  of the single photon wave packet which is expressed as [55]

$$\frac{1}{T_2} = \frac{1}{2T_1} + \frac{1}{T_2^*}. \quad (1.17)$$

For a perfect emitter the dephasing ( $1/T_2^*$ ) process becomes negligible and the photon bandwidth is only limited by the Fourier-transform of the radiative decay time  $T_1$ . A Fourier-limited single photon source in conjunction with perfect collection efficiency constitutes the ideal case for quantum communication applications as it delivers indistinguishable photons on demand [44, 55].

In reality, the quantum dot is subjected to a fluctuating charge environment in its vicinity. The residual doping, most likely p-type doping in MBE-grown GaAs heterostructures, as well as excess charges induced by off-resonant laser excitation, introduce an exciton energy jitter through the DC Stark effect. This “spectral wandering” occurs on timescale longer than the spontaneous recombination time  $T_1$ . Consequently two photons originating from the same emitter at separate points in time differ in color, diminishing two-photon coalescence. Particularly photons generated by two distinct quantum dots experience uncorrelated charge noise, rendering two-photon interference difficult due to these random energy fluctuations [71, 72].

State-of-the-art InGaAs QDs are embedded in electrically gated tunnel junction structures, that allow for deterministic charging of the quantum dot by application of a static voltage. This capacitor-like structure furthermore depletes excess charges, calming the overall charge environment [73]. Additionally, the diode structure gives rise to deterministic fine tuning of the exciton energy via the quantum confined Stark effect, allowing for an active locking of the exciton transition to a reference laser. Limited by the electronic bandwidth of the structure, an active feedback loop has shown to reduce low-frequency charge noise [74].

Another detrimental source of noise to the quantum dot energy arises from a coupling to the noisy nuclear-spin-bath, well known in InGaAs QDs. The interdiffusion of gallium into the InAs quantum dot establishes localized strain fields, generating electrical field gradients that couple via quadrupolar interaction with the nuclear spin bath [75]. The resulting fluctuations in magnetic field of the nuclei, known as the Overhauser field, in turn, couple to the electron state by contact hyperfine interaction, which constitutes a dephasing mechanism [73]. Due to their s-type wavefunction, only electrons couple notably to the nuclear spins, while holes are largely decoupled owing to their p-type Bloch wavefunction, since a wavefunction overlap with the nuclei is required [51, 76].

The theoretical lineshape for a Fourier-limited emission derives from the Fourier-transform of the single photon depicted in Fig. 1.9a, constituting a Lorentzian lineshape with FWHM =  $1/T_1$ . Under consideration of dephasing, the lineshape remains Lorentzian with a broadened bandwidth given by FWHM =  $2/T_2$ . The frequency spectrum of the charge envi-

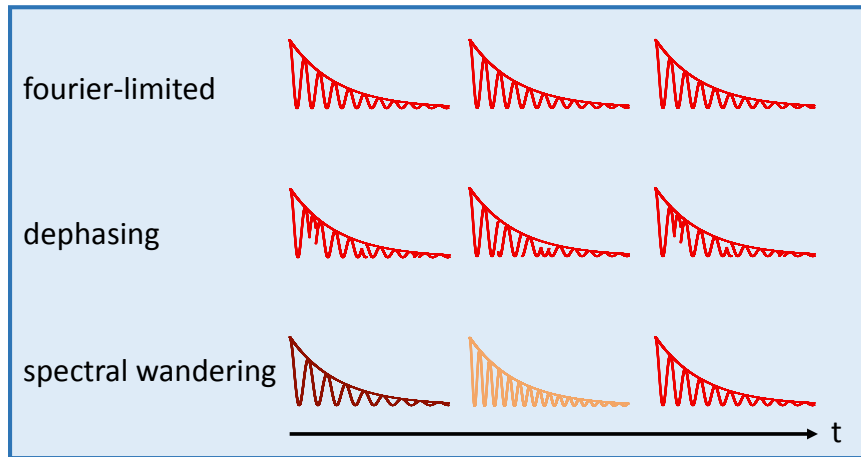


Figure 1.9: Illustration of single photon emission patterns. a) Fourier-limited emission yields identical photons. b) Dephasing introduces disruptions to the phase-coherence. c) Spectral wandering results in fluctuating single photon energies. (Adapted illustration derived from [55]).

ronment and nuclear spin interaction are quite diverse leading to an additional increase in linewidth.



## Chapter 2

# Interfacing GaAs quantum dots and atomic quantum memories

An efficient interface between GaAs quantum dots and atomic memories appears elusive with regard to the bandwidth mismatch of the two systems. Fourier-limited emission of a quantum dot exceeds the natural linewidth of the bare Rubidium D1 and D2 transition by 2 orders of magnitude (6 MHz compared to  $\sim 1$  GHz), owing to the high oscillator strength of quantum dots [47, 77]. Before further investigating the quantum dot properties, a short overview on the development of a suitable high-bandwidth quantum memory will be given, in order to outline the boundary conditions imposed on the quantum dot single photons. The presented quantum memory was developed by the group of Prof. Philipp Treutlein in the framework of a collaboration within the University of Basel, which also motivated the presented work on epitaxial GaAs quantum dots.

## 2.1 Simple atomic quantum memory suitable for semiconductor quantum dot single photons

This section aims to give a brief introduction to Rb quantum memories based on electromagnetically induced transparency and summarizes the main results originally published in:

“Simple Atomic Quantum Memory Suitable for Semiconductor Quantum Dot Single Photons”

Phys. Rev. Lett. **119** - 060502, Published 8. August 2017

Janik Wolters<sup>1</sup>, Gianni Buser<sup>1</sup>, Andrew Horsley<sup>1</sup>, Lucas Béguin<sup>1</sup>, Andreas Jöckel<sup>1</sup>, Jan-Philipp Jahn<sup>1</sup>, Richard J. Warburton<sup>1</sup>, Philipp Treutlein<sup>1</sup>

1 - Department of Physics, University of Basel, Klingelbergstrasse 82, CH-4056 Basel, Switzerland

Photon storage in a  $\Lambda$ -system (schematically illustrated in Fig. 2.1a) occurs through a transfer of a photon into a long-lived spin-wave [78]. Subsequent to initializing the atomic ensemble in one of the ground states,  $|g\rangle$  for example, the arriving single photon addresses the  $|g\rangle$ - $|e\rangle$  transition, while simultaneously a strong classical laser pulse addresses the  $|s\rangle$ - $|e\rangle$  transition, facilitating the storage of the single photon in form of a delocalized coherence of the two ground states [13].

In such a scheme, an important prerequisite constitute a negligible cross-coupling between the two transitions  $|g\rangle$ - $|e\rangle$  and  $|s\rangle$ - $|e\rangle$ , realized by sufficiently large energy differences and/or selection rules [13]. Both transitions of the <sup>87</sup>Rb fine-structure doublet,  $5^2S_{1/2} \rightarrow 5^2P_{1/2}$  (D1) and  $5^2S_{1/2} \rightarrow 5^2P_{3/2}$  (D2), meet this criterion. Their common ground state  $5^2S_{1/2}$  is split into two hyperfine levels (F=1, F=2) separated by 6.8 GHz, which can act as the two ground states of a  $\Lambda$  system. Completing the  $\Lambda$  system is one of the 2 (4) hyperfine transitions of the D1 (D2) line [47]. For quantum memory applications the D1 line has proven to yield higher theoretical efficiencies, mitigating unwanted coupling to hyperfine transitions outside the  $\Lambda$  system [79].

In a first step the control laser pulse drives  $|s\rangle \rightarrow |e\rangle$  ( $F_2 \rightarrow F'_1$ ), as depicted in Fig. 2.1a, ultimately initializing the system in ground-state  $|g\rangle$  ( $F_1$ ). Simultaneous with the arrival of the single photon resonant to  $|g\rangle \rightarrow |e\rangle$ , a strong control laser pulse addresses the  $|s\rangle \rightarrow |e\rangle$  transition. This strong control pulse facilitates a destructive interference of the two possible absorption paths  $|g\rangle \rightarrow |e\rangle$  and  $|s\rangle \rightarrow |e\rangle$ , rendering  $|g\rangle$  and  $|s\rangle$  to be in a “dark

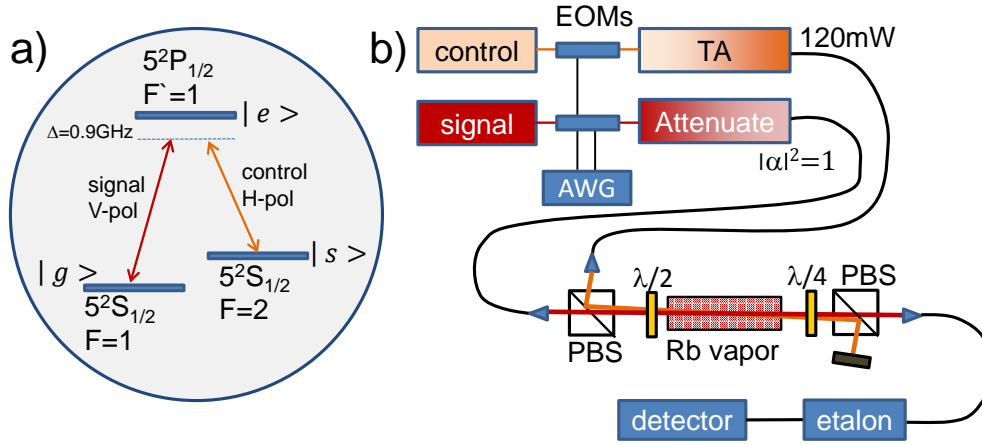


Figure 2.1: a)  $\Lambda$ -system arising from the  $^{87}\text{Rb}$  D1 transition. b) Experimental setup. Electro-optic modulators (EOMs) controlled by an arbitrary waveform generator (AWG) optically gate the control and signal laser pulses. The control laser pulses are subsequently amplified by a tapered amplifier (TA), while the signal pulses are attenuated to contain on average  $\alpha = 1$  photon per pulse. Polarization control is achieved by a set of polarizing beam splitters (PBS),  $\lambda/2$  and  $\lambda/4$ -wave plates. Detector: The stored signal is counted on a single photon avalanche photodiode (APD), analyzed in a Hanbury Brown-Twiss or an unbalanced Mach-Zehnder interferometer.

superposition". The otherwise opaque vapor becomes transparent within a small frequency window, through so called electromagnetic induced transparency (EIT). By increasing the control laser intensity, the bandwidth of the transparency window and therefore the memory bandwidth can be increased [13].

A sharp transition is always accompanied by a steep variation of the refractive index with frequency. Therefore the envelope function of the propagating photons is slowed down by orders of magnitude due to the enhanced refractive index. Slowing down the single photon wavepacket dispenses energy, which induces spin-flip processes that co-propagate to the pulse in form of a spin-wave. Since the origin of the ground-states  $|g\rangle$  and  $|s\rangle$  stems from opposing spin-states, this spin-flip process dynamically couples the groundstate into a coherent superposition. The interaction between spins and photons can be regarded as a composite quasi-particle of photons and spins, a dark-state polariton [80].

The intensity of the control laser directly controls the composition of the dark-state polariton. When the single photon enters the atomic medium, the polariton is initially purely photonic. With decreasing control beam intensity the group velocity of the single photon wavepacket is slowed down, while at the same time the photonic contribution is reduced.

## 2.1. Simple atomic quantum memory suitable for semiconductor quantum dot single photons

---

Ultimately the polariton becomes purely atomic, mapping out the photonic state as a single, delocalized flipped spin inside the medium [81].

The process can be written as follows:

$$|1\rangle |g\rangle \rightarrow |0\rangle \sum_{i=1}^N \frac{1}{\sqrt{N}} |g_1, \dots, s_1, \dots, g_N\rangle \quad (2.1)$$

where  $|1\rangle$  represents the single photon Fock state and  $|0\rangle$  the vacuum state. By applying another control pulse, the spin-wave is reconverted into a single photon on demand, completing the storage and retrieval process [81].

In the presented quantum memory, as depicted in Fig. 2.1b, attenuated laser pulses of 1 ns duration containing on average  $\alpha = 1$  photon are stored using the D1 transition of a warm  $^{87}\text{Rb}$ -vapor ( $T = 75^\circ\text{C}$ ,  $\text{OD} = 5$ ). These signal pulses are created by optically gating a continuous wave (CW)-laser with an electro-optical modulator (EOM, Jenoptik), controlled by a fast arbitrary waveform generator, simulating the demands, which the storage of single photons imposes. The signal pulses of  $\delta f = 660$  MHz bandwidth are combined with the control laser pulse, which is amplified in a tapered amplifier (TA) after the EOM, on a polarizing beam splitter, deliberately introducing a 10 mrad angle between the two beams through the cell. In conjunction with polarization filtering and spectral filtering through a Fabry-Pérot etalon, the slight angle allows efficient suppression of the control laser pulse by 12 orders of magnitude, necessary to distinguish the weak signal from the strong control pulse (120 mW in CW). The angle of the two beams is chosen to be small to ensure sufficient overlap ( $e^{-2}$ -diameter = 400  $\mu\text{m}$ ) throughout the 37.5 mm long isotopically clean  $^{87}\text{Rb}$ -vapor cell. The attenuation of the control laser stands in contrast to minor losses introduced to the retrieved signal pulses accounting to a factor of 3, which can be attributed to non-optimized optical components and coupling losses into a single-mode fiber.

A first laser pulse ( $t = 500$  ns) initializes the atoms in ground state  $|g\rangle$ . After a wait time of 25 ns the signal arrives, which is subsequently stored for 50 ns and then recreated (see Fig. 2.2) After exclusion of noise, the end-to-end efficiency yields  $(N_{\text{signal}} - N_{\text{noise}}) / (\alpha^2 \eta_{\text{APD}} / f_{\text{rep}} t_{\text{int}}) = 3.4(3) \%$  of stored and subsequently retrieved photons coupled into the fiber, with an overall signal-to-noise ratio of 3.7(6). Under consideration of the optical losses and extrapolating for theoretical immediate retrieval after storage (delay  $t = 0$  ns) reveals a total internal efficiency of  $\eta_{\text{int}} = 17(3) \%$ .

The remaining noise level stems from atomic fluorescence of atoms in the  $F=2$  state, verified by a second order correlation measurement of  $g_2(0) = 2$ , while the coherent signal pulse exhibits a  $g_2(0) = 1$ . In good agreement to the determined signal-to-noise ratio, a

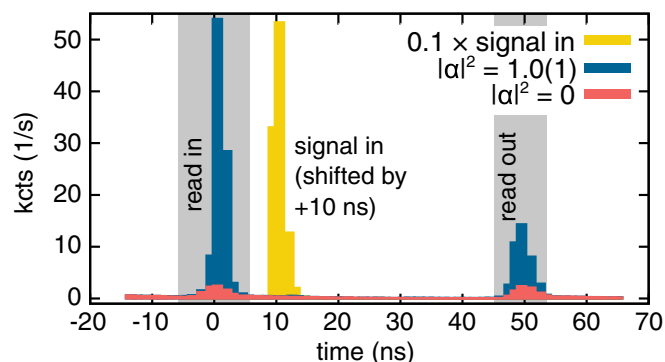


Figure 2.2: Arrival time histogram for the detected photons. Yellow: input signal, Blue: 50 ns storage-and-retrieval of signal pulses containing on average  $\alpha = 1$  photon. Red: storage-and-retrieval in the absence of a signal pulse ( $\alpha = 0$ ) allows for the determination of the level of noise contamination arising from atomic fluorescence.

$g_2$ -measurement on the retrieved signal arises from an admixture of the two components, manifesting in a  $g_2(0) = 1.3$ . The storage and retrieval process therefore preserve the photon statistics (see Fig. 2.3a).

Furthermore, in order to investigate the memory’s ability to retain the coherence of the signal pulse, stored photons are recombined on a beam splitter in an unbalanced Mach-Zehnder interferometer with retrieved photons of the subsequent duty cycle. A visibility of 65% is observed at a single photon level ( $\alpha = 1$ ), depicted in Fig. 2.3b. For a single photon level, the noise contamination accounts for a non-negligible share of the total signal, which is highly incoherent, naturally diminishing the visibility. By increasing the average photon number per pulse to  $\alpha = 10$ , the signal-to-noise ratio increases as well and the observed visibility reaches  $V > 99\%$ , indicating that the storage-and-retrieval process retains the coherence.

Consequently one of the main objectives for future improvements is motivated by a reduction of incoherent noise. This thermal noise stems from atoms that are not successfully initialized in the  $F=1$  state and remained in the “wrong”  $F = 2$  state. When these atoms diffuse into the interaction zone, while the control laser is present, the atoms fluoresce, contaminating the readout process with additional photons. A possible remedy is the use of a dedicated pump laser with a large beam diameter, which initializes the vapor homogeneously, minimizing the number of atoms in the “wrong” initial state.

To investigate the origin of limitations to the total internal efficiency, a theoretical model was developed, which shows excellent agreement with the obtained data. Simply increasing the control laser Rabi frequency by a factor 4 in conjunction with optimized control pulses already promises an increase in internal efficiency to  $\eta_{\text{int}} = 45\%$ , which can even be improved

## 2.1. Simple atomic quantum memory suitable for semiconductor quantum dot single photons

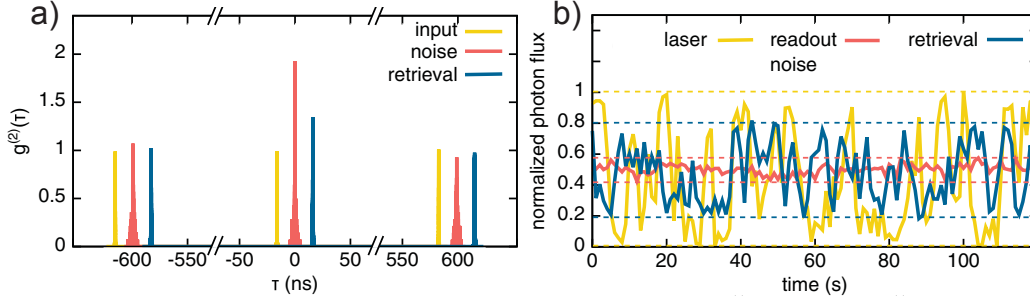


Figure 2.3: a) Second order correlation measurement on the retrieved signal pulses ( $g_2(0) = 1.3$ ), the thermal noise background and input signal exhibit  $g_2(0) = 2$  and  $g_2(0) = 1$  respectively. For better visibility the input signal (retrieval) is shifted by -16 (+16) ns. b) Interference between subsequently retrieved signal pulses in an unbalanced Mach-Zehnder interferometer, measured via random thermal phase fluctuations, reveals a visibility of 65%. To accommodate for imperfect mode overlap, the data is normalized based on the assumption of unity fringe visibility ( $V = \frac{\max - \min}{\max + \min}$ ) of the input laser signal.

to  $\eta_{\text{int}} = 92\%$  for  $\text{OD} = 35$ , if unwanted coupling to the parasitic  $F' = 2$ ,  $m_{F'} = 0$  state can be prevented. One way of ensuring negligible coupling to these transition is achieved by applying a magnetic field to the vapor cell, which lifts the degeneracy of the Zeeman substructure. In a magnetic field on the order of  $B \approx 1$  T, the atoms enter the Paschen-Back-Regime in which the atomic electron and nuclear spins decouple. The separation of the ground state hyperfine sublevels becomes larger than the optical linewidth in the warm vapor and enable to optically address each sublevel individually. Since transitions of  $\Delta m_I \neq 0$  involve the unlikely event of a nuclear spin flip, four isolated transition manifolds are created, as illustrated in Fig. 2.4. Selectively using a  $\Lambda$ -system of one manifold allows to minimize cross-coupling to parasitic transitions through selection rules and frequency discrimination.

For real-world quantum communication application, as outlined in chapter 1.1, the photon storage times ultimately need to be sufficiently long to function as an efficient node in a quantum network. Currently the storage is mainly limited by atoms diffusing out of the interaction zone and decoherence-inducing scattering processes with the vapor cell wall. The latter can be alleviated by anti-relaxation coated cells. Improving the interaction time on the other hand is achieved by larger beam diameters.

Increasing the interaction volume, i.e. the laser beam diameter, in conjunction with magnetic shielding to mitigate ground state decoherence, allows up to ms storage times.

Implementing all these straight-forward improvements, promises a highly efficient, broad-

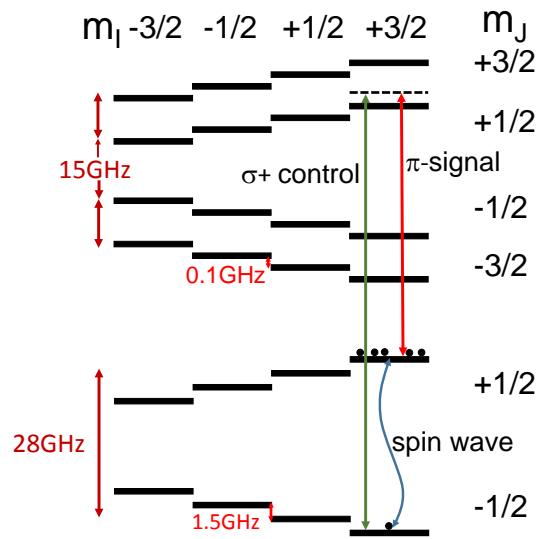


Figure 2.4: Energy levels of the Rb D2 line at  $B = 0.8$  T in the Paschen-Back regime. Electron and nuclear spin are decoupled and  $m_J$  and  $m_I$  become “good” quantum numbers. The ground states of the  $\Lambda$ -system are formed in the isolated the  $m_I = 3/2$ -manifold by the  $5^2S_{1/2}$   $m_J = -1/2$ - and  $m_J = +1/2$ -states. The  $5^2P_{3/2}$   $m_J = +1/2$  constitutes the common upper state

band quantum memory suitable as a building block in hybrid quantum communication with only comparatively low technological demands, enabling scalable quantum networks.

## 2.2 Prospect of quantum dot single photon storage in the atomic quantum memory

The presented quantum memory imposes three main constraints on the single photon emission by the GaAs quantum dot:

1. The quantum dot photons need to be spectrally matched to rubidium. Starting with quantum dots emitting close to the D1 or D2 line of rubidium, a tuning knob for the emission energy is required to bring the quantum dot into resonance with the rubidium atoms.
2. An efficient hybrid interface necessitates quantum dot photons of sufficiently low bandwidth. Based on typical exciton decay times observed on GaAs quantum dot excitons, Fourier-transform-limited emission is expected to yield single photons exhibiting a bandwidth of a few hundred MHz [58, 82]. This value is very close to the acceptance bandwidth of  $\delta f = \mathbf{660\text{ MHz}}$  demonstrated for the previously presented vapor cell memory. Consequently, the GaAs quantum dots need to be of excellent material quality to minimize interaction with defects in the surrounding lattice that could potentially impair the optical properties of the emitter.
3. In the presented quantum memory setup, storage and retrieval of a signal pulse (containing an average  $\alpha = 1$  photon) is achieved with a signal-to-noise ratio of  $\text{SNR} = 3.7$ . Consequently, a greater than unity signal-to-noise ratio demands that signal pulses arrive at the alkali vapor cell quantum memory containing  $\mu > \mathbf{0.27}$  quantum dot photons on average. This constraint can be regarded as equivalent to a combined quantum dot photon extraction and transmission efficiency of  $p_1\eta_t > \mathbf{0.27}$ .

In the following, solutions to the first two challenges are presented, before finally outlining how the third criteria can be achieved in the future.



## Chapter 3

# An artificial Rb atom in a semiconductor with lifetime-limited linewidth

Adapted from: “An Artificial Rb atom in a semiconductor with lifetime-limited linewidth”  
Phys. Rev. B **92**, 245439 - Published 28. December 2015

Jan-Philipp Jahn<sup>1</sup>, Mathieu Munsch<sup>1</sup>, Lucas Béguin<sup>1</sup>, Andreas V. Kuhlmann<sup>1</sup>, Martina Renggli<sup>1</sup>, Yongheng Huo<sup>2</sup>, Fei Ding<sup>2</sup>, Rinaldo Trotta<sup>2</sup>, Marcus Reindl<sup>2</sup>, Oliver G. Schmidt<sup>3</sup>, Armando Rastelli<sup>2</sup>, Philipp Treutlein<sup>1</sup>, Richard J. Warburton<sup>1</sup>

- 1 – Department of Physics, University of Basel, Klingelbergstrasse 82, CH-4056 Basel, Switzerland
- 2 – Institute of Semiconductor and Solid State Physics, Johannes Kepler University Linz, Altenbergerstrasse 69, A-4040 Linz, Austria
- 3 – Institute for Integrative Nanosciences, IFW Dresden, Helmholtzstrasse 20, D-01069 Dresden, Germany

### 3.1 Summary

We report results important for the creation of a best-of-both-worlds quantum hybrid system consisting of a solid-state source of single photons and an atomic ensemble as quantum memory. We generate single photons from a GaAs quantum dot (QD) frequency-matched to the Rb D2-transitions and then use the Rb transitions to analyze spectrally the quantum dot photons. We demonstrate lifetime-limited QD linewidths (1.42 GHz) with both reso-

nant and non-resonant excitation. The QD resonance fluorescence in the low power regime is dominated by Rayleigh scattering, a route to match quantum dot and Rb atom linewidths and to shape the temporal wave packet of the QD photons. Noise in the solid-state environment is relatively benign: there is a blinking of the resonance fluorescence at MHz rates but negligible dephasing of the QD excitonic transition. We therefore demonstrate significant progress towards the realization of an ideal solid-state source of single photons at a key wavelength for quantum technologies.

## 3.2 Introduction

Establishing the hardware for a quantum network is a challenging task. A source of indistinguishable single photons is required along with a means to store the single photons at each node. Single semiconductor quantum dots are excellent sources of single photons: they are bright, robust and fast emitters [2, 43]. A single quantum dot mimics a two-level atom closely such that single photons can be generated either by spontaneous emission from the upper level [7] or by coherent scattering of a resonant laser [83, 84, 14]. Subsequently emitted photons are close to indistinguishable [4]. However, achieving the lifetime-limit has been an elusive goal [85, 86], and the wavelength coverage is limited.

Independently, atomic ensembles have developed into one of the best platforms for optical quantum memories [87, 88]. The combination of strong absorption and long ground state hyperfine coherence has allowed storage times of milliseconds and efficiencies higher than 75 % to be achieved in these systems [11, 89, 90, 91]. Moreover, schemes for broadband operation with single photons at the GHz level have been proposed [13] and also demonstrated experimentally [92]; single photons emitted by a single atom were stored in a Bose-Einstein condensate of the same species and used to produce entanglement between the two remote systems [93].

A semiconductor-cold atom quantum hybrid would combine the advantage of the semiconductor (straightforward single photon generation, large oscillator strength) with the advantage of the cold atoms (slow decoherence) whilst avoiding the disadvantage of the semiconductor (fast decoherence [43]) and the disadvantage of the cold atoms (complex single photon generation [94]). This would constitute an implementation of a quantum repeater using single photon sources and memories [24]. Unfortunately, the workhorse systems are mismatched in frequency: self-assembled InGaAs quantum dots emit typically around 950 nm; the D1 and D2 transitions of the Rb atoms lie at 795 and 780 nm. We note that a frequency match has been achieved with Cs [95]; a link has also been established with a

transition of the  $\text{Yb}^+$  ion [96]; a trapped molecule produces single photons at the Na frequency [97]; and a new quantum dot growth procedure has led to a first hybrid experiment with Rb [98]. A high quality semiconductor source of single photons frequency-matched to the Rb transitions is highly desirable.

We present here a close-to-ideal semiconductor source of single photons at the Rb D2 wavelength. The emission frequency can be tuned through all the D2-hyperfine lines. We demonstrate lifetime-limited quantum dot linewidths. This points to negligible upper level dephasing and allows us to create photons by coherent Rayleigh scattering with weak, resonant excitation. We find that all our experiments (spectral analysis, intensity autocorrelation, decay dynamics) can be described in terms of a two-level atom with a common set of parameters. The only significant source of noise is slow relative to radiative emission and results in a telegraph-like blinking behavior. Apart from this the system behaves in an ideal way despite the complexity of the solid-state environment.

### **3.3 Sample**

Our solid-state source of single photons, Fig. 3.1, consists of a GaAs/AlGaAs quantum dot (QD) obtained by filling Al-droplet-etched nanoholes with GaAs [53]. The holes are formed by depositing 0.5 mono-layer (ML) of aluminium at a growth rate of 0.5 ML/s and at a temperature of 600 °C on a  $\text{Al}_{0.4}\text{Ga}_{0.6}\text{As}$  surface. This is followed by a 5 minute annealing step in arsenic ambiance. The holes are then filled with GaAs grown at 0.1 ML/s and capped again with  $\text{Al}_{0.4}\text{Ga}_{0.6}\text{As}$  resulting in strain-free GaAs QDs. The photoluminescence (PL) from the ensemble is adjusted to  $\sim 780$  nm, the wavelength of the Rb D2-line, by controlling the exact amount of deposited GaAs. Fig. 3.1b shows a typical PL spectrum from a single QD recorded at 4.2 K with non-resonant excitation at 633 nm. We observe several lines in the PL spectrum. We identify in particular the neutral exciton (X) and a red-detuned charged exciton (CX). The other lines are related to other exciton states, as yet unidentified. To fine tune the QD frequency with respect to the Rb transition lines, the sample is glued onto a piezo-electric transducer which induces uniaxial strain in the sample [99, 100], Fig. 3.1a. By scanning the piezo-voltage, reversible tuning over 30 GHz is achieved with very little creep from the piezo-electric elements, see Fig. 3.2c. In fact, the emission frequencies of the PL lines are stable over the course of a day such that a stabilization scheme was not necessary in these experiments.

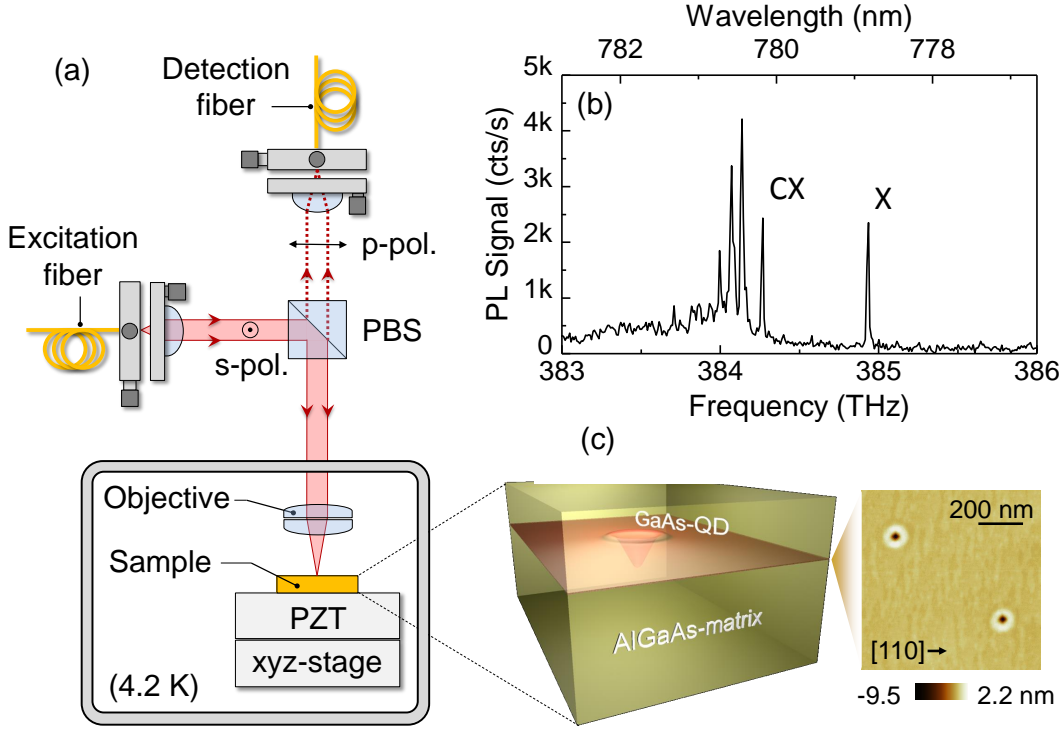


Figure 3.1: The experimental setup. a) Schematics of the resonance fluorescence setup showing orthogonally polarized excitation and detection. PBS refers to a polarizing beam splitter (PBS). The sample is glued to a piezo-electric transducer (PZT) and mounted onto an xyz-positioning stage. A solid immersion lens (SIL) on the surface of the sample increases the collection efficiency. b) PL spectrum of a single QD under non-resonant excitation at 633 nm ( $I_{NR} \sim 7 \mu\text{W}/\mu\text{m}^2$ ). We identify the neutral exciton (X) and a charged exciton (CX) which display narrow linewidths, limited here by the 9 GHz spectrometer resolution. c) Sketch of the QD layer and an AFM picture of the nano-holes obtained with in-situ etching [101].

### 3.4 Resonance fluorescence on a single QD

We first report resonance fluorescence on a single GaAs QD, the artificial Rb atom. For this, we use the dark-field microscope sketched in Fig. 3.1a. A resonant laser beam is focused onto the sample with linear polarization; resonance fluorescence from the QD is detected in the orthogonal polarization [73]. Careful control of the polarization suppresses the back-scattered laser light by 80 dB. We find that very weak non-resonant laser light ( $\lambda = 633$  nm,  $I_{NR} \gtrsim 0.8 \text{ nW}/\mu\text{m}^2$ ) is a necessary condition to observe resonance fluorescence on CX. This non-resonant excitation quenches the excitation of the neutral X and therefore acts as an “optical gate” [102]. This result was reproducibly observed on all five QDs that

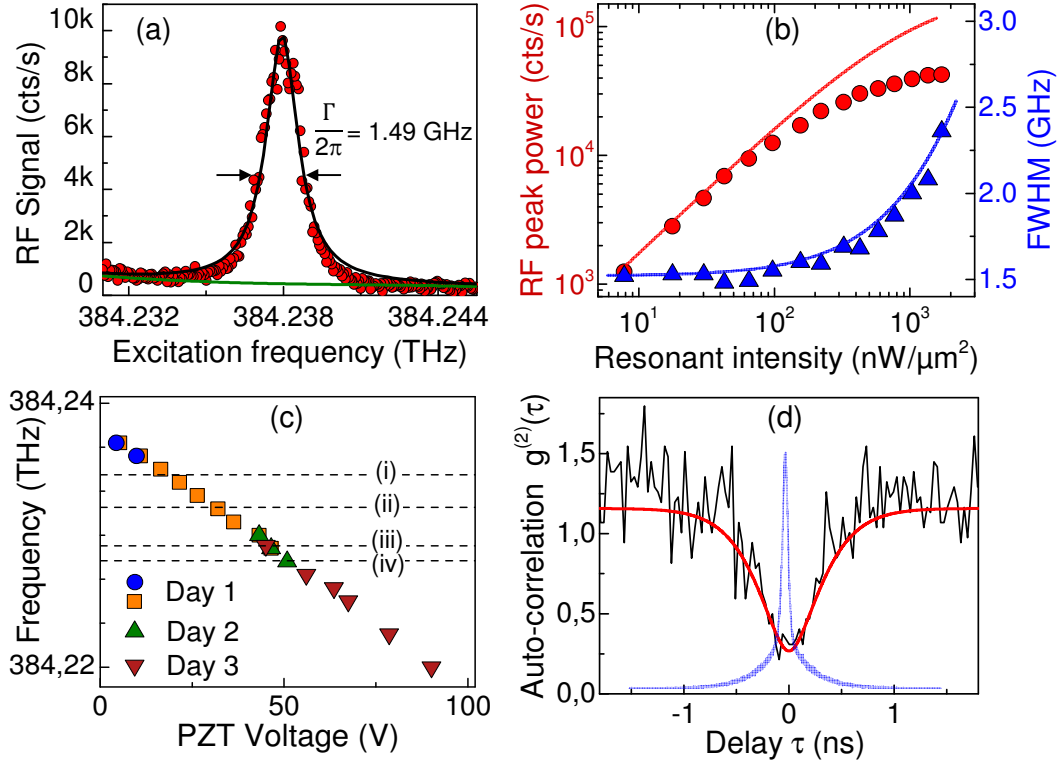


Figure 3.2: Resonance fluorescence of the charged exciton, QD1. a) Resonance fluorescence spectrum in the low power regime ( $I_R = 16 \text{ nW}/\mu\text{m}^2$ ). The laser background ( $\leq 780 \text{ cts/s}$  over the 12 GHz scanning range) is indicated in green. b) Resonance fluorescence intensity and FWHM as a function of resonant laser power. c) Frequency tuning of CX showing a linear response to the applied voltage with very little creep over the course of several days. The D2 transitions of Rb are indicated as dashed lines: (i)  $^{87}\text{Rb } F_g = 1 \rightarrow F'_e$ , (ii)  $^{85}\text{Rb } F_g = 2 \rightarrow F'_e$ , (iii)  $^{85}\text{Rb } F_g = 3 \rightarrow F'_e$  and (iv)  $^{87}\text{Rb } F_g = 2 \rightarrow F'_e$  (indices "g" and "e" denote "ground state" and "excited state" respectively). d) Second order correlation of the resonance fluorescence signal. In blue, the detectors' response function (arbitrary units for the y-axis) measured with ultra-short laser pulses (5 ps) at the QD frequency. The red line results from a fit using Eq. 3.1 convoluted with the detectors' response function. All data are obtained in the presence of an additional weak, constant non-resonant laser excitation of  $I_{\text{NR}} \approx 0.8 \text{ nW}/\mu\text{m}^2$ . The background associated with the non-resonant excitation is smaller than the detectors' dark counts.

we tested.

To record resonance fluorescence spectra, we monitor the count rate on a CCD camera as we sweep the laser frequency across the QD transition, as illustrated in Fig. 3.2a for the CX transition of QD1. The spectrum is fitted with a Lorentzian profile, and displays a signal-

to-background ratio S:B > 23 at the resonance. In the low power regime, the linewidth is  $\Gamma/2\pi = 1.49 \pm 0.04$  GHz, see Fig. 3.2a. We confirm the anti-bunched nature of the emitted photons by performing second-order correlation measurements on the resonance fluorescence signal, Fig. 3.2d. There is a small bunching on the normalized data ( $g_2(\tau) = 1.25$  for  $\tau > 1$  ns) which results from a slow blinking process, discussed below. For  $\tau \ll 1 \mu\text{s}$ , the exact blinking dynamics can be ignored and the data are fitted to the product of a constant pre-factor, which accounts for the QD dead-time (i.e. the blinking), and the second-order correlation function of a resonantly driven two-level system [103]

$$g_{\text{TLS}}^{(2)}(\tau) = 1 - e^{-\frac{1}{4}(3\Gamma_{\text{sp}} + 2\gamma^*)\tau} \times \left( \cos \lambda\tau + \frac{3\Gamma_{\text{sp}} + 2\gamma^*}{4\lambda} \sin \lambda\tau \right) \quad (3.1)$$

where  $\Gamma_{\text{sp}}$  is the spontaneous radiative emission rate,  $\gamma^*$  corresponds to the pure dephasing rate and  $\lambda = \sqrt{\Omega^2 - \frac{1}{16}(\Gamma_{\text{sp}} - 2\gamma^*)^2}$ , with  $\Omega$  the Rabi frequency of the resonant drive. Taking the experimentally measured response of the detectors into account, we find a very nice agreement and thus a coincidence detection probability consistent with zero at zero delay, the signature of pure single photon emission.

### 3.5 Spectroscopy of the Rubidium atomic ensemble with QD photons

We now turn to the spectroscopy of the Rb atomic ensemble using QD photons. We insert a room temperature 75 mm long Rb vapor cell in the detection line. The cell contains both  $^{85}\text{Rb}$  and  $^{87}\text{Rb}$  in natural abundance (72.2% and 27.8%, respectively). In a first experiment, QD1 is excited with the non-resonant pump only with  $I_{\text{NR}} = 7.1 \mu\text{W}/\mu\text{m}^2$ , Fig. 3.3a. Transmission through the atomic cloud is recorded as the piezo-voltage is increased thus tuning the QD emission frequency. As the CX transition is scanned from 384.225 THz to 384.237 THz, we observe several dips in the transmission corresponding to the hyperfine structure of the two rubidium isotopes, Fig. 3.2c. In order to distinguish between the QD and the atomic contributions to the linewidth, we perform a calibration measurement on the vapor cell by measuring the transmission with the laser only (short term [100  $\mu\text{s}$ ] FWHM  $\leq 1$  MHz). The result, shown in the appendix (see Fig. 3.6), is fitted to the theoretical Rb transmission spectrum, where the only unknown is the vapor cell temperature. Excellent agreement is found

for  $T = 24.8$  °C, corresponding to a Doppler broadening of 510 MHz. To describe the transmission spectrum recorded with QD photons, we then convolve the Rb spectrum with a Lorentzian profile of width  $\Gamma_{\text{NR}}$ , the QD linewidth under non-resonant excitation. Best agreement between the resulting function and the data is obtained for  $\Gamma_{\text{NR}}/2\pi = 1.60 \pm 0.20$  GHz. The modest depth of the transmission peaks reflects the mismatch between the QD linewidth and the atomic spectral width.

A lifetime-limited linewidth implies a negligible rate of exciton dephasing in the QD. In turn, this opens the possibility of generating single photons by coherent Rayleigh scattering. The resonance fluorescence can be divided into a coherent part, the Rayleigh scattering of the incoming laser light, and an incoherent part, resulting from an absorption and re-emission cycle. Including pure dephasing, the fraction of coherently scattered photons is given by

$$\frac{I_{\text{coherent}}}{I_{\text{total}}} = \frac{\Gamma_{\text{sp}}^2}{2\Omega^2 + \Gamma_{\text{sp}}^2 + 2\gamma^*\Gamma_{\text{sp}}}. \quad (3.2)$$

(See Appendix 3.9 for a complete description of the resonant spectrum.) The ratio is maximum in the low power regime ( $\Omega \ll \Gamma_{\text{sp}}$ ), the Rayleigh regime, and approaches unity should  $\gamma^*$  become negligible compared to  $\Gamma_{\text{sp}}$ . The last point highlights the importance of achieving a small dephasing rate. Conversely, the ratio decreases at high power where the strong excitation leads to inelastic scattering (Mollow triplet). We explore the possibility of coherent Rayleigh scattering in a second experiment where we drive the QD resonantly in the low power limit ( $I_{\text{R}} = 141$  nW/ $\mu\text{m}^2$ ). The resulting Rb transmission spectrum is shown in Fig. 3.3b. For a given driving laser frequency, we tune the QD into resonance via the piezo-voltage, and we measure the resonance fluorescence signal transmitted through the Rb vapor cell. This is then repeated for different laser frequencies. The transmission data are normalized using a linear baseline defined by points recorded when the QD is detuned from the Rb transitions. In Fig. 3.3b, the four dips corresponding to the D2-transitions of  $^{85}\text{Rb}$  and  $^{87}\text{Rb}$  can now clearly be resolved, showing negligible broadening of the atomic transitions beyond that of the atomic vapor itself. This implies that the spectrum of the light scattered by the QD has been narrowed down significantly below the lifetime limit, a clear evidence of coherent scattering from the QD [84].

To fit the measured spectrum in the Rayleigh regime, we compute the convolution between the atomic spectrum and the resonant emission spectrum, with  $\Gamma_{\text{sp}}$ ,  $\gamma^*$  and  $\Omega$  as free parameters. In order to determine a value for each parameter with the highest accuracy, we perform a global fit on both the transmission spectrum (Fig. 3.3b) and the second-order correlation measurement (Fig. 3.2d). From this combined analysis we determine  $\Gamma_{\text{sp}}/2\pi = 1.42 \pm 0.12$

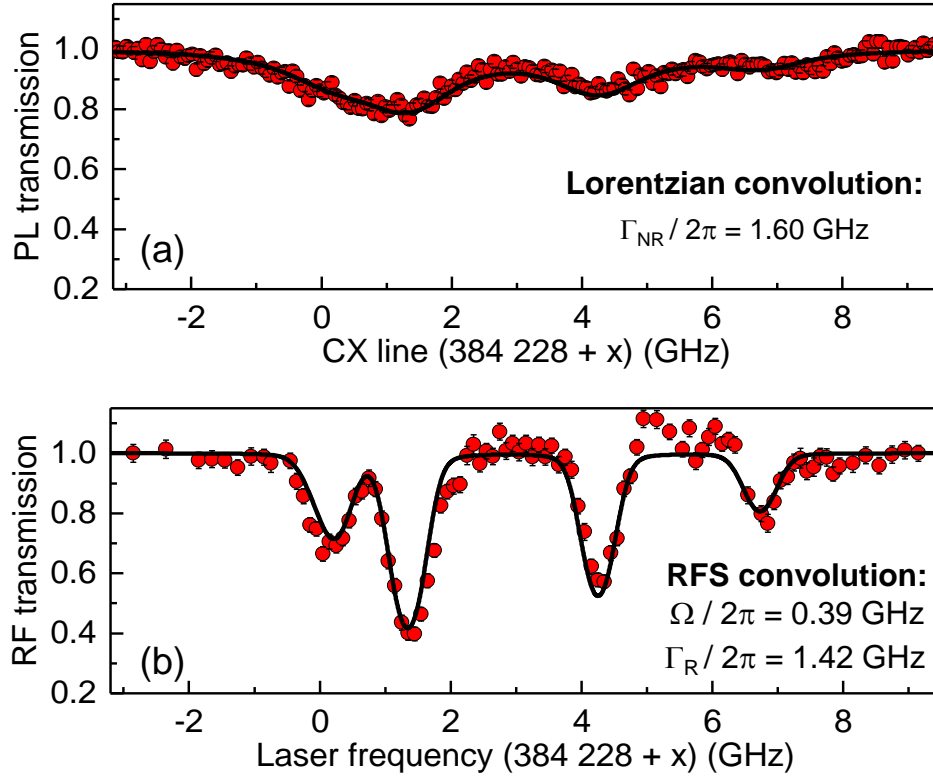


Figure 3.3: Spectroscopy of the Rb D2-transitions using QD photons. In a) QD1 is excited non-resonantly and the CX resonance is swept through the Rb transitions. The solid line is a fit based on the convolution between the atomic transmission spectrum and a Lorentzian line accounting for the spectral width of the QD photons. In b) CX is driven at resonance in the coherent Rayleigh scattering regime. The solid line is a fit where the QD is modeled as a two-level scatterer with associated resonance fluorescence spectrum (RFS).

GHz,  $\gamma^*/2\pi = 0 \pm \binom{0.10}{0}$  GHz and  $\Omega/2\pi = 0.39 \pm 0.10$  GHz, which corresponds to a fraction of coherently scattered photons as high as 87% (see details in Appendix 3.9). These results are further supported by recording a decay curve following non-resonant pulsed excitation. The data, which, incidentally, point to an unusually slow relaxation mechanism for transferring carriers from high energy continuum states into the QD, result in  $\Gamma_{sp}/2\pi = 1.7 \pm 0.2$  GHz, consistent with the spectroscopy analysis (see Fig. 3.8 from Appendix 3.10.2). We note also the excellent agreement with the power broadening experiment where the resonance fluorescence linewidth is described within the two-level system framework, with  $\Gamma_{sp}$  and  $\gamma^*$  as input parameters, Fig. 3.2b.



These results allow us to make an important conclusion, namely that we achieve lifetime-limited emission with our artificial atom. We thus combine, in a solid-state environment, a high single photon flux with negligible dephasing, a key result for further quantum optics experiments, for instance the generation of indistinguishable photons. In addition, this conclusion applies not only under resonant excitation (resonance fluorescence), but also under non-resonant excitation (photoluminescence). This is a surprising result in the context of InGaAs QDs where the transform limit has been achieved only with resonant excitation and for very specific conditions [44]; in the best case with non-resonant excitation the linewidth is about a factor of two larger than the transform limit [104] and is typically much larger still. These exceptional results on GaAs QDs reflect the high quality of the epitaxial material combined with the short radiative lifetime and possibly an unknown semiconductor advantage of strain-free QDs over highly-strained QDs.

### 3.6 Blinking in the QD signal

The solid-state environment results in negligible dephasing of the QD single photon source. However, the effects of the solid-state environment are not completely suppressed: Fig. 3.4 shows a correlation measurement under resonant excitation on a second QD for three different values of non-resonant power. The data are normalized to the average count per time bin for a Poissonian source,  $N = N_1 N_2 \tau_b T$ , with  $N_1$  and  $N_2$  the count rates on each avalanche photo-diode,  $\tau_b$  the time-resolution of the experiment and  $T$  the total integration time. In addition to the anti-bunching at zero delay already outlined in Fig. 3.2c, we observe a strong bunching peak at short delays ( $g^2(\tau)$  as high as 6.5). This corresponds to the signature of blinking in the QD emission [105]: the presence of dead times in the QD fluorescence produces packets of single photons separated in time. Assuming a simple Boolean statistics for the blinking process [106], ergodic and statistically independent of the two-level radiative decay, the second-order correlation function of the QD signal can be expressed as

$$g^{(2)}(\tau) = \left( 1 + \frac{1 - \beta}{\beta} e^{-\tau/\tau_c} \right) \times g_{\text{TLS}}^{(2)}(\tau) \quad (3.3)$$

where  $\beta$  corresponds to the fraction of time in which the QD is in an “on” state, and  $\tau_c$  to the correlation time of the blinking process. The first term (left bracket) accounts for telegraph noise associated with the blinking, the second term for the dynamics of the resonantly driven two-level system, cf. Eq. (3.1). From the fit of the data, we extract  $\beta_{CX} \sim 16\%$ , a less fa-

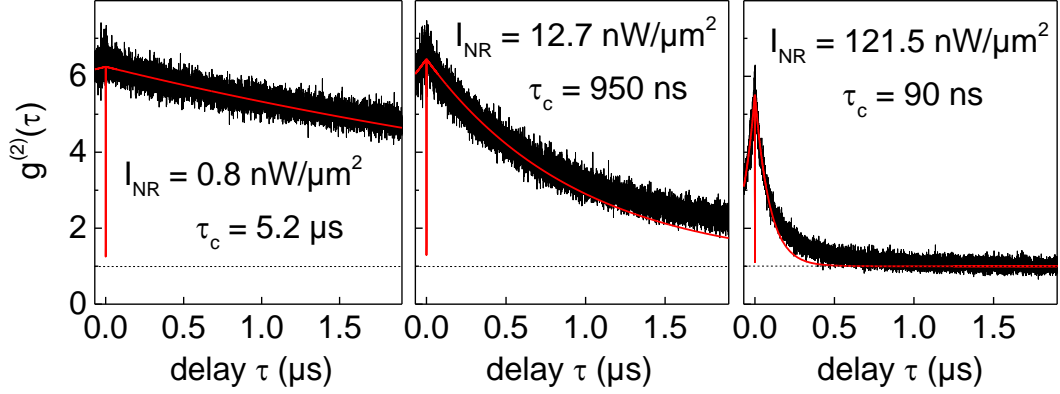


Figure 3.4: Blinking statistics on QD2. Second order correlation measurement of the resonance fluorescence signal of CX as a function of increased non-resonant pump ( $I_R = 180.5 \text{ nW}/\mu\text{m}^2$ ). Solid red lines are fits obtained from Eq. (3.3).

avorable situation for the charged exciton in QD2 as compared to QD1 ( $\beta_{CX} \sim 80\%$ , see Fig. 3.2d and Fig. 3.9 from Appendix 3.11.1). The blinking dynamics are strongly modified as we increase the non-resonant power. We find that  $\tau_c$  varies by several orders of magnitude over the available range of power with  $\beta$  remaining approximately constant. This result was reproducibly observed on all QDs we tested and reflects the general nature of the solid-state environment. It shows how the non-resonant laser power offers some control over the environment, here in all likelihood fluctuations in charge (either in the QD or in the immediate vicinity of the QD) which bring the QD in and out of resonance in a telegraph fashion with the fixed frequency laser. We note that  $\tau_c$  is in all cases considerably larger than the radiative lifetime (90 ps) such that the blinking contribution to the QD linewidth is small: the telegraph noise is consistent with the claim of a lifetime-limited QD linewidth. Also, we note that the simple on/off model does not capture all the details of the blinking dynamics. At high resonant power, the decrease in resonance fluorescence peak signal at the highest resonant powers (Fig. 3.2b) is probably related to an increase in the QD dead-time.

### 3.7 Conclusion

In conclusion, we report here a quantum hybrid system consisting of a frequency-matched solid-state source of single photons, a single quantum dot, and a Rb atomic vapor. The quantum dots exhibit lifetime-limited linewidths, even under non-resonant excitation. Resonance fluorescence in the Rayleigh scattering regime is used to address the bandwidth

mismatch between the two quantum systems. The most significant solid-state noise is at  $\sim$  MHz frequencies and results in telegraph noise in the emission reflecting QD blinking. We demonstrate some control over this correlation time, useful in the context of decoupling the QD from its complex environment. Further work should address this noise and also engineering of the photonic environment in order to achieve a higher QD single photon collection efficiency. Implementation of quantum memory protocols can then be attempted [13].

### 3.8. Appendix A: Vapor cell absorption spectrum

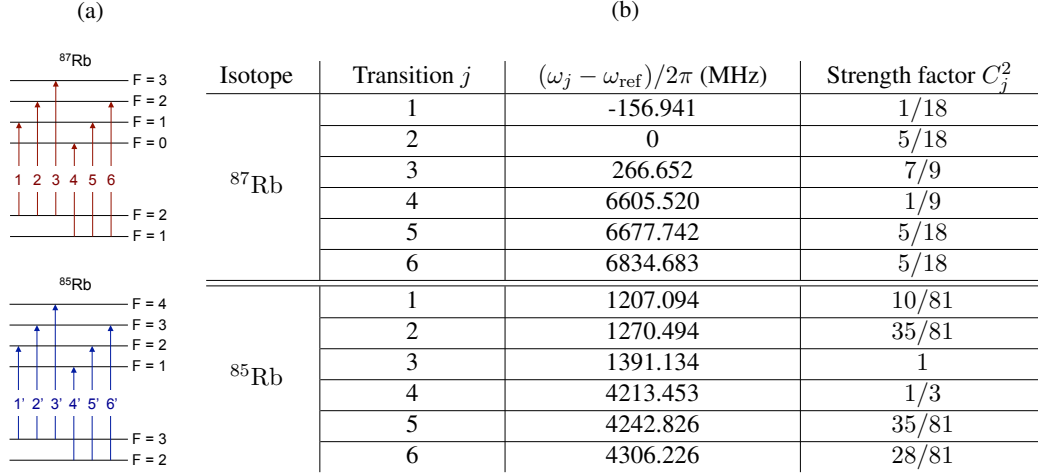


Figure 3.5: **Hyperfine structure of  $^{87}\text{Rb}$  and  $^{85}\text{Rb}$  D2 line.** (a) Sketch of the allowed hyperfine transitions. (b) Properties of the hyperfine transitions. Frequencies are given with respect to the  $^{87}\text{Rb}$  transition  $F_g = 2 \rightarrow F_e = 2$  of angular frequency  $\omega_{\text{ref}} = 2\pi \times 384\,227\,848.551$  MHz. Transition strength factors  $C_j^2$  are computed for linearly polarized incident light.

## 3.8 Appendix A: Vapor cell absorption spectrum

### 3.8.1 Theory

We derive here the absorption spectrum of the Rb vapor cell, following the method described in Ref. [107]. For weak probe intensity, the transmission of a monochromatic wave of angular frequency  $\omega$  through an atomic vapor with uniform density is given by

$$\mathcal{T}_{\text{vapor}}(\omega, T) = e^{-\alpha(\omega, T)L}, \quad (3.4)$$

where  $L$  is the length of the vapor cell and  $\alpha(\omega, T)$  is the absorption coefficient of the atomic vapor, which is only dependent on the temperature  $T$ . Our cell contains  $^{85}\text{Rb}$  and  $^{87}\text{Rb}$  in natural abundance ( $\epsilon_{85} = 72.17\%$  and  $\epsilon_{87} = 27.83\%$ ) so that the total absorption reads  $\alpha(\omega, T) = \alpha_{85}(\omega, T) + \alpha_{87}(\omega, T)$ . For each isotope, we consider the six allowed electric dipole hyperfine transitions shown in Fig. 3.5a, which leads to the following expression for the absorption of isotope  $i$

$$\alpha_i(\omega, T) = \sum_{j=1}^6 \frac{n_i(T)}{2(2\mathcal{I}_i + 1) \hbar \epsilon_0} C_j^2 d^2 \times s_{\Gamma}^i(\omega - \omega_j, T), \quad (3.5)$$

where  $d = 5.177 e a_0$  (with  $a_0$  the Bohr radius) is the reduced dipole matrix element computed for the D2 line,  $C_j^2 = \sum_{m_F} c_j^2$  is the total strength coefficient of the degenerate hyperfine transition  $j$  (tabulated in Fig. 3.5b for linear incident polarization) and  $n_i(T)/[2(2\mathcal{I}_i + 1)]$  is the isotope atomic density per Zeeman sublevel.  $^{85}\text{Rb}$  and  $^{87}\text{Rb}$  have nuclear spins  $\mathcal{I}_{85} = 5/2$  and  $\mathcal{I}_{87} = 3/2$  and their relative density  $n_i(T) = \epsilon_i n(T)$  is obtained from the ideal gas law where the vapor pressure  $p(T)$  is given by equations (A.1) and (A.2) of Ref. [107]. Finally, the lineshape factor

$$s_{\Gamma}^i(\delta_j, T) = \int_{-\infty}^{+\infty} \frac{\Gamma/2}{(\Gamma/2)^2 + (\delta_j - kv)^2} \times \frac{1}{\sqrt{\pi}\sigma_i(T)} \exp\left(-\frac{v^2}{\sigma_i^2(T)}\right) dv, \quad (3.6)$$

corresponds to the Doppler broadened profile of the atomic transition  $j$ . We take the Lorentzian profile of the atom with natural linewidth  $\Gamma = 2\pi \times 6.065$  MHz (the experimentally measured decay rate of the  $5^2P_{3/2}$  atomic state [47]) integrated over the Gaussian distribution of atomic velocities parallel to the probe beam, with  $1/e$  width  $\sigma_i(T) = \sqrt{2k_B T/m_i}$  ( $k_B$  is the Boltzmann constant,  $m_i$  is the isotope atomic mass). At  $T = 24.8^\circ\text{C}$ , the thermal longitudinal motion of the atom leads to a full-width half maximum (FWHM) Doppler broadening  $\Delta\omega = 2\sqrt{\ln 2}\omega\sigma_i/c \simeq 2\pi \times 0.51$  GHz for the D2 line at 780 nm.

### 3.8.2 Experiment

Fig. 3.6 shows an experimental transmission spectrum of a 75 mm rubidium vapor cell measured using a tunable 780 nm external cavity diode laser (short term [100  $\mu\text{s}$ ] FWHM < 1 MHz) with linear incident polarization. The data are fitted using equations (3.4), (3.5) and (3.6), where the vapor temperature is the only free parameter. Excellent agreement is obtained for  $T = 24.8 \pm 0.2^\circ\text{C}$  (see solid line).

## 3.9 Appendix B: Theory of the QD response to a resonant field

### 3.9.1 First order coherence $g^{(1)}(\tau)$ and power spectrum $S(\omega_{sc})$

We aim at describing the resonance fluorescence (RF) power spectrum  $S(\omega_{sc})$  of a QD excited resonantly. To do so, we assume that the QD behaves as a two-level system. We follow the approach of Mollow[69] and extend it to include the additional pure dephasing associated to the extra coupling to the QD solid-state environment. We first evaluate the first order coherence  $g^{(1)}(t, \tau)$  of the field scattered by the QD, from which we can easily

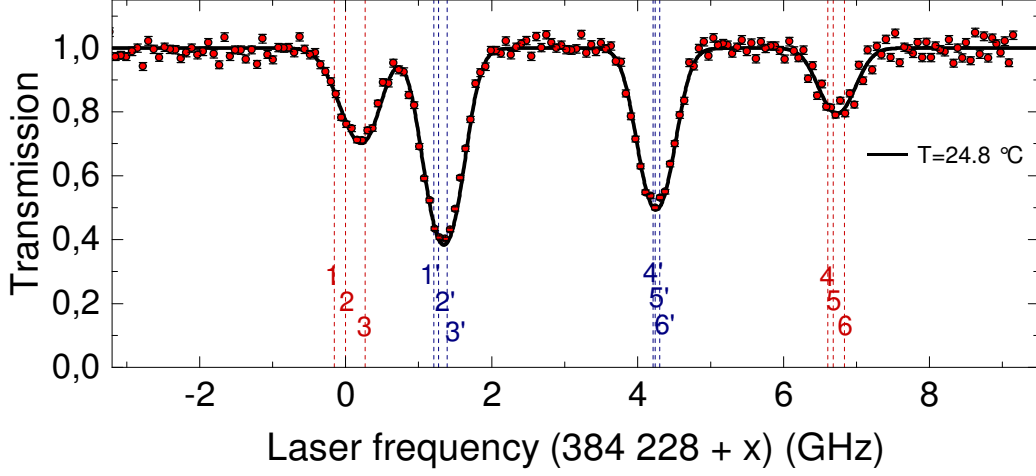


Figure 3.6: **Transmission of the Rb vapor cell.** The laser intensity is adjusted to the typical QD resonance fluorescence level of 5 kcts/s. The exposure time is 1 s per data point. Raw measurements are normalized using a linear baseline. The solid black line is a fit using equations (3.4), (3.5) and (3.6) with  $T = 24.8 \pm 0.2$  °C.

derive its power spectrum.

The two-level system has a ground state  $|g\rangle$ , excited state  $|e\rangle$  (decay rate  $\Gamma_{\text{sp}}$ ), and a transition angular frequency  $\omega_0$ . Neglecting retardation effects, the first-order coherence reads

$$g^{(1)}(t, \tau) = \frac{\langle \hat{\pi}^\dagger(t) \hat{\pi}(t + \tau) \rangle}{\langle \hat{\pi}^\dagger(t) \hat{\pi}(t) \rangle}, \quad (3.7)$$

$$\text{with } \begin{cases} \hat{\pi}^\dagger = |e\rangle \langle g|, & \langle \hat{\pi}^\dagger(t) \rangle = \tilde{\rho}_{ge}(t) e^{i\omega t} \\ \hat{\pi} = |g\rangle \langle e|, & \langle \hat{\pi}(t) \rangle = \tilde{\rho}_{eg}(t) e^{-i\omega t}, \end{cases} \quad (3.8)$$

where  $\tilde{\rho}_{ij}$  are the density matrix elements of the two-level system, and  $\pi^\dagger$  and  $\pi$  are atomic transition operators. The dynamics under coherent illumination are described by the optical Bloch equations [34]. The steady-state expectation values of the transition operators are computed in the interaction picture using the quantum regression theorem. The decay rates are  $1/T_1 = \Gamma_{\text{sp}}$  for the populations, and  $1/T_2 = \Gamma_{\text{sp}}/2 + \gamma^*$  for the coherences. Following the derivation of Ref. [69] we obtain the steady-state expression  $g^{(1)}(\tau) = \lim_{t \rightarrow \infty} g^{(1)}(t, \tau)$ ,

which, in the resonant case  $\omega = \omega_0$ , is given by

$$g^{(1)}(\tau) e^{i\omega\tau} = \frac{\Gamma_{\text{sp}}^2}{2\Omega^2 + \Gamma_{\text{sp}}^2 + 2\gamma^*\Gamma_{\text{sp}}} + \frac{1}{2} e^{-(\frac{\Gamma_{\text{sp}}}{2} + \gamma^*)\tau} + e^{-(\frac{3\Gamma_{\text{sp}} + 2\gamma^*}{4})\tau} \left[ \frac{P}{2} \cos \lambda\tau - \frac{Q}{2} \sin \lambda\tau \right], \quad (3.9)$$

with

$$\begin{cases} \lambda = \sqrt{\Omega^2 - \left(\frac{\Gamma_{\text{sp}}}{4} - \frac{\gamma^*}{2}\right)^2} \\ P = \frac{2\Omega^2 - \Gamma_{\text{sp}} + 2\gamma^*\Gamma_{\text{sp}}}{2\Omega^2 + \Gamma_{\text{sp}} + 2\gamma^*\Gamma_{\text{sp}}} \\ Q = \frac{\Omega^2(5\Gamma_{\text{sp}} - 2\gamma^*) - 2\gamma^{*2}\Gamma_{\text{sp}} + 2\gamma^*\Gamma_{\text{sp}}^2 - \Gamma_{\text{sp}}^3/2}{2\lambda(2\Omega^2 + \Gamma_{\text{sp}} + 2\gamma^*\Gamma_{\text{sp}})}. \end{cases}$$

The Fourier transform of  $g^{(1)}(\tau)$  gives the expression for the RF power spectrum

$$\begin{aligned} S(\omega_{\text{sc}}) = & \frac{\Gamma_{\text{sp}}^2}{2\Omega^2 + \Gamma_{\text{sp}}^2 + 2\gamma^*\Gamma_{\text{sp}}} \delta(\omega_{\text{sc}} - \omega_0) \\ & + \frac{1}{2\pi} \frac{\frac{\Gamma_{\text{sp}}}{2} + \gamma^*}{(\omega_{\text{sc}} - \omega_0)^2 + \left(\frac{\Gamma_{\text{sp}}}{2} + \gamma^*\right)^2} \\ & + \frac{1}{4\pi} \frac{\left(\frac{3}{4}\Gamma_{\text{sp}} + \frac{1}{2}\gamma^*\right) P - (\omega_{\text{sc}} - \omega_0 - \lambda)Q}{(\omega_{\text{sc}} - \omega_0 - \lambda)^2 + \left(\frac{3}{4}\Gamma_{\text{sp}} + \frac{1}{2}\gamma^*\right)^2} \\ & + \frac{1}{4\pi} \frac{\left(\frac{3}{4}\Gamma_{\text{sp}} + \frac{1}{2}\gamma^*\right) P + (\omega_{\text{sc}} - \omega_0 + \lambda)Q}{(\omega_{\text{sc}} - \omega_0 + \lambda)^2 + \left(\frac{3}{4}\Gamma_{\text{sp}} + \frac{1}{2}\gamma^*\right)^2}, \quad (3.10) \end{aligned}$$

which depends on three parameters only: the driving Rabi frequency  $\Omega$ , the radiative decay rate of the excited state  $\Gamma_{\text{sp}}$ , and the pure dephasing rate  $\gamma^*$ . Experimental RF spectra result from the convolution of (3.10) with the emission spectrum of the resonant laser. In practice, we use a highly coherent 780 nm external cavity diode laser, that we model by a Gaussian profile with a full width at half maximum of 1 MHz.

### 3.10. Appendix C: Experimental determination of the QD spontaneous emission rate and dephasing rate

---

#### 3.9.2 Second order coherence $g_{\text{TLS}}^{(2)}(\tau)$

Within the two-level system model (TLS), the second order coherence of the field scattered by the QD is given by

$$g_{\text{TLS}}^{(2)}(t, \tau) = \frac{\langle \hat{\pi}^\dagger(t) \hat{\pi}^\dagger(t + \tau) \hat{\pi}(t + \tau) \hat{\pi}(t) \rangle}{\langle \hat{\pi}^\dagger(t) \hat{\pi}(t) \rangle^2}. \quad (3.11)$$

As before, it is derived in the interaction picture using the quantum regression theorem. Using the same notations, we find

$$g_{\text{TLS}}^{(2)}(\tau) = 1 - e^{-\frac{3\Gamma_{\text{sp}} + 2\gamma^*}{4}\tau} \left( \cos \lambda\tau + \frac{3\Gamma_{\text{sp}} + 2\gamma^*}{4\lambda} \sin \lambda\tau \right), \quad (3.12)$$

which depends on the same three parameters  $\Omega$ ,  $\Gamma_{\text{sp}}$ , and  $\gamma^*$ .

## 3.10 Appendix C: Experimental determination of the QD spontaneous emission rate and dephasing rate

### 3.10.1 Results from the resonant excitation

In order to evaluate the QD spontaneous emission rate and dephasing rate, we perform a simultaneous fit ( $\chi^2$ -minimization) of 1) the Rb vapor transmission spectrum measured with single photons from the resonantly excited QD, and 2) the intensity correlation measurements (respectively Fig. 3b and Fig. 2d). As we used the same resonant laser intensity  $I_R = 141 \text{ nW}/\mu\text{m}^2$  in both experiments, the two data sets are fitted by a common set of the three parameters  $\Omega$ ,  $\Gamma_{\text{sp}}$ , and  $\gamma^*$  (see previous section). For each data set, the vertical error bars used in the  $\chi^2$ -minimization result from shot noise in the number of detected photons per time bin. We find  $\Omega/2\pi = 0.39 \pm 0.10 \text{ GHz}$ ,  $\Gamma_{\text{sp}}/2\pi = 1.42 \pm 0.12 \text{ GHz}$ , and  $\gamma^*/2\pi = 0 \pm \binom{0.10}{0} \text{ GHz}$ , where the error bars correspond to one standard deviation.

To appreciate the fit sensitivity, we plot in Fig. 3.7 the theoretical predictions corresponding to values of the fitting parameters differing by three standard deviations.

- The first column shows the predictions of the model obtained with the parameters from the best fit:  $\Omega = 2\pi \times 0.39 \text{ GHz}$ ,  $\Gamma_{\text{sp}} = 2\pi \times 1.42 \text{ GHz}$ , and  $\gamma^* = 2\pi \times 0 \text{ GHz}$ .
- The second column draws attention to the case of a non-zero pure dephasing  $\gamma^* = 2\pi \times 0.30 \text{ GHz}$  (+3  $\sigma$  value), with the constraint  $\Gamma_{\text{sp}} + 2\gamma^* = 2\pi \times 1.42 \text{ GHz}$  (total FWHM measured in Fig. 2a of the article). In this case, the coherent fraction of the



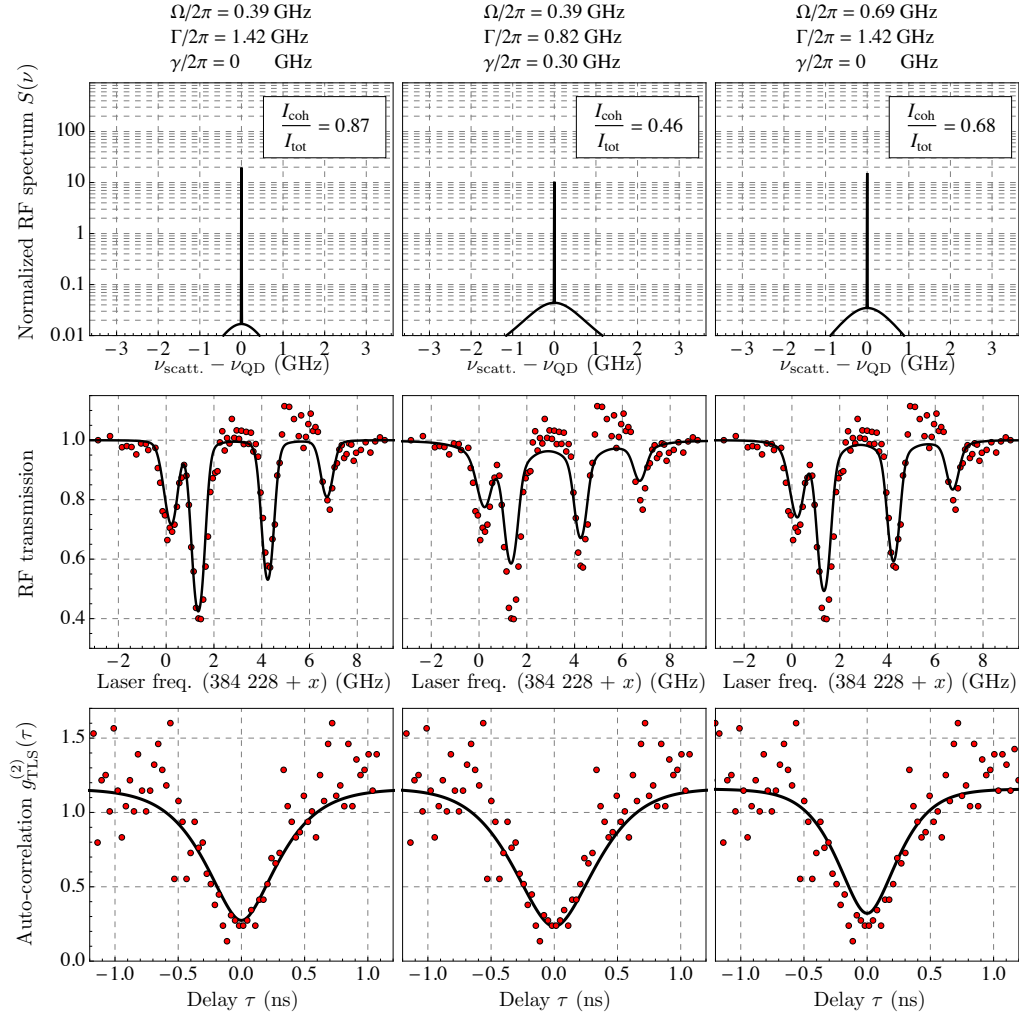


Figure 3.7: **Sensitivity on the fitting parameters.** First row: computed resonant QD spectrum. Second row: absorption spectrum under resonant excitation. Third row: second order correlation function. Open circles correspond to the experimental data.

scattered light decreases to 70%, such that the absorption peaks on the transmission spectrum become broader and shallower.

- The last column shows the predictions of the model with larger Rabi frequency  $\Omega = 2\pi \times 0.69$  GHz (+3  $\sigma$ -value), keeping  $\Gamma_{\text{sp}}$  and  $\gamma^*$  at optimal values. A close examination shows that the absorption peaks on the transmission spectrum also become broader and shallower, and the rise time at the dip of the intensity auto-correlation becomes slightly shorter.

3.10. Appendix C: Experimental determination of the QD spontaneous emission rate and dephasing rate

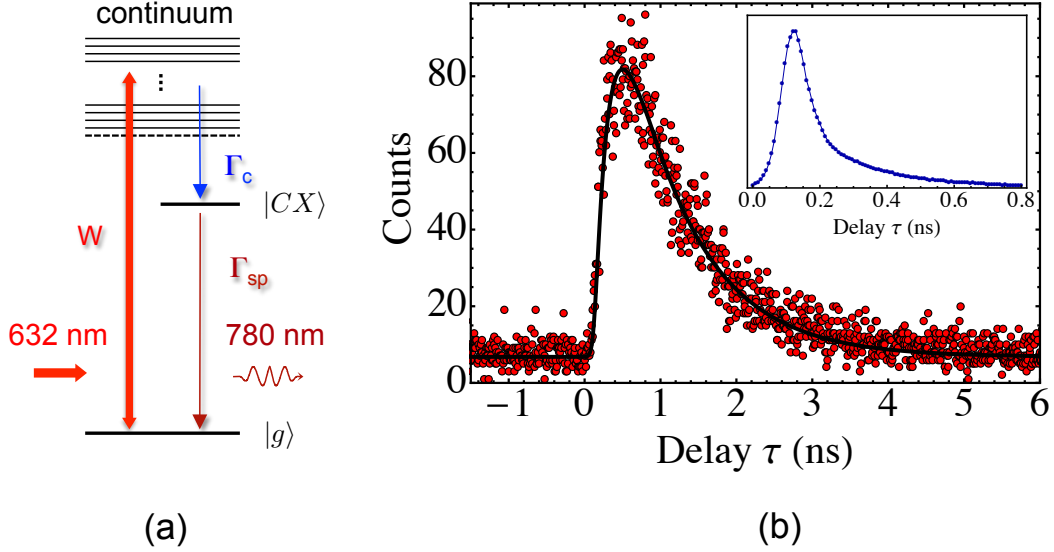


Figure 3.8: **Decay-time measurements.** (a) Non-resonant excitation scheme. (b) Histogram of the QD photons arrival time (8 ps time bins, integration time 2 minutes). The solid line is a fit using Eq. (3.13) convoluted by the measured instrument response (FWHM = 100 ps, see inset) and scaled to the signal amplitude, with  $\Gamma_{sp} = 2\pi \times 1.7$  GHz and  $\Gamma_c = 2\pi \times 176$  MHz.

As an additional consistency check, we can fit the dependence of the FWHM of the RF spectrum  $\Gamma$  (Fig. 2b) with laser intensity using the expression  $\Gamma(I_R) = \sqrt{\Gamma_{sp}^2 + 2AI_R}$ , with the value of  $\Gamma_{sp}$  obtained above and an adjustable coefficient  $A$ . Best agreement is obtained for  $A = 0.34 \times 10^{17} (\text{rad/s})^2/(\text{nW}/\mu\text{m}^2)$ . From this fit, the Rabi frequency corresponding to the operating resonant intensity  $I_R = 141 \text{ nW}/\mu\text{m}^2$  that we extract is  $\Omega = \sqrt{AI_R} = 2\pi \times 0.35$  GHz, in excellent agreement with the value obtained from the previous analysis.

### 3.10.2 Decay-time measurements under non-resonant excitation

In order to confirm the value for the spontaneous emission rate of the QD upper level, we perform decay-time measurements with a non-resonant pulsed laser ( $\lambda = 635$  nm,  $\simeq 90$  ps pulses, 80 MHz repetition rate). The dynamics of the population  $N_{CX}(t)$  are well described by Einstein rate equations with two distinct rates:  $\Gamma_c$ , the relaxation from the continuum to the QD excitonic state, and  $\Gamma_{sp}$ , the radiative decay rate to the QD ground state (see Fig. 3.8a). Assuming that the system is initially excited in the continuum, the population of

the state  $|CX\rangle$  takes the form

$$N_{CX}(t) = \frac{\Gamma_c}{\Gamma_c - \Gamma_{sp}} (e^{-\Gamma_{sp}t} - e^{-\Gamma_c t}). \quad (3.13)$$

The result from our measurements is shown in Fig. 3.8b for low excitation power. The fit of the data yields a high rate (small lifetime) of  $2\pi \times (1.7 \pm 0.2)$  GHz ( $\simeq 90$  ps) and a slow rate (long lifetime) of  $2\pi \times (176 \pm 3)$  MHz ( $\simeq 900$  ps). This is completely consistent with the Rb cell spectroscopy and  $g^{(2)}$  results provided the high rate is associated to radiative decay, and the slow rate to relaxation, an association which we have confirmed with pulsed resonant excitation (data not shown). The relationship of the relaxation and decay rates is contrary to the standard interpretation for InGaAs QDs, for which relaxation is much faster than radiative decay. We speculate that the presence of a tunnel barrier between the QDs and the nearby wetting layer (the ring-shaped AlGaAs mound, cf. Fig. 3.1), combined with the indirect bandgap in the Al-rich AlGaAs surrounding matrix are responsible for the unusually slow relaxation dynamics. Of course, the decay curves determines the total decay rate not necessarily the radiative decay rate. However, we are working here with MBE-grown GaAs of very high quality at low temperature where it is safe to assume that non-radiative decay processes are weak such that spontaneous emission represents the dominant decay process.

The radiative lifetime is rather short and corresponds to an oscillator strength of  $\sim 100$ . The oscillator strength is around 10 in the strong confinement regime [108] (quantization energy much larger than the Coulomb energy) rising to well above 100 in the weak confinement regime [109]. In this case the result, similar in fact to that of interface fluctuation quantum dots [110], shows that the quantum dot is in the intermediate confinement regime.

## 3.11 Appendix D: Complementary information on the blinking in the QD signal

### 3.11.1 QD1 second order correlation function at long delays

For the correlation measurements, we position a hemispherical solid-immersion lens on the surface of the sample, thereby increasing the count rates by a factor of  $\sim 4$ . Fig. 3.9 extends the data shown in Fig. 3.2d to longer delays. We clearly observe a bunching dynamics with a correlation time on the order of 600 ns. The count rate for this experiment was  $2 \times 10^3$  cts/s,

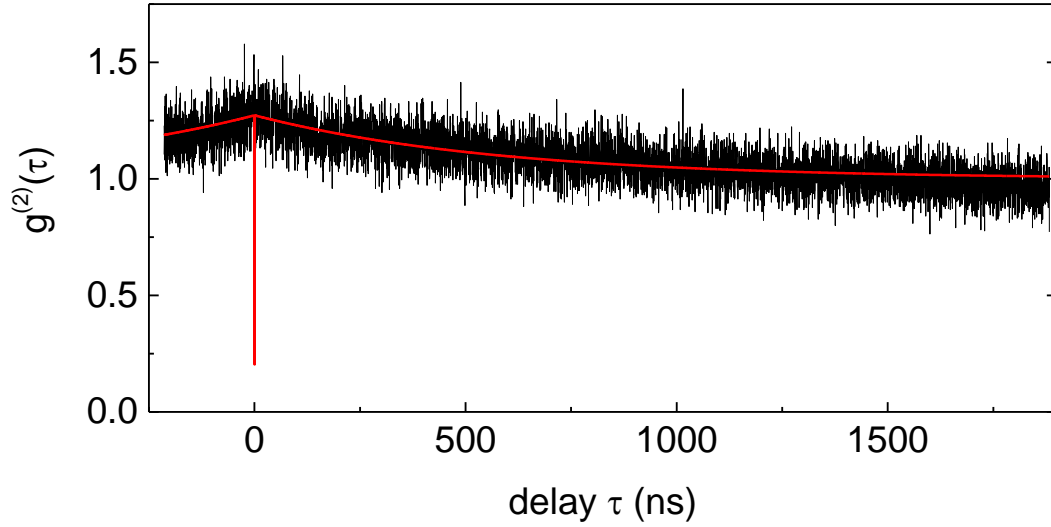


Figure 3.9: **QD1  $g^{(2)}(\tau)$ -function at long delays.** Experimental data (black), and a fit (red) using Eq. (3.3), with  $\tau_c = 580$  ns and  $\beta = 0.8$ .

so that we can exclude any artefact from the detector[111].

### 3.11.2 Effect of the non-resonant contribution on the RF signal

Fig. 3.10 shows the effect of an increasing non-resonant contribution on the resonance fluorescence intensity of the neutral and charged excitons. The data is recorded on QD2 and the data points correspond to the same non-resonant intensities as used in Fig. 3.4. We note that the values reported here are calculated assuming a perfectly focused beam. Our objective lens is however mono-chromatic and its focus adjusted to maximize collection efficiency at 780 nm.

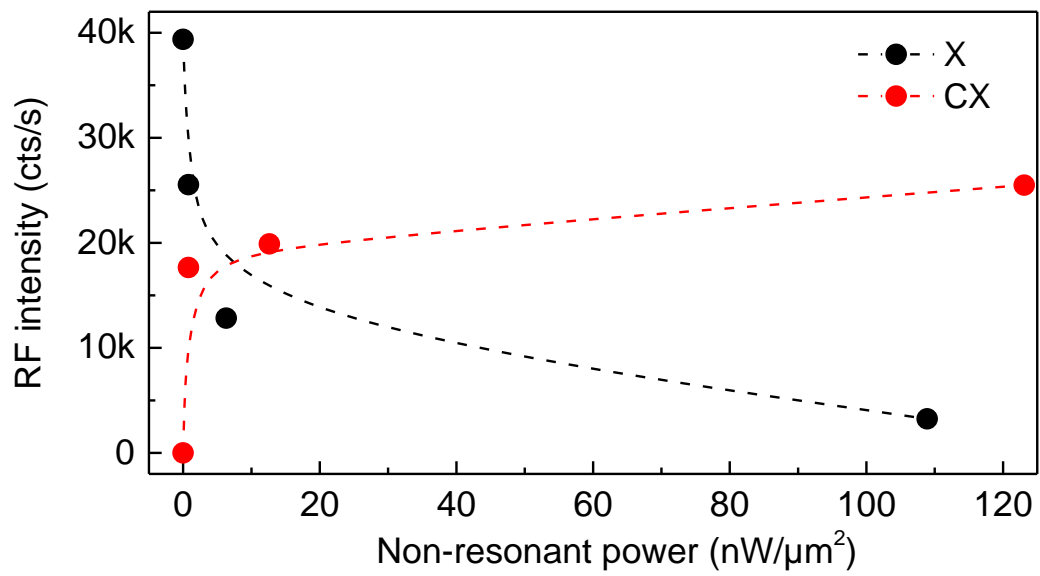


Figure 3.10: **Influence of the non-resonant pump on the RF signal.** Dashed lines are guides to the eyes.

*3.11. Appendix D: Complementary information on the blinking in the QD signal*

---

## Chapter 4

# On-demand semiconductor source of 780-nm single photons with controlled temporal wave packets

Adapted from: “On-demand semiconductor source of 780 nm single photons with controlled temporal wave packets”

Phys. Rev. B **97**, 205304 - Published 21. May 2018

Lucas Béguin<sup>1</sup>, Jan-Philipp Jahn<sup>1</sup>, Janik Wolters<sup>1</sup>, Marcus Reindl<sup>2</sup>, Yongheng Huo<sup>2</sup>, Rinaldo Trotta<sup>2</sup>, Armando Rastelli<sup>2</sup>, Fei Ding<sup>3</sup>, Oliver G. Schmidt<sup>4</sup>, Philipp Treutlein<sup>1</sup>, Richard J. Warburton<sup>1</sup>

- 1 – Department of Physics, University of Basel, Klingelbergstrasse 82, CH-4056 Basel, Switzerland
- 2 – Institute of Semiconductor and Solid State Physics, Johannes Kepler University Linz, Altenbergerstrasse 69, A-4040 Linz, Austria
- 3 – Institut für Festkörperphysik, Leibniz Universität Hannover, Appelstrasse 2, D-30167 Hannover, Germany
- 4 – Institute for Integrative Nanosciences, IFW Dresden, Helmholtzstrasse 20, D-01069 Dresden, Germany

### 4.1 Abstract

We report on a fast, bandwidth-tunable single-photon source based on an epitaxial GaAs quantum dot. Exploiting spontaneous spin-flip Raman transitions, single photons at 780 nm are generated on-demand with tailored temporal profiles of durations exceeding the intrinsic

quantum dot lifetime by up to three orders of magnitude. Second-order correlation measurements show a low multi-photon emission probability ( $g^2(0) \sim 0.10 - 0.15$ ) at a generation rate up to 10 MHz. We observe Raman photons with linewidths as low as 200 MHz, narrow compared to the 1.1 GHz linewidth measured in resonance fluorescence. The generation of such narrow-band single photons with controlled temporal shapes at the rubidium wavelength is a crucial step towards the development of an optimized hybrid semiconductor-atom interface.

## 4.2 Introduction

The distribution of quantum states and entanglement between remote systems within a quantum network [23] enables a vast range of technological breakthroughs from secure communications [30] to computational speed-up [112] and quantum-enhanced global sensing [113]. In this framework, single photon sources are essential resources that allow matter qubits at stationary network nodes to be interconnected [39, 114, 115]. For most of these applications, controlling the spectral and temporal properties of the single photons is a crucial requirement. Indeed, the performance of quantum protocols based on two- or single-photon interference critically depends on the degree of coherence of the individual photons: the coherence limits the achievable coalescence contrast in two-photon interference experiments [116]. Single-photon wave packets should therefore be generated in a well-defined spatio-temporal mode with a Fourier-transform-limited spectrum. The ability to tailor the photons' carrier frequencies, spectral widths and temporal profiles is essential to ensure efficient coupling between remote heterogeneous systems [117].

In particular, control over the temporal profile, the waveform, of the single photons is important for a number of reasons. First, "long" single photons with narrow spectra are required for an efficient interaction with media featuring sharp absorption lines such as atomic species or solid-state color centers. Secondly, protocols for long-distance entanglement distribution require path length differences stabilized to within the temporal "length" of the single photon wave packets [118], and the use of long photons thus relaxes these requirements. Finally, fine control of the temporal profile enables the coupling efficiency between single photons and atoms [119, 120] or between single photons and optical cavities [121] to be optimized. Numerous approaches to generate single photons with tunable spectro-temporal properties have been investigated using cavity-enhanced spontaneous parametric down conversion [122, 123, 124, 125], single atoms [126, 127, 128] or ions [129, 130] in a cavity, hot [131, 132, 133, 134] and cold [11, 135, 136, 137, 138, 139, 140, 141] atomic ensembles, trapped ions in free space [142], and quantum dots [14, 143, 144, 145, 146, 147].



Among all single photon emitting devices, semiconductor quantum dots (QDs) embedded in dedicated photonic nanostructures are highly promising single photon sources. QD sources combine simultaneously large photon extraction, high brightness and near-perfect levels of purity and indistinguishability [6, 26], all in a fast and robust device. These properties are not shared by any other source. An exciton, an electron-hole pair, mimics a two-level system in these devices. However, exciton recombination takes just a few hundred picoseconds such that QDs usually generate single photons with GHz linewidths. This linewidth far exceeds the bandwidth of prototypical single photon memories. A specific and important example is an ensemble of atoms which have excellent properties for a photon memory [88] but only in a narrow bandwidth, typically  $\sim 10$  MHz. Interfacing GHz-bandwidth single QD photons with atomic memories is therefore highly inefficient on account of the bandwidth mismatch.

Finding a way to control the spectro-temporal properties of QD photons represents a key challenge. In this direction, several methods have been investigated. A first temporal shaping demonstration implemented fast electro-optic amplitude modulation synchronized with the photon generation to temporally filter preselected profiles from exponentially decaying envelopes [144]. Although this method can help to improve the degree of indistinguishability of a noisy source, it works by introducing losses that significantly reduce the single photon generation efficiency. Another approach exploited weak resonant excitation to generate highly coherent, indistinguishable photons with tailored waveforms via Rayleigh scattering [14]. Although the spectral properties in continuous wave excitation can approach the bandwidth of the driving-laser, pulsed excitation cannot yield true single photons with wave packet durations exceeding the lifetime of the two-level system. Therefore, the lower bound on the bandwidth of QD single photons is still dictated by the inverse of the exciton decay time. An additional drawback lies in the probabilistic nature of this excitation scheme, ruling out its applicability as an on-demand source of tailored single photons.

The two-level exciton offers a too restrictive set of possibilities. Inspired by experiments on trapped ions [148, 149], a much more powerful approach is to create a three-level system, specifically a  $\Lambda$ -system, by trapping a single electron or hole in the QD. A  $\Lambda$ -system is created on application of a magnetic field. The main idea is to generate a single photon with tailored waveform by driving the spin from one spin state to the other, a Raman process. While Raman scattering from QD  $\Lambda$ -systems is established [143, 145], forming in fact the basis for recent demonstrations of remote spin entanglements [72, 150], the creation of on-demand single-photons with user-defined temporal profiles is not.

Here, we demonstrate high-rate, on-demand generation of single photons with tailored temporal wave packets from a QD. The QD is spectrally matched to the rubidium D2 line.

### 4.3. Scheme

Such a versatile single photon source opens up important applications in heterogeneous quantum networking, combining tailored single photons with broadband atomic quantum memories [151, 29].

### 4.3 Scheme

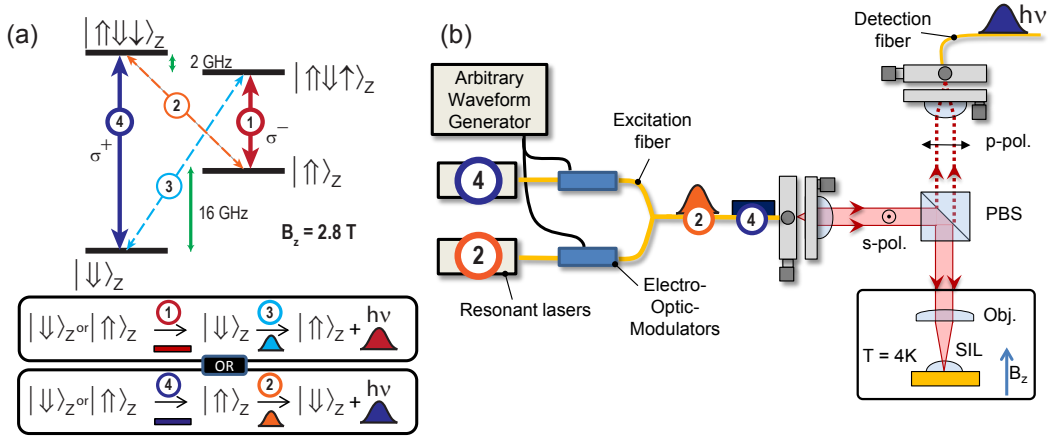


Figure 4.1: (a) Reduced energy level diagram of a quantum dot charged with a single hole subject to a magnetic field in the Faraday geometry. The inset illustrates the two-step sequence used for generating a “red” or “blue” single Raman photon with controlled temporal waveform. (b) Polarization-based dark-field microscope with tailored excitation pulses.

We consider a QD charged with a single hole. The ground states correspond to the two hole spin states  $|\uparrow\rangle_z$  and  $|\downarrow\rangle_z$ ; the excited states to the two trion  $X^{1+}$  states  $|\uparrow\uparrow\downarrow\rangle_z$  and  $|\downarrow\uparrow\downarrow\rangle_z$  consisting of two spin-paired holes and a lone electron spin. In a magnetic field along the growth direction, the degeneracies between the ground states and the excited states are lifted according to the out-of-plane  $g$ -factors  $g_h$  and  $g_e$ , respectively (Fig. 4.1(a)). For a pure heavy-hole state, selection rules dictate that only the “vertical” spin-preserving transitions (① and ④) are allowed with orthogonal circular polarization ( $\sigma^-$  and  $\sigma^+$ , respectively). In practice, the “diagonal” spin-flipping transitions (② and ③) are also weakly allowed by heavy hole-light hole mixing or by the hyperfine interaction (the nuclear spins induce a slight tilt of the quantization axis) [43]. This means that each trion state possesses two spontaneous decay channels, one fast, the other slow. This is described as a  $\Lambda$ -system with a very asymmetric branching ratio,  $\gamma/(\Gamma + \gamma) \ll 1$ , where  $\Gamma$  and  $\gamma$  are the “allowed” and “forbidden” spontaneous decay rates. As a result, optical spin pumping is achieved

by resonantly driving the strong spin-preserving transitions until the trion spontaneously decays via the weak spin-flipping transitions [152, 153]. Once the QD spin state has been initialized, a single photon can be generated by driving the weak “diagonal” spin-flipping transition of the  $\Lambda$ -system. A single photon is generated on driving the spin from one spin state to the other. This is a Raman process. The asymmetric branching ratio ensures that the purity of the photon scattered in the spontaneous Raman process is not limited by an otherwise broad emission time distribution [149].

## 4.4 Experimental setup and methods

The experiments are performed on GaAs epitaxial QDs obtained by droplet etching and overgrowth, embedded in an  $\text{Al}_{0.4}\text{Ga}_{0.6}\text{As}$  matrix at 4.2 K [53]. The photoluminescence from the ensemble is centered around 780 nm. QDs in the ensemble can be brought into resonance with the Rb D2 line using strain tuning as detailed in chapter 3. This is a powerful feature. However, the spin properties of these QDs are presently unexplored. In particular, spin-pumping has not previously been achieved on these QDs.

An additional low-power nonresonant laser at 633 nm is used to induce charges in the QD vicinity that are able to tunnel into the QD and change its charge state [102]. Here, we study the line identified as the positively charged exciton  $X^{1+}$  of one single QD. The identification is based on the widely different  $g$ -factors of electrons and holes in GaAs [51]; the electron  $g$ -factor is assumed to be negative. The QD is subjected to a magnetic field of 2.8 T along the sample growth axis and parallel to the optical axis (Faraday geometry) resulting in a pair of spin-preserving optical transitions. For the chosen QD, the electron and hole  $g$ -factors are determined to be  $g_e = -(0.05 \pm 0.01)$  and  $g_h = (0.41 \pm 0.02)$  based on the energy splittings of the four transitions. The two spin-preserving transitions are separated in frequency by  $\approx 18$  GHz (Fig. 4.1(a)).

Figure 4.1(b) shows the polarization-based dark-field microscope used to collect the resonance fluorescence on resonant excitation [86]. Linearly-polarized laser light propagates in a single mode through an excitation port, and the orthogonally-polarized light scattered by the QD is collected at a separate detection port. A polarizing beam splitter separates the scattered light from the excitation. Exquisite fine control of the polarization suppresses back-scattered laser light at the detection port up to 80 dB, and we observe resonance fluorescence (RF) with a signal-to-background ratio up to 100 : 1. A  $\text{ZrO}_2$  solid-immersion lens mounted onto our sample in combination with an aspheric lens of numerical aperture of 0.77 enhances the collection efficiency.

Electro-optic intensity modulators (EOM, Jenoptik, 200 ps rise time) driven by a fast arbitrary waveform generator (AWG, Tektronik 7122C) allow excitation pulses with tailored intensity profiles to be generated. The QD output is coupled into a fiber and guided either to a spectrometer equipped with electron multiplying charge coupled device or to single photon detectors (APDs) connected to a time-correlated single-photon counting module (Pico-harp 300). The photons' temporal profiles are reconstructed with a resolution of 512 ps by recording histograms of APD detection events.

To study the spectral properties of the QD photons, we added a Fabry-Pérot etalon (FP) to the detection arm (12.9 GHz free spectral range, 250 MHz linewidth). The FP is frequency tuned via a heater, and the temperature is feedback-controlled; the FP has high long-term stability. A spectrum is obtained by recording the number of detected photons after the FP etalon during 100 s as a function of the etalon detuning  $\Delta_{\text{FP}}$ .

## 4.5 QD spin dynamics

First, we demonstrate the optical initialization of the QD hole spin in the Faraday geometry. We work initially at moderate nonresonant (633 nm) laser intensities ( $0.15 \text{ nW}/\mu\text{m}^2$ ). The resonance fluorescence (RF) spectrum of  $X^{1+}$  is shown in Fig. 4.2(a). The red (blue) curve displays the rate of QD photons detected on the spectrometer around the spin-preserving transition frequency ① (④) as we scan the frequency of a continuous wave (CW) excitation laser above saturation. The red (blue) RF peak is well fitted by a (power-broadened) lorentzian profile, except for a dip observed when the scanning laser is resonant with the spin-flipping transition ② (③). Qualitatively, such dips in the RF signals show the enhancement of the optical spin pumping in which the spin, initially in a statistical mixture of the two spin states, is driven into one of the spin states.

To access the spin pumping and relaxation dynamics, we implement an all-optical method similar to Ref. [154] based on time-resolved resonance fluorescence (TRRF) measurements. The two-color excitation sequence is illustrated in Fig. 4.2(b). Acousto-optic modulators are used to create pulses from two CW lasers, resonant with the spin-preserving transitions ① and ④ respectively, which alternately pump the spin into  $|\downarrow\rangle_z$  and  $|\uparrow\rangle_z$ . Figure 4.2(b) displays the TRRF signals when the pulses drive the spin-preserving transitions well-above saturation. Exponential fits (not shown) indicate optical spin pumping times  $\tau_{\text{opt}} = 50 \text{ ns}$  ( $\sim 2/\gamma$ ). The spin pumping time is much larger than the radiative emission time, 330 ps for this QD. This represents an experimental demonstration that the branching ratio is highly asymmetric  $\gamma/(\gamma + \Gamma) \sim 1 : 75$ .

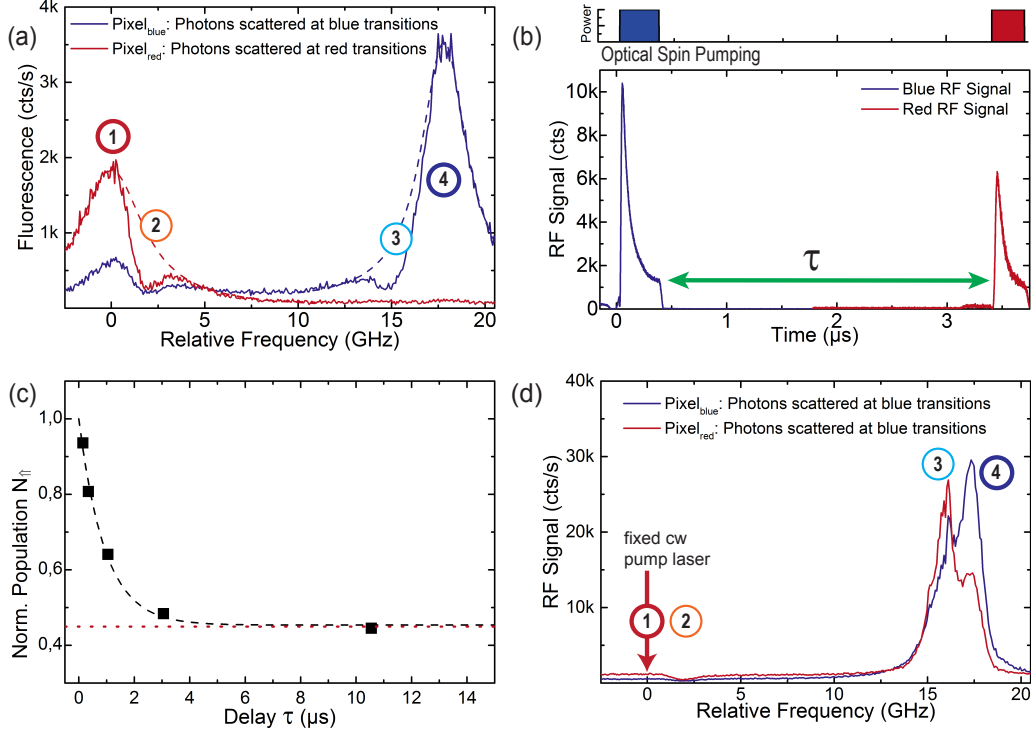


Figure 4.2: Observation of optical spin pumping. (a)  $X^{1+}$  resonance fluorescence (RF) spectrum in the Faraday configuration at  $B_z = 2.8$  T. Light scattered on the red transitions {①, ②} (red trace) and on the blue transitions {③, ④} (blue trace) are detected on two neighboring pixels of the CCD-spectrometer (9 GHz resolution), with residual leakage of the red RF signals from the transitions {①, ②} also detected on the “blue” pixel. The dip in the red (blue) trace compared to the fitted Lorentzian profile (dashed line) shows the enhancement of the optical spin pumping that depopulates the ground state  $|\uparrow\rangle_z$  ( $|\downarrow\rangle_z$ ) when the driving laser is resonant with the spin-flipping transition ② (③). (b) Time-resolved fluorescence observed under pulsed resonant excitation, alternately pumping the transition ④ and ① at saturation with a delay  $\tau$ . The exponential decays result from optical spin pumping that sequentially prepares  $|\uparrow\rangle_z$  and  $|\downarrow\rangle_z$  with time constant  $\tau_{\text{opt}} = 50$  ns. (c) Spin relaxation dynamics. The exponential fit (dashed line) gives an effective  $1/e$  spin thermalization time of  $0.95 \mu\text{s}$ . Dotted line shows Boltzmann equilibrium. (d) Same as (a) but with additional CW laser (1) driving the spin-preserving transition ① at saturation. The spin remains optically pumped in  $|\downarrow\rangle_z$  except when the scanning laser is resonant with the spin-preserving transition ④ (photon scattering at transitions ① and ④) or the spin-flipping transition ③ (photon scattering mostly at transition ①, with residual leak of red fluorescence counted on the blue pixel).

In a next step, the spin relaxation dynamics are investigated by increasing the delay  $\tau$  between the two resonant pulses. Just after a 400 ns pulse on transition ④, the spin is initialized in ground state  $|\uparrow\rangle_z$ . Without laser excitation, the spin flips from  $|\uparrow\rangle_z$  to  $|\downarrow\rangle_z$  ( $|\downarrow\rangle_z$  to  $|\uparrow\rangle_z$ ) at a rate  $\gamma_{\uparrow\downarrow}$  ( $\gamma_{\downarrow\uparrow}$ ) due to interaction with its environment. When the next pulse on transition ① arrives, the RF signal amplitude is proportional to the spin population left in  $|\uparrow\rangle_z$ . Figure 4.2(c) shows the decay of the population  $N_{\uparrow}$  as the delay  $\tau$  increases. By solving rate equations, the populations ( $N_{\uparrow}, N_{\downarrow}$ ) both relax to Boltzmann equilibrium  $N_{\uparrow}/N_{\downarrow} = \gamma_{\downarrow\uparrow}/\gamma_{\uparrow\downarrow} = \exp(-g_h\mu_B B/k_B T)$  at an effective rate  $\gamma_{\text{eff}} = \gamma_{\uparrow\downarrow} + \gamma_{\downarrow\uparrow}$ . By fitting the decay of  $N_{\uparrow}$  with an exponential, we extract an effective spin relaxation time  $\gamma_{\text{eff}}^{-1}$  of  $0.95 \mu\text{s}$  which corresponds to a spin lifetime  $\gamma_{\uparrow\downarrow}^{-1}$  of  $1.75 \mu\text{s}$  at 2.8 T. The optical spin pumping is thus much faster than the spin relaxation dynamics ( $\tau_{\text{opt}}^{-1}/\gamma_{\uparrow\downarrow} \sim 35$ ) which enables fast and efficient spin ground state preparation.

Finally, the ability to drive the weak cross transitions is demonstrated in Figure 4.2(d). A CW laser (1) resonantly drives the red spin-preserving transition ① at saturation, and a RF spectrum is recorded as the frequency of a second CW scanning laser (2) is tuned across the optical transitions. In this experiment, the red RF signal is almost constant at 1.2 kcts/s over the scanning range, as laser (1) keeps on driving transition ①. However, it reduces when the scanning laser (2) becomes resonant with the spin-flipping transition ②. Moreover, a new peak is clearly observed when the scanning laser (2) comes into resonance with the spin-flipping transition ③. This demonstrates that the spin-flipping transitions can be driven in the Faraday geometry, i.e. with an in-plane polarization. Tuned to resonance ②, laser (2) enhances the spin pumping achieved with laser (1). Tuned to resonance ③, laser (2) disrupts the spin pumping achieved with laser (1). The ratio of the red RF signals when spin pumping is disrupted or present gives a spin preparation efficiency of 95 %.

We note that in our sample, the QD charge state is randomized more quickly under higher nonresonant intensity, effectively increasing the hole spin relaxation rates and decreasing the spin preparation efficiency. This represents useful *in situ* control. For instance, the basic spectroscopy to establish the frequencies of the transitions can be conducted at high ( $> 30 \text{ nW}/\mu\text{m}^2$ ) nonresonant excitation (suppressed spin pumping, large RF signals); photon shaping is then implemented at low ( $0.03 \text{ nW}/\mu\text{m}^2$ ) nonresonant excitation (high efficiency spin pumping  $\geq 95 \%$ ).

These experiments establish all the features required for generating single photons with a Raman process, namely spin initialization via optical pumping and a “diagonal” spin-flipping transition which can be driven in the Faraday geometry.

## 4.6 Raman single-photon pulse shaping

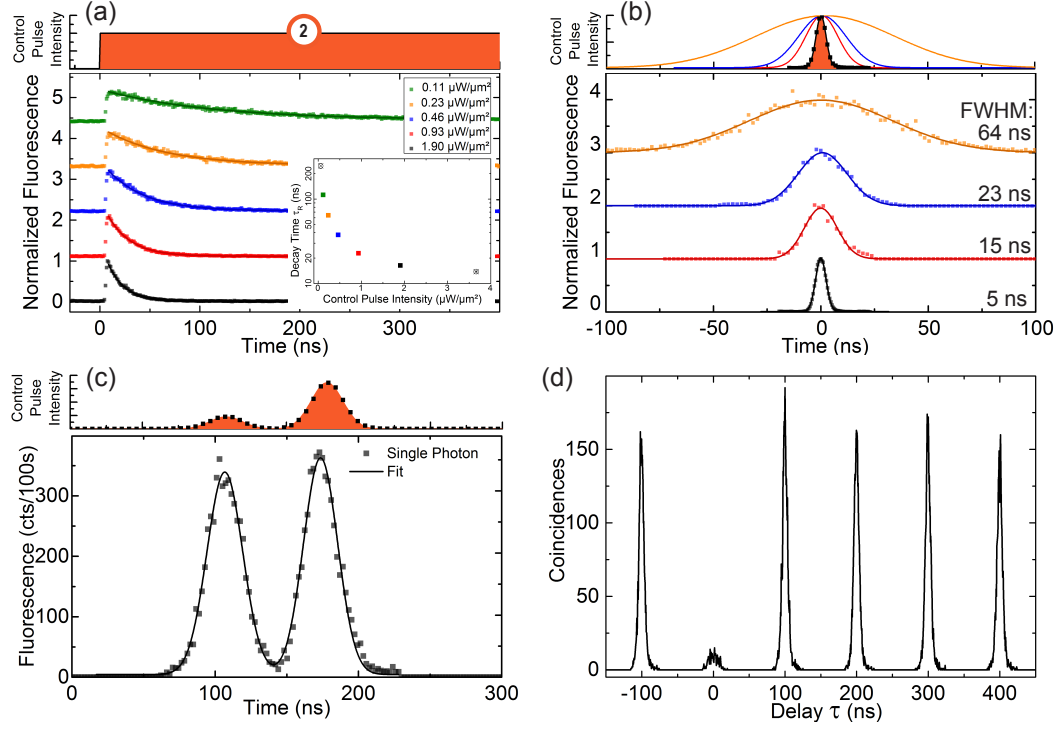


Figure 4.3: Single-photon pulse shaping. (a) Exponential photon waveforms obtained with a square control pulse. The single photon waveforms are shown (with an offset for visibility) as the intensity of the control pulse decreases. Inset: Tuning of the Raman photon duration  $\tau_R$  with control pulse intensity. (b) Gaussian photon waveforms (gaussian control pulses) with FWHM duration of 5, 15, 23 and 64 ns respectively. (c) Double gaussian photon waveform. Each curve from (a) to (c) corresponds to 10 min integration, and 2 ns time resolution. (d) Intensity autocorrelation of Raman photons with gaussian waveform (FWHM = 5 ns, 10 MHz repetition rate, 11 h acquisition).

We demonstrate the pulsed generation of single Raman photons with tailored waveforms. We use a two-color excitation sequence similar to Fig. 4.2(b), addressing the transitions ④ and ②. In a first step, the spin is prepared in  $|\uparrow\rangle_z$  using a pump pulse (50 – 200 ns) on resonance with transition ④. Subsequently, a second control pulse with frequency  $\nu_L$  drives the spin-flipping transition ② of frequency  $\nu_2$  at a detuning  $\Delta_L = \nu_L - \nu_2$ . The sequence is repeated at a rate up to 10 MHz. The concept is to induce a single spin-flip along with the emission of a single blue Raman photon. (The reverse scheme starting in  $|\downarrow\rangle_z$  and emitting a red Raman photon by driving the weak transition ③ is an equivalent concept). By adjusting the temporal envelope of the control pulse, a user-defined temporal structure

is imprinted on the Raman photon waveform.

Figures 4.3(a-c) show photon waveforms obtained for different control pulses shapes close to resonance ( $\Delta_L = 0$ ). With square control pulses (Fig. 4.3(a)), the quantum dot output exhibits an abrupt onset (limited by the rise time of the EOM) followed by an exponential decrease in the trailing edge with time constant  $\tau_R$ . By decreasing the control pulse power, we can adjust the duration  $\tau_R$  of the single photons from 14 ns to 245 ns, which is respectively about two and three orders of magnitude longer than the intrinsic radiative lifetime of the trion states (330 ps). With the perspective of optimizing the interface of our single-photon source with a rubidium quantum memory [78], we also demonstrate the ability to tailor the temporal envelopes of the single photon wave packets. An efficient starting point for memory optimization is to use gaussian profiles of chosen duration. Using gaussian control pulses, we generate gaussian single photons of full-width-at-half-maximum (FWHM) duration ranging from 5 ns to 64 ns (Fig. 4.3(b)).

As a final example, a more complex pulse shape, we address the possibility of splitting a single photon over two distinct time bins. Such photons have application in robust long-distance quantum communication protocols [155, 156, 157, 158]. To do this, we apply a double gaussian waveform to the control laser. The quantum dot output mimics the control (Fig. 4.3(c)).

To confirm the single-photon nature of the Raman light stream, we measured the second-order coherence for each temporal waveform using a standard Hanbury Brown-Twiss (HBT) setup. The two APDs were gated such that only photons emitted during the Raman generation phase (and not the initialization phase) were counted. The observed coincidences form a series of spikes separated by the sequence period, each with a shape related to the photon wave packet. A nearly vanishing peak at zero delay demonstrates that at most one single Raman photon is emitted during one sequence. Residual counts due to laser background are negligible compared to the Raman signal and are not subtracted in the data shown. The raw multi-photon emission probability ( $g^2(0)$ ) is extracted by computing the ratio of coincidence events of the central peak to the mean of the next five neighboring peaks. Figure 4.3(d) shows the intensity correlation histogram obtained for the 5 ns gaussian photons with  $g^2(0) = 0.12$ . Similar values were obtained for all the different waveforms: 0.10-0.15 for exponentials, 0.12-0.33 for gaussians and 0.26 for the double gaussian. Residual coincidences originate from the detection of photons off-resonantly scattered by the QD either on transition ① before the Raman flip, or on transition ④ after the emission of the first Raman photon, i.e. after the spin has flipped to  $|\downarrow\rangle_z$ . No selection rules in the Faraday configuration prohibit the linearly polarized control laser from driving off-resonantly the transitions ① and ④. In practice, we find that the control laser intensity and detuning can



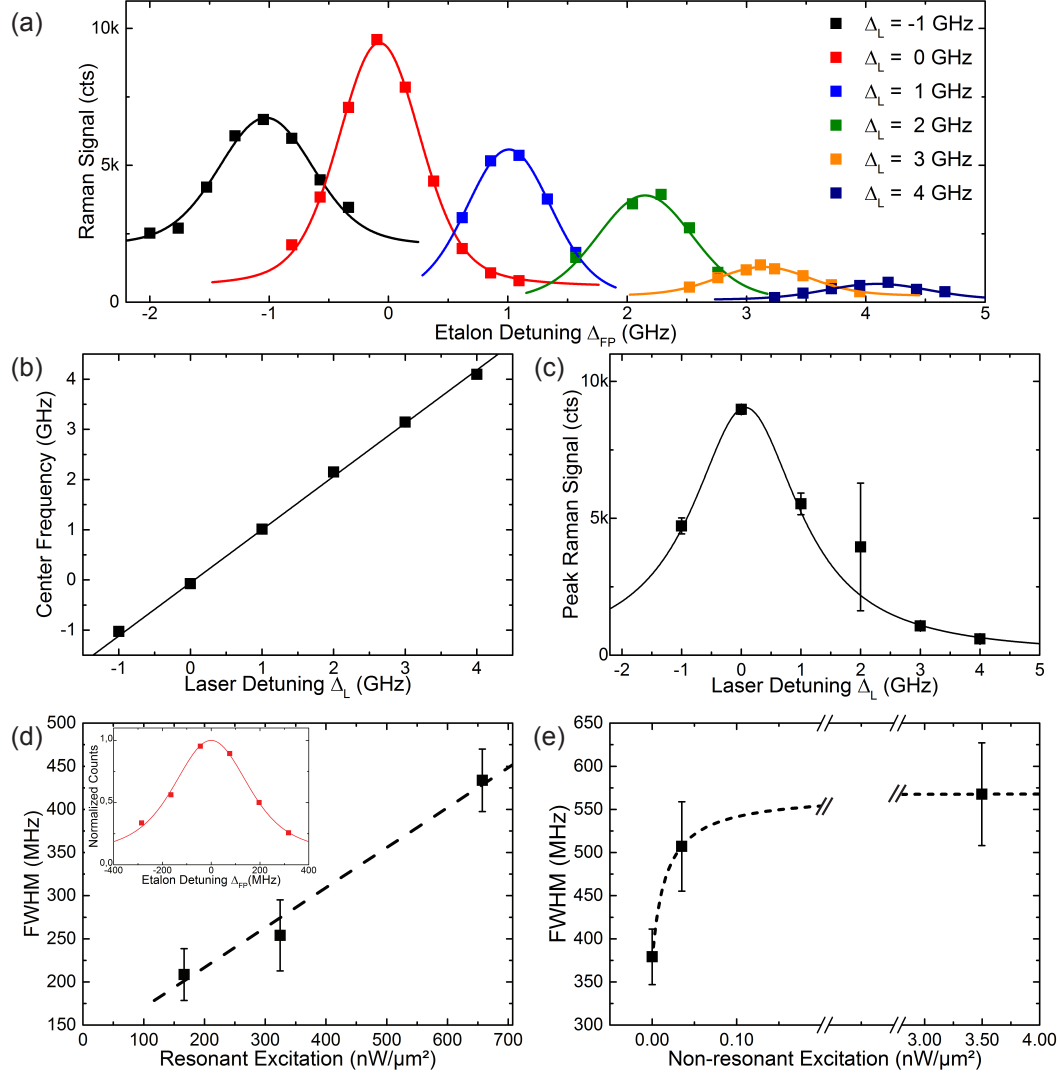


Figure 4.4: Spectral properties of the Raman photons. (a) Spectra of 50 ns gaussian single photons measured for different control laser detunings  $\Delta_L$  (2 MHz repetition rate, 100 s integration). Voigt fits (solid lines) are used to extract values and error bars for the center frequency (b), peak (c) and linewidth of the Raman light stream deconvoluted from the (lorentzian) etalon transmission profile. (d) Increase of the spectral linewidth with control pulse intensity for a fixed temporal profile with the minimum nonresonant intensity (the dashed line indicates a linear fit). Inset: Raw spectrum. A Gaussian emission linewidth (FWHM) of 200 MHz is obtained by a Voigt fit with the Lorentzian instrument response (FWHM of 250 MHz) (e) Increase of the spectral linewidth with nonresonant intensity. The saturation fit (dashed line) is a guide to the eye.

be adjusted to reach a good compromise between high single-photon generation rate and low multi-photon emission probability.

## 4.7 Spectral properties of Raman photons

Besides tunability and purity, quantum protocols based on two-photon interference require sources of single photons with a high degree of indistinguishability. By comparing the spectral linewidth and the Fourier transform of a given temporal wave packet, one can infer the degree of indistinguishability that would be measured in a Hong-Ou-Mandel interference experiment. This is a very stringent test: it compares photons generated at widely different times.

Figure 4.4(a) shows the spectra corresponding to 50 ns gaussian single photons obtained for different excitation detunings  $\Delta_L$  from the  $|\downarrow\rangle_z \rightarrow |\downarrow\uparrow\uparrow\rangle_z$  resonance. These measurements were performed with a moderate nonresonant laser intensity of  $0.15 \text{ nW}/\mu\text{m}^2$  to increase signal count rates. Each curve is fitted by a Voigt profile to extract the center frequency, amplitude and linewidth, after deconvolution from the etalon transmission profile. A free offset allows an estimation of the number of unwanted (background) counts due to photons scattered before or after the Raman flip. As expected, the center frequency of the Raman signals shifts linearly with the laser detuning  $\Delta_L$ , while its peak amplitude follows a lorentzian profile in  $\Delta_L$ , as shown in Fig. 4.4(b) and (c), respectively. However, the expected decrease of the linewidth with  $\Delta_L$  at large values is not observed; instead, it retains a value of  $\sim 700 \text{ MHz}$ .

To understand this, we studied the influence of laser intensities on the Raman photon linewidths from both the 780 nm resonant control and the 633 nm nonresonant laser. Initially, the nonresonant intensity was set to a low level ( $\sim 0.01 \text{ nW}/\mu\text{W}^2$ ) to minimize charge noise in the QD environment, and we measured the variations of the spectral linewidths as we increased the intensity of a square resonant control pulse. From the data shown in Fig. 4.4(d), the linewidth increases linearly with the intensity of the control pulse. This points to a broadening mechanism involving laser-induced mixing between long- and short-lived states. Here indeed, due to the absence of strict polarization selection rules, the off-resonant couplings of the control field between  $|\uparrow\rangle_z$  and  $|\downarrow\uparrow\uparrow\rangle_z$ , and  $|\downarrow\rangle_z$  and  $|\downarrow\uparrow\downarrow\rangle_z$  are expected to reduce the effective hole spin coherence. This effect is also responsible for the broadening of the spectrum observed in Fig. 4.4(a) when the laser comes close to resonance with the  $|\uparrow\rangle_z \rightarrow |\downarrow\uparrow\uparrow\rangle_z$  transition ① at  $\Delta_L = -1 \text{ GHz}$ . However, at the cost of reduced single-photon emission efficiency, lower excitation intensity enables the generation of Ra-

man photons with linewidths as low as 200 MHz (see Fig. 4.4(d), inset), which is about an order of magnitude narrower than the 1.1 GHz linewidth of the excited states measured in RF at low saturation.

Finally, we set the resonant square pulse to an intermediate peak intensity, and we measure the variations of the spectral linewidth with the intensity of the nonresonant laser. While the single-photon emission rate increases quickly as the QD becomes more active, we again observe a broadening of the linewidth up to about twice the initial value (Fig. 4.4(e)). We attribute this additional broadening to charge noise in the environment of the QD, which increases with the nonresonant intensity as more and more charges are optically excited in the  $\text{Al}_{0.4}\text{Ga}_{0.6}\text{As}$  matrix surrounding the QD. In our sample without charge control, fine tuning of the nonresonant power is thus required to reach a compromise between large single-photon emission rates and narrow emission linewidth.

## **4.8 Conclusion and outlook**

In summary, we have demonstrated a fast single-photon source based on an epitaxial GaAs QD that generates on-demand single Raman photons with controlled temporal profiles at the wavelength of the rubidium D2 line.

Reaching the Fourier-transform limit eventually requires to engineer the electronic and photonic QD environments. First, embedding the QDs in a pin-diode type structure would enable deterministic charge control, eliminating the need for an additional nonresonant excitation [43]. Furthermore this capacitor-like structure is known to suppress charge noise. In the case of self-assembled InGaAs QDs, this results in close-to-transform-limited optical linewidths [44, 73], and long  $T_2^*$  times for the hole spin [45]. Secondly, adding a photonic structure to enhance the collection efficiency would enable operation at lower resonant power and larger detunings. This will improve the photons' properties, and could ultimately provide deterministic spin-photon entanglement using cavity-stimulated Raman spin-flip [146].

Even with the present performance, the demonstrated properties of our source make it immediately suitable for investigating EIT-based single-photon storage and retrieval in warm rubidium vapors [29]. The ability to control the temporal profile of the photon wave packets opens the way for memory optimization using optimal control methods [13]. Such a semiconductor-atom interface will form the basis for studies on hybrid entanglement between collective atomic spin-wave excitation and single semiconductor spins, as well as between distant atomic quantum memories in a quantum network.

#### 4.8. *Conclusion and outlook*

---

## Chapter 5

# Exciton decay dynamics of a positively charged exciton $X^+$ in an epitaxial GaAs quantum dot in pulsed resonant and above-band excitation

The exciton lifetime constitutes an important metric of a quantum dot. It directly quantifies the expected maximum rate of single photon generation as well as the lower bound of single photon bandwidth as the Fourier-transform limit.

A time-resolved detection of the emitted photons from a quantum dot following pulsed laser excitation directly maps the decay of the excited state population in the recorded histogram. Under the assumption of negligible non-radiative relaxation processes, and therefore near-unity quantum efficiency, the measurement directly reveals the exciton lifetime.

Such measurements are predominantly carried out by above-band laser excitation, in which carriers are excited in the barrier material surrounding the quantum dot. These photoexcited carriers are subsequently captured by the quantum dot, where they relax to the lowest, unoccupied, discrete excited state of the quantum dot, from which single photon emission occurs [159].

The required carrier relaxation depends on an efficient interaction-mediated energy dissipation. An inelastic scattering with phonons is believed to be inefficient due to energy and momentum conservation requirements [70]. The discrete level spacings of a quantum dot

---

need to match LA- or LO-phonon energies, rendering phonon scattering unlikely. The suggested presence of a phonon bottleneck however, is not universally observed [160]. For InGaAs quantum dots it has been shown that a continuum tail, originating from the wetting layer, enables an efficient phonon-mediated relaxation process [161]. For epitaxial GaAs QDs, this coupling is inhibited due to the presence of a tunnel barrier, separating the QDs from the wetting layer. However, fast excited state population has been reported in GaAs quantum dots, which was determined to arise from Auger-type Coulomb scattering processes involving confined carriers in the quantum dot [58].

Regardless of the underlying relaxation mechanism, relaxation results in the disjunct carrier injection and hence emission time-jitter of a single photon, which is highly unfavorable for applications that rely on two-photon interference as it impedes reproducible wave-packet overlap. Furthermore, an increased level of charge-noise arises from additional laser-induced charges in the vicinity of the quantum dot, diminishing two photon coalescence further due to spectral wandering [25, 26, 162].

In order to avoid the drawbacks associated with above-band excitation, excitons can be created directly in the quantum dot by pulsed resonant excitation. Due to the identical wavelengths of quantum dot photons and reflected laser light, a clear distinction between the two requires either a cross-polarized excitation and detection scheme, as previously shown, or means of geometrical beam separation to avoid compromising signal integrity with residual laser light [86, 163]. The generation of resonant laser pulses of duration shorter than the exciton lifetime imposes further demands. Either a pulsed laser, tunable in emission wavelength, can be used, or optical laser pulses are created by optically gating the light from a tunable continuous-wave laser via an electro-optic-modulator (EOM) in conjunction with fast switching electronics.

Resonant injection of a single exciton can be regarded as equivalent to coherently driving the quantum dot two-level system from the vacuum state to the excited state, achieving the highest photon yield when the two-level system is completely inverted by a resonant “ $\pi$ -pulse” [164, 165, 166]. This geminate, resonant excitation of a bright exciton is highly coherent and stands in contrast to the above-band excitation in which charges of random spin are captured by the quantum dot. This results in an equal probability of dark- and bright state population of the neutral exciton, diminishing photon generation efficiency [167]. The elimination of an emission time-jitter and the two-fold increase in excitation fidelity can be regarded as clear advantages over above-band excitation. However, the presence of two non-degenerate neutral exciton states split by the comparably small FSS can invoke an undesired coherent coupling of the two, manifesting in an observed beat-note in the temporal emission [168]. This is an effect that arises in both resonant and above-band excitation and

adds unwanted complexity to a simple lifetime measurement. Naturally, this effect can be avoided by polarization discrimination of the excitation laser.

A straightforward alternative is to use a singly charged exciton state. The absence of dark states in conjunction with degenerate states circumvent the discussed drawbacks of single photons emitted by the neutral exciton.

## **5.1 Experimental setup and methods**

All measurements are performed in above-band ( $\lambda = 633$  nm) or resonant ( $\lambda \approx 780$  nm) excitation on epitaxial GaAs quantum dots obtained by subsequent filling of locally etched nano-holes in AlGaAs [53]. The quantum dots are not incorporated into a diode structure. Therefore, it lacks any means of deterministic charge-state control. A dark-field microscope, as shown in Fig. 5.1, is used to collect the single photons emitted by the quantum dot and enables discrimination between back-scattered laser light and resonance fluorescence signal by a cross-polarized excitation and detection scheme. Spectrally-resolved detection of the photoluminescence signal on a spectrometer equipped with a charge coupled device (CCD) constitutes a fundamental characterization of a single quantum dot. Resonance fluorescence spectra are obtained by sweeping the excitation frequency across the exciton resonance and detecting the emitted photons as a function of the laser detuning. The enhanced sensitivity of resonance fluorescence enables deeper insight into the optical properties of the investigated quantum dot.

Exciton lifetime measurement are performed by pulsed excitation with a supercontinuum laser (NKT SuperK Extreme), emitting pulses of 5 ps duration and a Gaussian spectrum of FWHM  $\approx 5$  nm with adjustable repetition rates of up to 78 MHz (see Fig. 5.1). The quantum dot signal is spectrally filtered by a diffraction grating spectrometer (FWHM = 0.1 nm), as illustrated in Fig. 5.1, to ensure exclusive transmission of light from a selected exciton transition to the two single-photon avalanche photo diode (APD, Picoquant MPD) with a timing-jitter of  $\sim 40$  ps. A time-correlated single-photon counting module (TCSPC, Picohart 300) measures the relative time delay of single photon events of one detector with respect to a trigger signal from the pulsed laser, in order to obtain a time-resolved photoluminescence / resonance fluorescence measurement. By recording relative time delays of photon events on two independent detectors in a Hanbury Brown-Twiss interferometer, a second-order correlation measurement can be obtained.

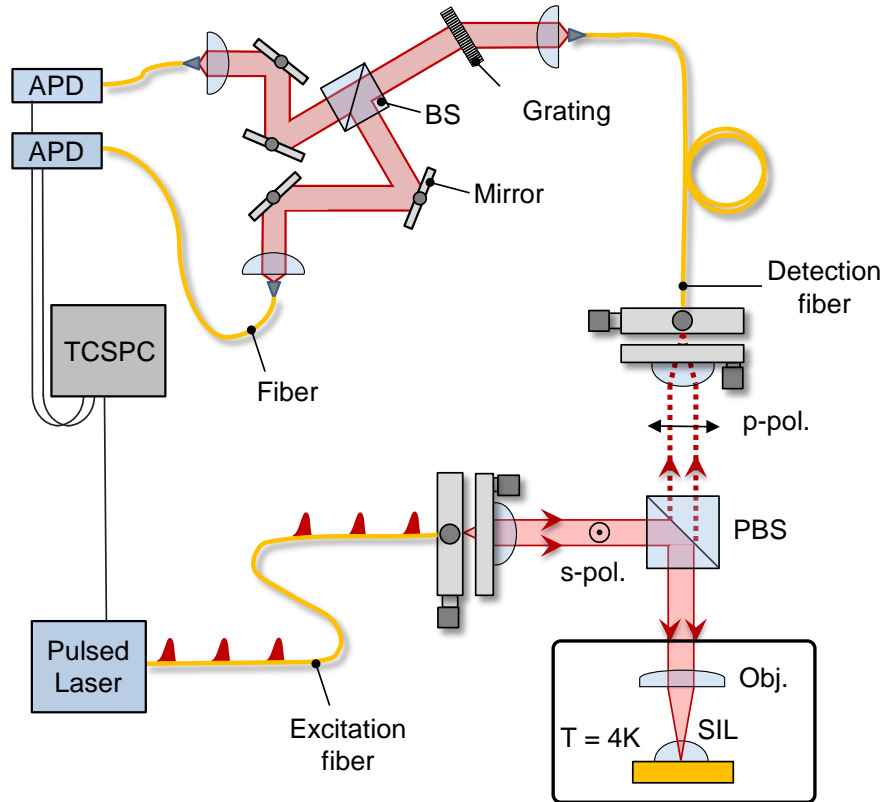


Figure 5.1: Experimental setup for time-resolved photoluminescence / resonance fluorescence measurements. A cross-polarized dark-field microscope suppresses back-reflected laser light by up to 80 dB. Additional optical filtering via a grating spectrometer ensures the exclusive detection of light from a single exciton transition on fast single-photon avalanche photo diodes (APDs). A time-correlated single-photon counting module (TCSPC) measures the relative time delay of trigger events.

## 5.2 Decay dynamics

As a first characterization, laser excitation intensity dependent photoluminescence is recorded. The spectra of the investigated quantum dot show a typical pattern of different exciton transitions, identical to the vast majority of quantum dots in this sample, allowing a definite identification of the positively charged  $X^+$  based on previous measurements (see chapter 3 and 4). A Lorentzian fit of the signal recorded on the spectrometer-CCD, shows a saturation at  $\sim 95$  kcts/s for the  $X^+$ , notably higher than the neutral exciton ( $\sim 70$  kcts/s) (see Fig. 5.2a). By changing to resonant excitation, while keeping the detection scheme



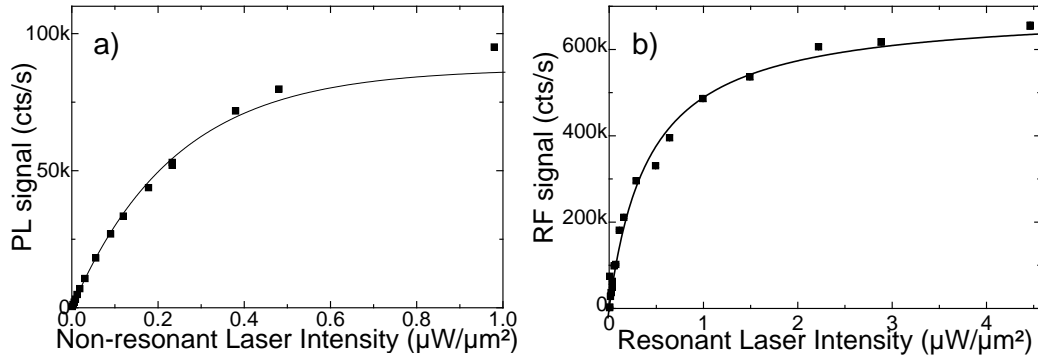


Figure 5.2: Excitation intensity dependent photoluminescence signal (a) and resonance fluorescence signal (b) of the  $X^+$  transition. An approximately six-fold increase in emission rate is observed in resonance over above-band CW-excitation.

identical, an approximately six-fold increase in emitted photons in saturation is observed, as shown in Fig. 5.2b, which can be only attributed to an increased efficiency in resonant excitation.

Concluding that a lower emission rate directly stems solely from a slow population process of the charged exciton state however, would be a misleading oversimplification. The above-band excitation induces charges in the surrounding barrier material which acts as a charge reservoir [82]. The quantum dot captures charges from this reservoir which populate its discrete energy levels. As there is no control over the number of charges captured, various charge configuration of excitons, and even (charged) multi-excitonic complexes are possible. With increasing laser intensity, the reservoir is filled with an increasing number of charges which empties by charges migrating into the quantum dot or recombination inside the barrier material. This process gives rise to a complex formation of various possible exciton configurations, interconnected by recombination processes as well as fast capture (release) processes of charges from (to) the surrounding material. A photoluminescence spectrum obtained on an ungated sample resolves the emission of various competing exciton configuration. The relative brightness of each line is the result of a complex charge filling process and charge state competition, that depends on various factors such as residual doping concentration and the efficiency of the charge capture process [169, 170].

In contrast to above-band excitation, resonance fluorescence from a charged exciton occurs by resonantly driving the corresponding exciton transition, provided the necessary additional charge occupies the quantum dot for the duration of the excitation. The additional charge is optically injected by a weak above-band laser excitation [102]. The non-resonant laser intensity is chosen such that resonance fluorescence remains the main excitation chan-

nel. Thus, the charge reservoir remains empty, effectively inhibiting the interaction of charges occupying the quantum dot with charges in the barrier material. Consequently, the charge state of the exciton stabilizes and the  $X^+$ -transition can be addressed efficiently (see section 3.11.1). In contrast, the complex charge capture process in non-resonant excitation promotes a competition between various exciton states, contributing to a reduced total photoluminescence emission from the  $X^+$  compared to resonant excitation.

In order to investigate further the exciton formation and subsequent decay dynamics, time-resolved fluorescence measurements are conducted, as depicted in Fig. 5.3a-c. In resonant excitation, the measured time-trace exhibits an instantaneous rise-time, owing to the direct exciton creation in the quantum dot, followed by a bi-exponential population decay. The determined exciton decay time of  $\tau = \frac{1}{\Gamma_{21}} = 310$  ps proves to be unaffected by excitation intensity, as expected. The existence of a second decay time can be explained by a coupling of the  $X^+$  state to other charge state configuration of the exciton via charge tunneling processes that occur on similar time-scales as the radiative exciton decay, as schematically shown in Fig. 5.3b. For the coupling rate we obtain a value of ( $\tau = \frac{1}{\Gamma_{23}} = 1600$  ps). While retaining the excitation scheme, a second-order correlation measurement is recorded, to verify that the obtained time trace stems solely from the decay of single  $X^+$ . A measured single-photon purity of  $g_{780\text{ nm}}^2(0) = 0.05 \pm 0.02$  (see Fig. 5.3d) inspires confidence in the validity of the obtained exciton lifetime. Notably, the lifetime is about three times longer than the value obtained ( $\tau = 90$  ps) in chapter 3. Beyond the strong-confinement regime in quantum dots, the oscillator strength and consequently the exciton lifetime depends strongly on the lateral extent of the quantum dot (see 1.12). Since not all quantum dots are of identical shape and size, it is conceivable that the quantum dot measured in chapter 3 exhibits a particularly large oscillator strength.

Next, time-resolved photoluminescence measurements were performed using the exact same laser and detection scheme with the only difference being the excitation wavelength of  $\lambda = 633$  nm.

In non-resonant excitation, the observed time-trace maps the exciton state population  $N_{X^+}$  and is fitted extremely well by the function

$$N_{X^+}(t) = \frac{\Gamma_{32}}{\Gamma_{32} - \Gamma_{21}} (e^{-\Gamma_{21}t} - e^{-\Gamma_{32}t}), \quad (5.1)$$

derived from a 3-level rate equation model with two transitions rates  $\Gamma_{21} = \frac{1}{\tau_{21}}$  and  $\Gamma_{32} = \frac{1}{\tau_{32}}$ , as illustrated in Fig. 5.3e,f. The measured time-trace does not allow any distinction between the two transition rates, as the rise time will always be the faster of the two rates [171]. Furthermore, since the total number of recorded photon incidences is proportional to

Chapter 5. Exciton decay dynamics of a positively charged exciton  $X^+$  in an epitaxial GaAs quantum dot in pulsed resonant and above-band excitation

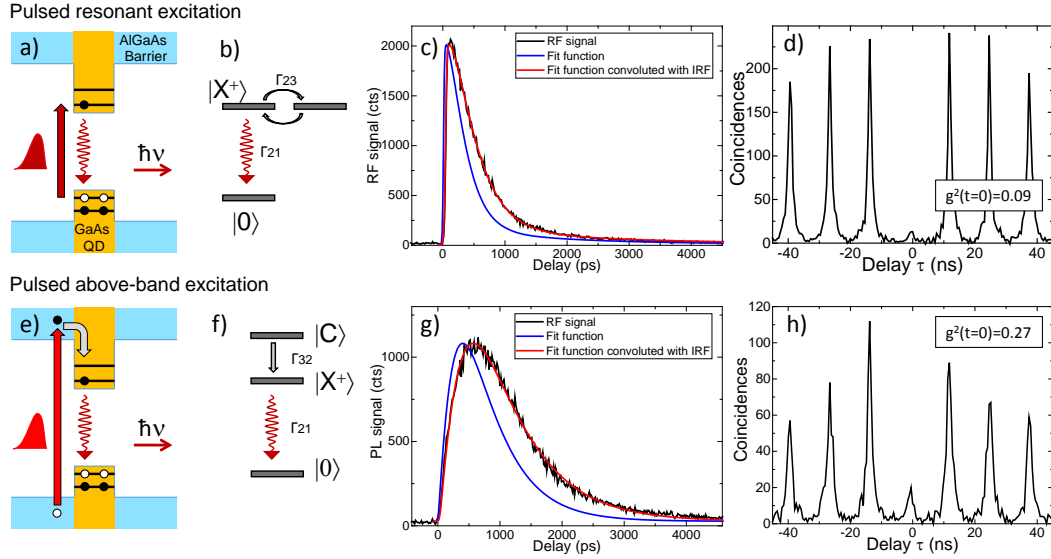


Figure 5.3: Top (bottom) row shows data obtained for resonant (above-band) excitation: a, e) Schematic of photon generation in pulsed laser excitation; b, f) Level scheme used to model the obtained results; c, g) Time-resolved quantum dot emission following pulsed excitation. In black: data points, red: fit function convoluted by the instrument response function, blue: fit function; d, h) Second-order correlation measurement. All laser intensities given are temporal averages.

$N_{X^+} \cdot \Gamma_{21}$  no distinction between the transition rates is possible based on the number of recorded photon events.

For InGaAs quantum dots the common assumption is for the fast transition rate to arise from an efficient population of the exciton level, while the slow decay mechanism stems from the population decay a single exciton [172]. Typically an accelerated exciton population with increased above-band laser intensity is observed, due to more pronounced Auger-process-mediated relaxation [58]. On the other hand, the exciton decay time constitutes an intrinsic parameter independent of excitation intensity, which is expected to be identical in resonant and non-resonant excitation. Consequently, a time-resolved photoluminescence measurement should directly map the exciton lifetime either as a decay time, or as a rise time, in case of a “slow” charge-injection mechanism. Therefore one timescale is expected to be identical to the value obtained in resonant excitation.

Remarkably, neither of the two obtained time scales proves to be similar to the values obtained in resonant excitation ( $\tau = 310$  ps). Furthermore, pulsed above-band excitation yields rise and decay times, which each show strong dependence to the non-resonant laser intensity, as shown in Fig. 5.4a. The quantum dot exhibits rise times (blue) increasing from

## 5.2. Decay dynamics

---

$\sim 60$  ps up to  $\sim 250$  ps, while the decay times (red) decrease from  $\sim 920$  ps to  $\sim 750$  ps ( $I_{\text{Laser}}^{\text{max}} = 64 \mu\text{W}/\mu\text{m}^2$ ). To verify these results, a second quantum dot was investigated, presenting nearly identical results. In resonant pulsed excitation an exciton decay time of  $\tau = 250$  ps ( $X^+$ ) is recorded. On QD2, the investigated range of non-resonant excitation intensities was higher ( $I_{\text{Laser}}^{\text{max}} = 165 \mu\text{W}/\mu\text{m}^2$ ), revealing an increase of the rise time from  $\sim 50$  ps up to  $\sim 460$  ps, while the decay time decreases from  $\sim 1030$  ps to  $\sim 660$  ps (see Fig. 5.4b). Notably, the sum of the rise and decay time appears to be more or less independent of the excitation intensity for each quantum dot.

Fig. 5.4c shows the total recorded number of photon events during each measurement on QD2. As the laser intensity is increased the total number of photon events shows a linear dependence. Only for high excitation intensities ( $>70 \mu\text{W}/\mu\text{m}^2$ ), the countrate starts to saturate.

To rule out systematic errors arising from the broad non-resonant laser spectrum, a different above-band laser diode of identical wavelength was also used, reproducing the results. Furthermore, a switch to resonant excitation with short laser pulses from a continuous-wave laser, optically-gated by a fast EOM showed no difference to the results obtained with the supercontinuum laser.

The origin of the observed discrepancy in transition rate between resonant and non-resonant excitation has been reported before in similar GaAs quantum dots [82], where the long decay times are explained to originate from a pronounced charge reservoir effect induced by a large number of states available in the AlGaAs barrier that feed excitons into the quantum dot. This hypothesis agrees well with the presented results. A second-order correlation measurement in non-resonant excitation shows a diminished single photon purity ( $g_{633 \text{ nm}}^2(0) = 0.27 \pm 0.02$ ) over resonant excitation ( $g_{780 \text{ nm}}^2(0) = 0.05 \pm 0.02$ ), depicted in Fig. 5.3d,h. When one photon has been emitted, remaining charges in the vicinity can be captured by the quantum dot and form a second exciton, resulting in the emission of two photons by a single laser pulse, which are detected as coincidence events close to delay  $t = 0$  [25].

The increase in rise times induced by an increased above-band excitation intensity (see Fig. 5.4a,b) indicates an enhanced filling and consequentially, a prolonged charge capture process by the quantum dot. Similar observations on InAs quantum dots have been reported, however attributed to an increased competition with higher exciton charge-state configurations within the quantum dot [170].

The origin of the observed decrease in decay times with increasing non-resonant laser pulse intensity is not fully understood. In the picture of an increasingly filled charge reservoir, a high laser intensity increases the availability of additional charges in the vicinity of the quantum dot. This effect might increase interaction of quantum dot excitons with these

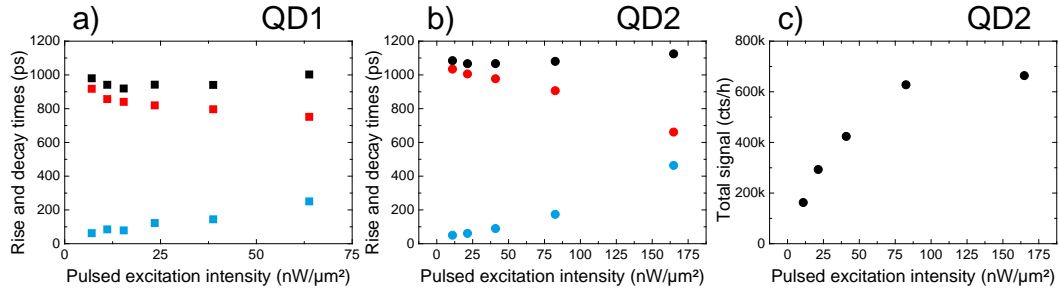


Figure 5.4: a,b) Dependence of the rise (blue) and decay (red) time in time-resolved photoluminescence measurements with respect to non-resonant excitation laser intensity for QD1 and QD2. Black: Sum of rise and decay times. c) Background-subtracted total integrated photon events of one full decay curve recorded in 1h. Data is obtained on QD2 and correspond to the measurements presented in b). All measurements are performed with 78 MHz laser repetition rate.

charges, possibly promoting exciton state competition. Capture of an additional charge before the exciton decays, alters the charge state. Such a process is not registered as a photon event at the  $X^+$  wavelength due to the accompanied change in emission frequency. This can be interpreted as an additional non-radiative decay channel, that becomes more pronounced with increasing laser intensity, since emission is more likely to occur on a different radiative transition.

### 5.3 Conclusion and Outlook

The results of exciton decay measurements in non-resonant and resonant pulsed excitation are presented. A vast difference between measured exciton decay times from a single GaAs quantum dot in time-resolved photon emission measurement is observed, depending on the excitation process. In pulsed resonant excitation a single exciton is created directly in the quantum dot. The subsequent emission exhibits a single-photon purity ( $g_{780\text{ nm}}^2(t=0) = 0.05 \pm 0.02$ ) and allows precise determination of the exciton decay time (QD1:  $\tau = 310$  ps, QD2:  $\tau = 250$  ps) independent of the excitation laser intensity. In contrast, similar measurements in pulsed above-band excitation reveal a strong dependence of the inferred time scales on the non-resonant excitation laser pulse intensity. This circumstance can be attributed to a charge reservoir effect of the large number of states available in AlGaAs. The observed effect defies the general preconception that time-resolved photoluminescence measurement allow reliable determination of the exciton lifetime, as the charge reservoir effect masks the intrinsic lifetime. This circumstance indicates the necessity of resonant excitation of the

### *5.3. Conclusion and Outlook*

---

quantum dot to obtain reliable exciton lifetimes. In the future, power dependent second-order correlation measurements will be recorded to investigate the hypothesis of the presence of a charge-reservoir, since a more pronounced timing-jitter is expected to diminish single photon purity further.

## Chapter 6

# GaAs quantum dots in a membrane

Achieving lifetime-limited emission by a quantum dot, as shown in chapter 3, requires negligible interaction with defects in the surrounding lattice that could impair the optical properties of emitted single photons. Therefore, an ideal quantum dot and its surrounding host material should feature excellent material purity, arising from the absence of unwanted “foreign” atoms or lattice defects that can dynamically interact with the quantum dot exciton, altering the emission energy. Conversely, the level of spectral wandering, which a quantum dot transition exhibits, constitutes a strong indicator for the overall quality of the material [35, 44].

Measuring photoluminescence spectra on a spectrometer equipped with a charge coupled device (CCD) gives only limited insight to the spectral properties of the emitted photons due to its finite spectral resolution ( $\sim 9$  GHz /  $\sim 37$   $\mu$ eV). The above-band laser creates charges in the quantum dot-surrounding barrier material, which relax into the quantum dot to form an exciton (as discussed in section 5). Residual, optically induced charges in the vicinity of the quantum dot shift the transition energy through the DC Stark effect, resulting in additional spectral wandering [173].

Consequently, resonance fluorescence constitutes a less invasive and more sensitive tool to investigate the optical properties of an exciton transition, owing to a reduction of spectral wandering and increased optical resolution [35]. Sweeping a tunable, resonant laser across the exciton transition and detecting the emitted photons as a function of the laser detuning directly reveals the optical linewidth [73]. A comparison of the obtained spectrum with the Fourier-transform of the exciton lifetime gives insight to the level of noise the quantum dot emission experiences. While lacking information about the exact origin of the noise, the measured spectrum acts as a good indicator for the overall material quality and suitability for its intended purpose. A broad spectrum that deviates from the Fourier-transform by or-

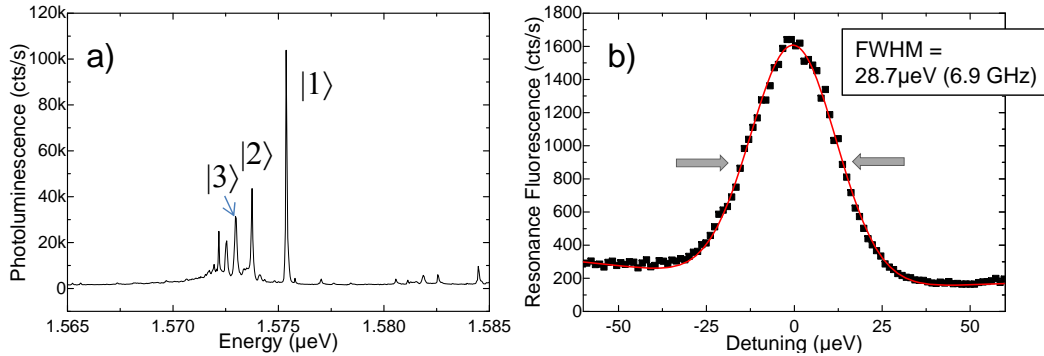


Figure 6.1: a) Photoluminescence spectrum of a GaAs quantum dot obtained by local droplet etching and subsequent filling of nanoholes in AlGaAs. The sample II-196 a<sub>4</sub> is provided by W. Hansen of the University of Hamburg. Three main transitions are investigated that can be attributed to charge state variations of the exciton. b) Resonance fluorescence spectrum of the  $|1\rangle$ -exciton with low resonant excitation power without any additional non-resonant laser light. A linewidth of  $\text{FWHM} = 28.7 \mu\text{eV}$  (6.9 GHz) is obtained by fitting with a Gaussian function.

ders of magnitude for instance, points towards an inherent unsuitability for applications that rely on two-photon-interference.

It is worth mentioning, that dedicated noise measurements based on resonance fluorescence allow an in-depth investigation of noise-frequency spectrum and to distinguish the origins of the different noise sources [73], however we refrain from conducting such measurement due to the high magnitude of noise prevalent in the examined quantum dots.

The investigated GaAs quantum dots are embedded in a 500 nm thick membrane, that was grown with the ultimate goal in mind of transferring it to a piezo-electric-crystal to gain means of emission energy tuning via tunable stress fields.

A photoluminescence spectrum of a typical quantum dot, shown in Fig. 6.1a, reveals several distinct peaks of which the highest energy transition is presumed to stem from the neutral exciton decay [62, 174]. Due to a lack of characteristic features however, will the state henceforth be referred to as  $|1\rangle$ . Aside from a number of weaker transition, which will not be investigated further, two additional main peaks  $|2\rangle$  and  $|3\rangle$  are observed, which are attributed to charged single exciton transition, since each line increases proportional to the excitation power, contrary to dependencies expected of biexciton transitions.

Fig. 6.1b shows a resonance fluorescence measurement of the  $|1\rangle$  exciton, which can be fitted in good agreement with a single Gaussian of  $\text{FWHM} = 28.7 \mu\text{eV}$  (6.9 GHz). The expected observation of two distinct peaks split by the FSS is completely masked by the broad linewidth, exceeding the expected Fourier-transform limit by about one order of magnitude.



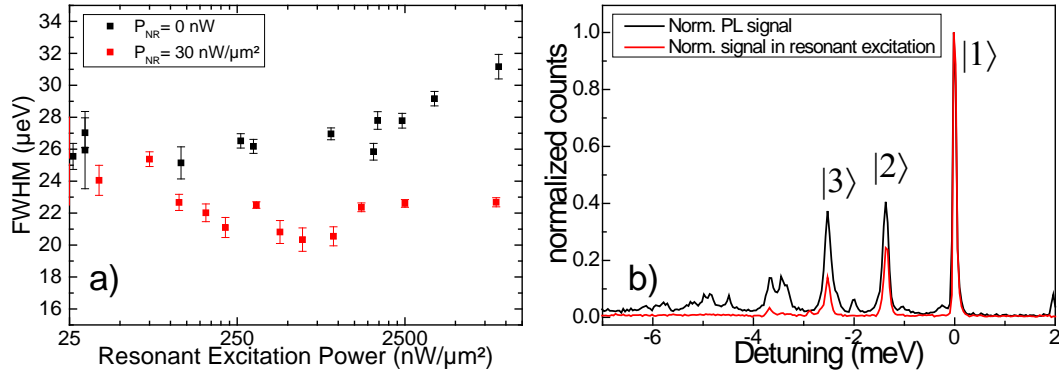


Figure 6.2: a) Gaussian linewidth obtained by resonance fluorescence of  $|1\rangle$ -exciton for different resonant excitation powers, in the presence (red) and absence (black) of non-resonant excitation. The additional  $P_{NR} = 30$  nW/μm<sup>2</sup> of above-band excitation calms the charge environment, reducing the obtained linewidth (red). b) Overlay of a normalized photoluminescence spectrum (black) with a normalized spectrum measured by resonant excitation of transition  $|1\rangle$  (red).

The discrepancy is believed to originate from a fluctuating electrostatic charge environment, prevalent despite the exclusive photoexcitation of charges directly in the quantum dot by resonant excitation [159]. Charge noise can arise from an imperfect material quality in form of residual doping or crystal defects in the vicinity of the quantum dot. Furthermore, an enhanced level of charge noise is typically associated with quantum dots close to the surface, as is the case in this membrane structure, due to an interaction with surface-bound charges [174]. The observed broadening is believed to be a result of a combination of both effects. However, their individual levels of contribution to the charge-noise remain unknown.

The observed spectral width appears to be insensitive to the resonant excitation power (see Fig. 6.2a). Even close to saturation, only negligible influence of power broadening is observed, since charge noise remains the dominant contributor. The introduction of an additional low power, above-band CW-excitation ( $\lambda = 532$  nm,  $30$  nW/μm<sup>2</sup>) calms the quantum dot environment and reduces charge noise and thus the FWHM to  $\sim 22$  μeV ( $\sim 5.3$  GHz). Despite this additional laser, resonant excitation remains the main pumping mechanism. However, the above-band laser induces additional charges in the barrier, that are presumed to saturate defect states. Such a behavior has been observed prior in InGaAs quantum dots, where it was studied in more depth [44, 102, 175].

Interestingly, fluorescence emerging from the charged excitons  $|2\rangle$  and  $|3\rangle$  is observed, while resonantly driving transition  $|1\rangle$ , as shown in Fig. 6.2b) and Fig. 6.3. The photon flux of all observed transitions scale linearly with the resonant excitation power used to excite the  $|1\rangle$  exciton, retaining the overall ratio of light contributions. The origin of this

---

cross-coupling of exciton transitions is not known. Presumably, it arises from a fast capture of an additional charge by the quantum dot, as the observed high level of charge noise suggests. This hypothesis is further supported by comparison of the ratio of emission rates from the three transitions in resonant and non-resonant excitation, as depicted in Fig. 6.2b. The ratio of light emission is largely unaffected by the resonant excitation power. Notably, it differs in pure non-resonant excitation in overall higher contributions from the charged exciton transitions. In resonant excitation of transition  $|1\rangle$ ,  $|1\rangle$ -excitons are exclusively created and emission from either  $|2\rangle$  or  $|3\rangle$  exciton requires the capture of an additional charge to occur on time scales faster than the exciton lifetime. In non-resonant excitation, all excitons are formed by a probabilistic charge capture process from the surrounding barrier material. In this process it is more likely that more than one electron and one hole migrate into the quantum dot, resulting in an enhanced probability that  $|2\rangle$ - or  $|3\rangle$ - excitons are formed. In the future, an investigation of the cross-coupling processes will entail a cross-correlation measurement of the main transition  $|1\rangle$  with either of the lower-energy charged exciton transitions. In particular the difference of resonant and non-resonant excitation is expected to give more insight into the underlying cross-coupling mechanism. However, the high-level of charge-noise proves detrimental for the use of the quantum dot as a deterministic single photon source interfaced with atomic quantum memories. Presumably, the incorporation into a charge-tunable device will inhibit unwanted charge tunneling as well as deplete residual charges - the origin of the broad emission distribution [73].

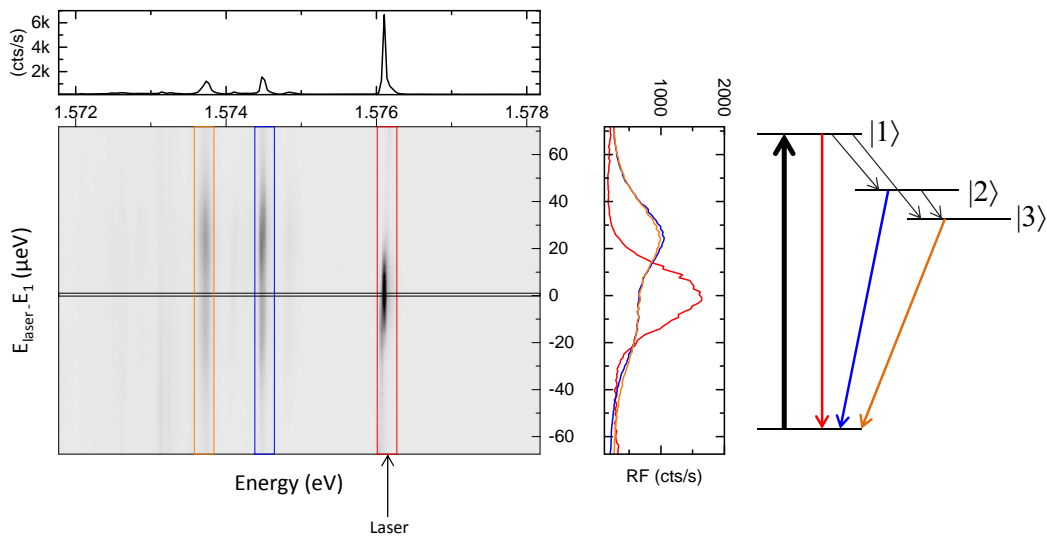


Figure 6.3: Observation of cross-translational excitation in resonance fluorescence on transition  $|1\rangle$ . a) Spectrum obtained while driving transition  $|1\rangle$  in resonance. Horizontal lines in b) indicate the specific linecut. b) Full spectrum obtained while scanning the resonant excitation laser across the transition  $|1\rangle$ . c) Aggregated spectrum of detected photons (over 7 pixels on the CCD) with respect to the excitation energy detuning from transition  $|1\rangle$ . The colored boxes in b) illustrate the aggregated events. d) Schematic level scheme of the observed quantum dot transitions.

---

## Chapter 7

# Outlook: Tuning of the quantum dot emission energy

Unlike atoms, no two quantum dot are the same. Establishing a strong interface between rubidium quantum memories and epitaxial GaAs quantum dots, however, requires frequency-matched single photon emission. As a consequence, one of the two is required to mimic the other. In light of large-scale hybrid quantum networks, it becomes obvious that all of the nodes need to operate with photons of identical frequency - the one of rubidium. Therefore a tuning knob to spectrally match each individual quantum dot to the atomic transition is required.

### 7.1 A simple low-voltage high-strain tuning device

A possible route to alter the quantum dot emission energy arises from the deliberate introduction of reversible strain. By applying stress along one of the crystal axes, the energy bands of the crystal can be manipulated. Particularly, the possibilities enabled by eliminating the FSS of the  $X^0$  motivated various approaches to strain tuning [28, 64, 65].

The previously shown method (see chapter 3) of gluing a sample piece onto a piezo-electric lead zirconic titanate (PZT) ceramic stack is derived from the work of Seidl et al. [99]. In contrast to the motivation of the original publication, which was to eliminate the FSS of an InGaAs quantum dot, our interest in this method stems solely from the tunability of the transition energies.

Despite the proven excellent long term stability, a highly desirable trait for interfacing the quantum dot with atoms, the main drawback arises from a rather limited tuning range of

### 7.1. A simple low-voltage high-strain tuning device

---

about  $\sim 30$  GHz ( $\sim 120$   $\mu\text{eV}$ ) ( $V = 0\text{-}150$  V), rendering the initial process of finding a Rb-compatible quantum dot within the ensemble challenging.

Novel strain-tunable devices rely on micromachined piezo-electric single crystal (PMN-PT), which can withstand high electric fields ( $>20\text{kV/cm}$ ) and are therefore fabricated to be on the order of hundreds of micrometer thin to reach these electric fields with still reasonable applied voltages. To achieve high strain fields at the location of the emitter, the quantum dots are embedded in membranes of few hundreds of nanometer thickness. A membrane is soft compared to the piezo-crystal ( $k_{\text{sample}} \ll k_{\text{piezo}}$ ), thus not affecting its ability to expand/contract. By selectively etching away a sacrificial layer, implemented underneath the quantum dots in the growth process, the resulting membrane, containing the quantum dots, can be lifted off and bonded onto the piezo-electric crystal [176].

While membranes offer highly tunable quantum dot energies, with ranges exceeding 100 meV in suitable devices, the inevitable proximity of the quantum dots to surface-bound charges has been shown to be a potent source of charge-noise [82]. Furthermore, the reduced spatial dimension in growth direction leaves little room for a directional photonic environment of the structure to maximize collection efficiency [35, 177].

A simple measure to increase outcoupling efficiency by a factor of  $\sim 4$  constitutes the use of a zirconia solid immersion lens, which is attached directly to the surface of the sample with vacuum grease [178]. These hemispherical lenses only enhance the collection from a “sweet spot” of about 50  $\mu\text{m}$  diameter restricting the number of usable quantum dots. To benefit from the aforementioned optical improvements, the tunability of these few quantum dots needs to be high enough that at least one quantum dot in the sweet spot can be tuned into resonance with rubidium.

The complexity involved in PMN-PT-based strain-tuning in conjunction with the limited possibilities of a tailored photonic structure motivated the development of a simple tuning device that reliably exerts high stress on the quantum dot, without the need to mechanically or chemically modify the substrate thickness. By using strong PZT-PT actuators in a mechanical device (see Fig. 7.1a), inspired by the works of Hicks et al. [179], we expect to achieve a significant increase of energy tunability over the concept of Seidl et al, without compromising on ease-of-use.

Application of a positive (negative) bias extents (contracts) two, 9 mm long PZT-PTs stacks with a  $5 \times 5$   $\text{mm}^2$  cross-section, actuating a titanium block onto which one end of the sample is firmly attached with epoxy. A reversed bias of identical amplitude, as applied to the other PZT-PTs, actuates a  $7 \times 7$   $\text{mm}^2$  PZT-PT stack, driving the opposing part of the sample holder in the opposite direction. Due to the proportionality of the cross-sectional area to the generated force by the PZT-PT, the stress exerted on the sample in each direction is identical,

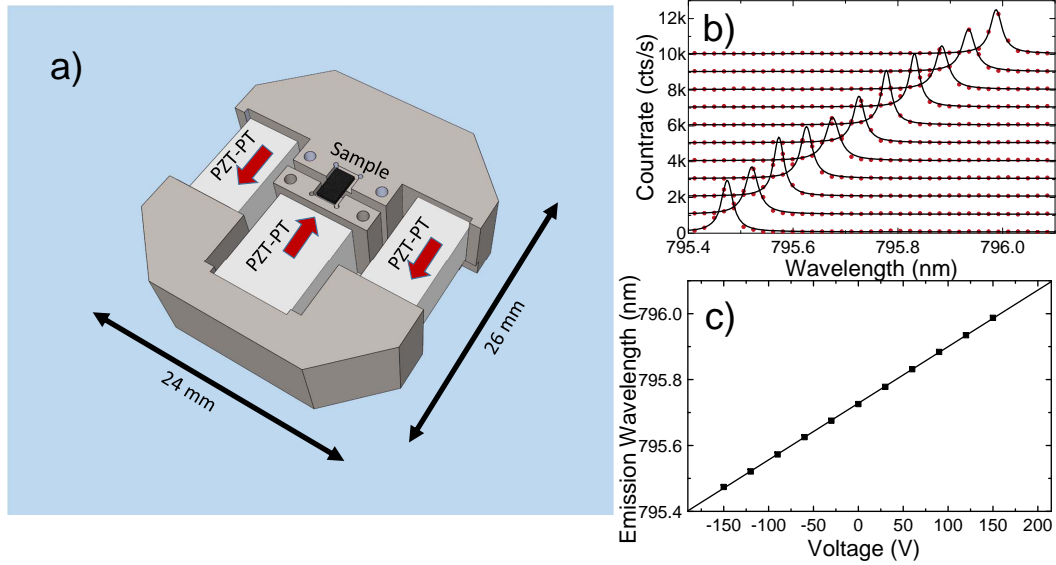


Figure 7.1: a) Schematic illustration of a PZT-PT based strain-tuning device. b) Spectrum with Lorentzian fit and c) central wavelength of the  $X^0$  transition of a GaAs quantum dot obtained by voltage dependent photoluminescence measurement.

leaving the quantum dot location unchanged regardless of the voltage applied. The symmetric arrangement of piezo-electric transducers is designed to be inherently unaffected by cooling related contraction of the piezos, minimizing undesired pre-strain to the sample. By limiting the sample length, to which strain is applied, to  $\sim 1$  mm, the total relative elongation of the three piezo-stacks is leveraged to achieve higher strain in the sample. Provided the spring constant of the sample is negligible compared to the stiffness of the piezo-stacks, the PZT-PTs reach the maximum combined total elongation (contraction) of approximately  $\pm 3.6 \mu\text{m}$  ( $T = 4$  K). This equates to a  $\sim 17$ -fold increase over the concept of Seidl et al. with a total attainable strain of  $\pm 0.4\%$  [99].

In cryogenic temperatures, the force a PZT-PT stack exerts for a given voltage is reduced to  $\sim 10\%$  of the room temperature value. On the other hand, cryogenic temperatures allow for higher voltages and bidirectional use due to an increased resistivity against depolarization, extending the operational voltages from  $-30$  to  $150$  V at  $300$  K, to  $-300$  V to  $300$  V at  $4$  K. Despite the thickness ( $500 \mu\text{m}$ ) of the GaAs substrate and the short length of  $1$  mm (width =  $2$  mm), the sample is comparably soft ( $k_{\text{sample}} \approx 90 \text{ N}/\mu\text{m}$ ) with respect to PZT-PT actuators ( $k_{\text{piezo}}^{7 \times 7 \text{ mm}^2} = 240 \text{ N}/\mu\text{m}$  &  $2 \times k_{\text{piezo}}^{5 \times 5 \text{ mm}^2} = 240 \text{ N}/\mu\text{m}$ ) and a theoretical strain of  $\pm 0.26\%$  is attainable, which equates to a  $\sim \pm 220$  MPa or a total tuning range of  $\sim 5.4$  meV ( $\sim 1.3$  THz) [99]. Extrapolation to the maximum voltage range of first results of a voltage

dependent photoluminescence measurement on a GaAs quantum dot, obtained for -150 V to 150 V operation, yields about 2.0 meV total tuning range as shown in Fig. 7.1b,c. Despite the prevalent deviation from the expected value, a  $\sim 4$ -fold increase of the energy tuning range with respect to the scheme of Seidl et al. is achieved in a cost effective and simple to use piezo-mechanical device. Presumably, the observed discrepancy stems from an imperfect strain transfer through the epoxy (estimated Young's modulus  $\approx 10$  GPa [180]), which might be remedied with additional clamping and/or mechanically polishing the sample to reduce its stiffness.

In the future, a reduction of the sample holder spacing can further improve the tunability due to an increased leverage of the piezo-stack movement, provided the aforementioned challenges are successfully addressed.

An additional interest in engineering the strain environment felt by the quantum dot arises from the effect stress has on the light-hole-heavy-hole admixture. For even comparatively modest positive tensile strain of  $\sim 0.1 - 0.4\%$ , a significant shift towards a higher light-hole component has been observed [177, 181]. The level of light-hole-heavy-hole mixing controls the transition rate of the “weakly-allowed” spin-flipping transition of a quantum dot in a magnetic field applied in growth direction (see chapter 4). An increasing light-hole component makes the diagonal transition faster, thus enables faster spin initialization via spin pumping. Control over the light-hole-heavy-hole admixture constitutes a possible tuning knob to adjust the branching ratio observed in high magnetic fields. A less asymmetric branching ratio allows for a faster initialization step as well as requiring less resonant excitation power to generate tailored single Raman photons of the same duration, promising an overall shorter two-step photon generation sequence, while mitigating unwanted coupling to the main transitions owing to the decreased laser intensity - a promising advancement to the concept shown in chapter 4.

## 7.2 Charge tuning in a GaAs QD

Using strain solely to engineer the branching ratio implies the requirement of new means to tune the emission energy of the quantum dot to match the Rb transitions. For InGaAs-QD, charge-tunable structures, utilizing the quantum confined Stark effect, have become the standard. Furthermore, there are additional benefits, such as a reduced blinking of emission and decreased charge noise, which motivate the development of a charge-tunable diode structure for GaAs quantum dots [45, 73].

It is most common to incorporate a diode in the epitaxial growth process of quantum dots by



selective regional doping. In a typical n-i-Schottky- (n-i-p-) diode, a highly n-doped region is grown, which acts as the back gate of a diode structure in which the quantum dots are embedded. The emitters themselves are incorporated into an undoped barrier region of the same material composition, physically separated by a typically 20-30 nm thick layer from the backgate, which acts as a tunnel barrier, and hundreds of nanometers from the top gate, formed by a highly p-doped region or a metallic Schottky gate electrode [5].

The dopants induce a bending of the band structure, that can be actively manipulated by applying a voltage to the electrodes. At a structure-specific negative bias, the lowest electron state of the quantum dot becomes resonant with the Fermi energy and a single electron can tunnel through the tunnel barrier into the quantum dot [5], modifying the single photon emission to arise from a negatively charged trion rather than a neutral exciton. In analogy, changing the gate voltages allows deterministic access to higher negative charge states of the exciton. Within a certain range of applied voltages, the charge state of the exciton emission is stable, suppressing spontaneous charge state fluctuations arising from probabilistic charge tunneling in and out of the quantum dot [182]. This constitutes a major benefit over ungated structures, as it eliminates the cause for unwanted blinking behavior, which is detrimental to the deterministic use as an on-demand single photon source.

Each change of quantum dot exciton charge state is accompanied by an abrupt jump in emission energy. However, within a limited voltage window, the emission energy of the transition can be precisely adjusted through the quantum confined Stark effect [5]. The electric field prevalent in the structure depletes excess charges in the vicinity of the quantum dot, reducing charge noise and thus mitigating the effects of spectral wandering [73]. Despite reports on a successful implementation [66, 183] and the apparent benefits, GaAs quantum dots are rarely embedded in charge-tunable diode structure. To some extent this can be attributed to the focus on membrane structures which would require more sophisticated tunnel-junction designs for deterministic charge tuning of a single quantum dot due to the size constraints [184]. On the other hand, Si-doping of the quantum dot-surrounding AlGaAs-barrier material leads to the formation of DX-centers, deep donor levels that can be ionized upon illumination, inducing fluctuations of the effective potential at the quantum dot location [185].

To eliminate the detrimental effects of DX-centers, we propose to place the Si-doping ( $n = 3 \cdot 10^{18} \text{cm}^{-3}$ ) from AlGaAs into a  $\sim 6$  nm thick GaAs quantum well (QW), which substitutes the bulk back gate. The discrete energy levels associated with a 1D confinement structure elevate the Fermi energy to reside within the conduction band of the GaAs-QW. An illustration of the proposed structure is shown in Fig. 7.2a. Fig. 7.2b shows the calculated band structure obtained by Poisson-Schrödinger simulation. A simplified view which

## 7.2. Charge tuning in a GaAs QD

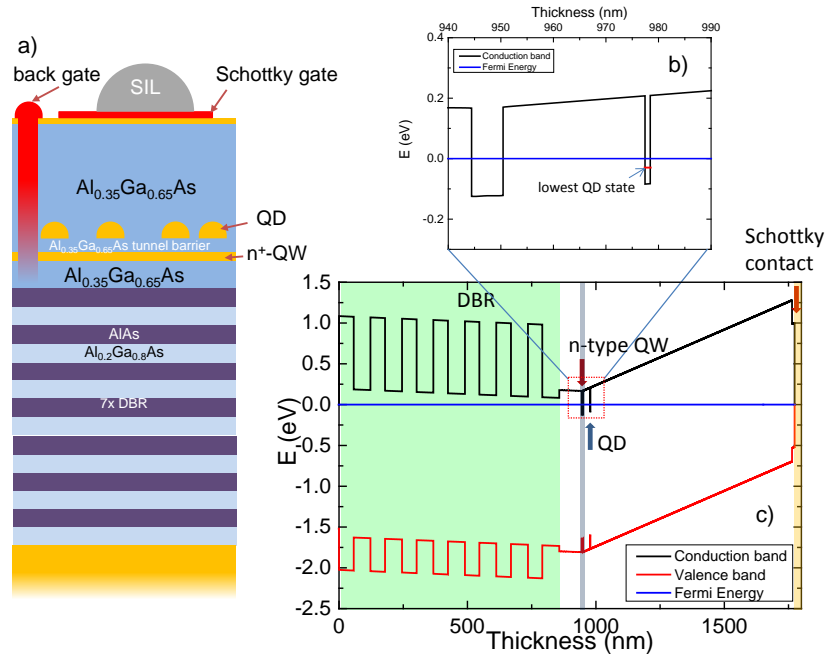


Figure 7.2: a) Schematic illustration of the proposed p-i-Schottky diode that permits deterministic charge-tuning of epitaxial GaAs quantum dots. The high doping concentration of the back contact is allocated into a GaAs-QW in order to avoid creation of DX-centers commonly observed in Si-doped AlGaAs. b,c) Calculated band structure of the structure depicted in a)

disregards hole confinement potential, allows an estimation of the lowest QD energy level at approximately 69 meV above the bottom of the conduction band. Based on the obtained energy, a quantum well thickness and doping concentration is chosen. The Fermi-energy is determined to be 83 meV above the bottom of the QD conduction band for the proposed structure, high enough for the lowest energy level of the quantum dot conduction band to be below the Fermi energy even without application of a voltage. This allows resonant tunneling of single charges from the QW into the quantum dots, circumventing a doping of AlGaAs. The detailed proposed layout and a corresponding calculation of the optical mode, can be found in the appendix to this chapter. Notably, the QW thickness and doping concentration is chosen to allow operation at frequencies of either of the rubidium D-lines. In turn, the discrete electron levels allow for a QW emission and photon absorption at lower wavelength than bulk GaAs, in the presented case  $\lambda \approx 750$  nm, an important trait to avoid interference with the optical properties of the quantum dot photons.

The electrical contact to the QW is achieved by deposition of Au/Ge alloy contacts onto the

surface, that diffuse to the QW in a subsequent annealing process, establishing a direct electrical connection to the back gate from the surface. The top gate forms a semi-transparent 10 nm Ti/Au alloy Schottky gate subsequently evaporated onto the surface by electron beam sputtering.

The proposed structure only considers deterministic charging of electrons into the quantum dot. However, it can be beneficial to gain access to positively charged excitons, which can be accomplished by bringing the quantum dots close to a p-doped region. Such a p-i-n diode however, differs from the earlier proposed n-i-Schottky structure in some key features to adapt to the specific characteristics of holes. The higher effective mass results in a decreased tunnel probability, which has to be accounted for by an adjustment of the tunnel barrier that separates the quantum dots from the  $p^+$ -doped region. Since  $p^+$ -doping in AlGaAs does not entail the formation of DX-centers,  $p^+$ -doped GaAs-QWs are not required. However, the incorporation of C-atoms as a p-dopant has the tendency of introducing structural irregularities, which will be passed on to subsequently grown layers, negatively affecting the optical properties. Consequently, it is beneficial to reverse the structural layout and bring the  $p^+$ -doped region close to the surface, while a  $n^+$ -doped GaAs-QW, acting as the backcontact, is buried deeper in the structure [45].

Pristine optical properties, i.e. reduced charge-noise and blinking effects, paired with superior energy tuning capabilities constitute the main motivation for the development of a charge-tunable diode structure for quantum dots. Ultimately, the structure needs to incorporate additional measures to ensure a highly directional emission in order to maximize outcoupling efficiency. A first step is already incorporated in the proposed design in form of a highly reflective Bragg mirror below the quantum dots in order to reflect photons emitted in the “wrong” direction. It is conceivable to include an additional opposing Bragg mirror to form a cavity and achieve preferential emission into said mode. In the following, a brief outlook into the development of photonic quantum structure, optimized for outcoupling efficiency will be given.



## Chapter 8

# Outlook: Enhancing the outcoupling efficiency of quantum dot photons

The term “on-demand photon” implies delivery of exactly one single photon at a desired location upon a trigger signal. In light of the aspired implementation of the presented hybrid quantum communication protocol, the importance of a near-perfect photon extraction efficiency becomes evident. It can be shown from Eq. 1.7, that the total time for successful entanglement distribution involving  $n$  nodes, scales with  $p_1^{-(n+3)}$ , in which  $p_1$  denotes the probability of single photon emission per trigger pulse [24]. An additional constraint arises from the noise level in the quantum memory. The storage and retrieval of a single photon of greater than unity signal-to-noise ratio, assumes  $>0.27$  photons per signal pulse (see chapter 2.2).

A common approach to enhance photon extraction efficiency stems from the incorporation of a quantum dot into an optical cavity. The enhancement of the photonic density of states, i.e. optical modes, available to a dipole transition, yields a preferential emission into these modes. By embedding the emitter in a microcavity, a highly directional emission is achieved, owing to a pronounced cavity mode, by an increase in the spontaneous decay rate through the Purcell enhancement,  $F_P$ . In this framework, a measure for the directionality of emission constitutes the mode coupling efficiency  $\beta$ , given for cavity structures by [186]

$$\beta = \frac{F_P}{1 + F_P}. \quad (8.1)$$

While a large  $\beta$  is an essential prerequisite for a high photon extraction efficiency, the associated Purcell enhancement increases the Fourier-transform limit bandwidth of spontaneously emitted photons proportionally. Direct storage of such photons in the quantum memory be-

---

comes increasingly inefficient due to the more pronounced bandwidth mismatch. However, the previously shown generation of Raman photons is not constricted by the Fourier-limit, rendering the effect irrelevant for the establishment of an efficient hybrid interface.

Various realizations of semiconductor microcavities, such as photonic-crystal cavities [187], micropillar cavities [6, 7, 26], circular Bragg grating bullseye cavities [188] and fully tunable plano-concave microcavities [189] exhibit excellent photonic properties. Notably, alternatives to a cavity have emerged, devices which rely on inhibiting undesired optical modes opposed to enhancing preferential modes. Harnessing the intrinsic wave-guiding properties of nanowires and photonic trumpets, for instance, allowed extraction efficiencies of single photons, emitted by an incorporated InAs quantum dot, up to 75% [8, 27]. Furthermore, microlenses defined in-situ by three-dimensional electron-beam lithography presented extraction efficiencies of 23% [168, 190].

Retaining a sufficiently tunable, low linewidth emission from the quantum dot is highly desirable. In this regard, microcavities have proven to be an excellent choice. The following will therefore briefly outline what an adaptation for epitaxial GaAs quantum dots entails.

The incorporation of suitable dielectric Bragg reflectors (DBR), positioned underneath and above the quantum dot region, allows the formation of a planar microcavity in the growth process. The shorter emission wavelength of GaAs quantum dots, compared to common InGaAs quantum dots, necessitates a change in the composition of the constituent layers, from GaAs to  $\text{Al}_{0.2}\text{Ga}_{0.8}\text{As}$  to avoid band gap related absorption losses in the DBR. The quantum dots are positioned in the center of the cavity antinode to ensure maximized coupling to the optical mode.

Owing to an inherent optical instability of such planar microcavities, measures to ensure lateral mode confinement are required [191]. Commonly, micropillars of a few  $\mu\text{m}$  diameter, which act as a waveguide by total internal reflection at the lateral interfaces, are defined into the epitaxial structure by reactive ion etching, ideally containing a single quantum dot in the center. Probabilistic definition of micropillars without knowledge of quantum dot positions yields a low success rate of obtaining an optimal single photon device. Therefore, a position-resolved characterization preceding the etch process is required [6]. As etched structures have large height-to-diameter aspect ratio, strain-tunability is expected to be inhibited. However, despite the  $\mu\text{m}$  diameter, intricate, electrical contacts to the micropillar enable deterministic charging and emission energy tuning in p-i-n diode structures, an important knob to match quantum dot- and cavity resonance [6]. However, rough side-walls of the micropillars, larger doped areas and the possibility of enhanced oxidization due to the enlarged surface area, introduce losses.

Circumvention of the discussed drawbacks comes in a fully tunable plano-concave air gap

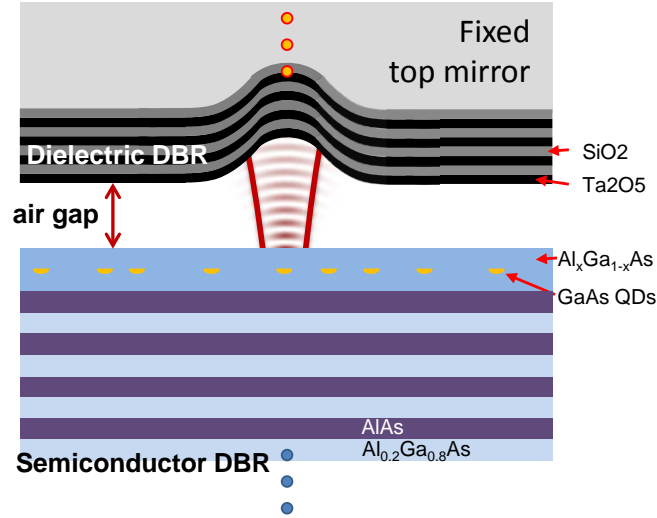


Figure 8.1: Schematic of a tunable microcavity comprised of a concave dielectric top mirror and a planar, epitaxially grown structure containing GaAs quantum dots on top of a highly reflective DBR. Three-axis nanopositioners enable arbitrary selection of a quantum dot, brought into resonance through in-situ adaptation of the cavity length by a second set of nanopositioners [192, 193].

microcavity structure, shown in Fig. 8.1 [189]. The Fabry-Pérot cavity consists of a concave top mirror and a planar epitaxially grown structure, containing the GaAs quantum dot layer on top of a highly reflective semiconductor back mirror. Both constituents are movable with respect to each other via three-axis nanopositioners, thus allowing tuning of the cavity resonance, while the additional three-axis nanopositioners enable positioning of the entire cavity in relation to a fixed collection lens [42]. As a consequence, any quantum dot out of the ensemble can be chosen through lateral positioning and brought into resonance with the cavity. Stable cavity operation is ensured by a curvature in the top mirror [191]. The underlying depressions obtained by laser ablation of silica substrates are subsequently coated with alternating layers of  $\text{Ta}_2\text{O}_5$  and  $\text{SiO}_2$  to form a dielectric Bragg mirror [194]. Unbalanced reflectivities of both mirrors ( $R_{\text{top}} < R_{\text{bottom}}$ ) facilitate a preferential outcoupling out the top, ideal for maximized single photon collection efficiency.

Advantageous to this approach, the epitaxially grown planar quantum dot structure requires no post-growth processing aside from evaporation of electrical contacts. Therefore it retains the versatility of charge- and strain-tunability, while benefiting from an efficient coupling to a Fabry-Pérot cavity, that evidently can extend well into the strong-coupling regime and therefore beyond the sought after preferential emission [193]. It is worth mentioning, that

---

the previously presented n-i-Schottky diode structure needs to be adapted to a n-i-p structure, due to light absorption on the Schottky contact.

Assuming typical parameters, a comparatively small Q-factor of 10 000, readily attainable in the shown tunable microcavity, yields a Purcell enhancement of  $F_P \approx 4$ , which equates to  $\beta \approx 0.8$ . Ultimately, the total extraction efficiency hinges on coupling losses ( $\eta_{\text{coupling}} \approx 0.7$ ) to the optical fiber, as well as polarization-filtering related losses introduced by the cross-polarized dark-field microscope ( $\eta_{\text{pol}} \approx 0.5$ ). Provided a perfectly suppressed blinking in quantum dot emission, as associated with a diode structure, the expected total quantum dot photon extraction efficiency enables photon storage and retrieval of unity signal-to-noise in the previously presented Rb vapor quantum memory.

The current quantum memory does not exploit its full potential yet and strong enhancements in signal-to-noise as well as end-to-end efficiency can be achieved with comparably little effort. On the other side of the hybrid interface, the proposed improvements to the quantum dot structure drastically increase the number of Rb-compatible emitters in the quantum dot ensemble, as well as enhancing collection efficiency of the emitted photons. Exploitation of a Raman transition for single photon generation, as shown in chapter 4, potentially alleviates the need for the current cross-polarized excitation and detection scheme, due to the possible spectral distinction between excitation laser and Raman photon emission. In this framework, a sophisticated scheme that exploits the directionality of the cavity is conceivable [195, 196]. Another benefit of the tunable cavity arises from the independent tuning of the radiative from the non-radiative transition rate, opening up means to investigate the quantum efficiency of the quantum dot transition [197].

Implementation of all the proposed improvements, eventually allows deterministic storage-and-retrieval of single photons from a quantum dot in a Rb vapor quantum memory, with negligible noise.



## Chapter 9

# Conclusion and Outlook

The enhancement of everyday applications by exploitation of quantum mechanics requires overcoming a variety of obstacles. While an envisioned quantum application might be implementable in broadly different systems, each realization faces challenges specific to the system. Rather than trying to mitigate the consequences of inferior traits, one can take advantage of the superior ones of other systems, to get the best of both worlds.

In this thesis, a hybrid approach to quantum communication is presented. By combining the excellent storage time and efficiency of alkali atomic quantum memories with the robustness and exceptional single photon emission of epitaxial GaAs quantum dots, an exponential speed-up in quantum communication over the established, non-composite DLCZ protocol, can be achieved.

Solutions to new challenges are presented, which arise en route to establish an efficient link between the two systems. The excellent material quality of state-of-the-art GaAs quantum dots enables Fourier-transform-limited emission, a prerequisite for quantum applications that rely on perfect two-photon-interference. A single-photon bandwidth of 1.42 GHz stems from a high oscillator strength and therefore fast emission, inherent to these specific types of quantum dots. While usually regarded as a strong-suit of quantum dots, the consequential bandwidth mismatch with the atomic transition necessitated a reduction of single-photon bandwidth below the Fourier-transform limit. By adapting established techniques of ion-physics to the specific demands of quantum dots, we achieved the generation of single Raman photons with tailored temporal waveform from a GaAs-quantum dot with unity efficiency, exceeding the exciton lifetime by up to 3 orders of magnitude. The generated single photons exhibit a bandwidth as low as 200 MHz, well below the limitation imposed by the exciton lifetime. Furthermore, the scheme enables the possibility of optimizing single-photon wavepackets specifically for an efficient interface with the broad-band

---

EIT-based atomic quantum memory that was developed in parallel.

As outlined, future development will focus on engineering the band-structure properties by adjustable uniaxial strain in conjunction with the development of a charge-tunable GaAs quantum dot. Specifically, the target is a single photon source optimized for fast, Fourier-transform-limited Raman photon generation. The elimination of detrimental blinking behavior expected to accompany the implementation into an electrically gated diode structure with a tunnel-junction, further increases the overall efficiency of on-demand photon generation - an important parameter for future applications. Since benefits of a hybrid communication protocols over established alternatives require near-unity collection efficiency, a strong focus will be on an optimized photonic environment of the quantum dot. In the short term, the enhanced tunability associated with an electrically gated structure enables the use of solid immersion lenses, by drastically increasing the availability of Rb-compatible quantum dots. Further advancement necessitates the incorporation into a photonic resonator in an optimized photonic structure such as a fully tunable cavity to maximize collection efficiency through a highly directional emission.

Uniting all these advancements into a single structure facilitates the generation of highly-tunable, single photons of arbitrary temporal shape exceeding hundreds of ns with near-unity collection efficiency - an exceptionally versatile yet robust single photon source, ideal to bring quantum communication to the next level.

# Appendix to chapter 5:

## The experimental Setup

Generating tailored single photons requires two tunable single-mode external cavity diode lasers (ECL), which can be tuned into resonance with the desired quantum dot transitions. By means of piezo-actuated fine control of the emission frequency, the Toptica DL Pro 780 is remotely adjustable with femtometer precision and a mode-hop free range of approximately 40 GHz. The second ECL's frequency is coarsely changed by mechanically adjusting the Littrow grating position of the external cavity and fine tuned by changing the current of the laser diode. Due to the lack of a piezo-actuator the wavelength of this laser needs to be fixed during the course of an experiment.

The fibered EOMs (Jenoptik) exhibit a 10-90% reaction time of  $\approx 200$  ps. Prior to coupling the laser light into the polarization maintaining fibers of the EOM, the linear polarization of the laser is rotated by a  $\lambda/2$ -plate in order to maximize the efficiency of the EOM. The EOM's underlying Mach-Zehnder interferometer utilizes a Pockels cell, which changes the relative path length and thus induces a phase shift, effectively switching between outcoupling of the light or discarding it internally.

By applying a DC voltage to the EOM, the induced phase shift is adjusted to ensure minimized light transmission, which is monitored with an external fast photodiode.

Since Mach-Zehnder interferometers are strongly susceptible to thermally induced path length variation, each EOM is clamped on a breadboard to ensure sufficient temperature stability. The in-coupled laser power remains constant in order to further minimize drifts in the DC voltage offset required for minimal transmission.

Fast switching of the optical signal is achieved by a short voltage pulse, provided by a 12 GHz arbitrary waveform generator (Tektronik 7122C), which is added to the DC voltage employing high-speed bias-tee (Mini-Circuit ZX85-12G-S+).

At high operation frequencies (pulse length shorter than 1 ns), the AWG fails to reach its maximum voltage amplitude of 1 V, providing only  $\approx 0.6$  V. In order to ensure that full

---

EOM transmission is reached during a pulse, a fast voltage amplifier is required to ensure the pulse amplitude reaches the EOM-specific peak-to-peak voltage of 1.2 V. The 10 GHz bandwidth of the amplifier (Photline DR-PL-10-MO) ensures that additional electrical pulse broadening remains negligible.

After the EOM, the laser excitation power is controlled by changing the transmission ratio through a polarizing beam splitter (PBS) by rotating the polarization. Subsequently, a second  $\lambda/2$ -plate ensures the polarization matches the dark-field microscope's polarizer. After the signal is outcoupled from the output fiber of the darkfield microscope, the signal analysis entails a highly flexible, free-space Hanbury Brown-Twiss interferometer in conjunction with an analyzing Fabry-Pérot cavity which is optimized for minimal photon losses. Rotation of the polarization in conjunction with a polarizing beam splitter is used as a building block to control the route of the light beam. The initial optical switch allows the Fabry-Pérot cavity to be bypassed when it is not needed. When the polarization is set for maximum transmission through the first PBS, the beam propagates through a scanning Fabry-Pérot etalon for spectral analysis. Prior to the Fabry-Pérot-etalon, a first coarse spectral filtering with a notch filter (bandwidth  $\approx 0.5$  nm) ensures blocking of any bulk material related emission. The beam is focussed into the etalon by a lens of 30cm focal length, which is chosen to match the cavity mode. Since the lens position is fixed the Fabry-Pérot etalon is mounted on a biaxial translational stage as well as a biaxial tilt stage to optimize transmission ( $T \approx 80\%$ ). The temperature stabilized Fabry-Pérot etalon has a free-spectral-range of 12.9 GHz and a Lorentzian transmission of 250 MHz FWHM.

After recombining the two possible photon paths on another PBS, the emission spectrum is filtered to block any residual above-band excitation and bulk emission using optical long-pass- and adjustable notch-filters, respectively.

By rotating a  $\lambda/2$ -plate, the photon flux can subsequently be fully transmitted to a single APD (Picoquant  $\tau$ -SPAD 20) or split equally between two APDs in a Hanbury Brown-Twiss-type interferometer. Due to residual photons being detected by the APDs in the initialization step of the two-step photon generation process, the electrical trigger pulses given by the APD during this time interval need to be discarded, so that only Raman photon related events are recorded by the TSPC. The NIM trigger signal of the APD is connected to a fast electrical switch (Mini-Circuit ZASWA-2-50DR+), which is controlled by the AWG, defining time windows in which the APD trigger pulses are transmitted to the photon counting electronics.

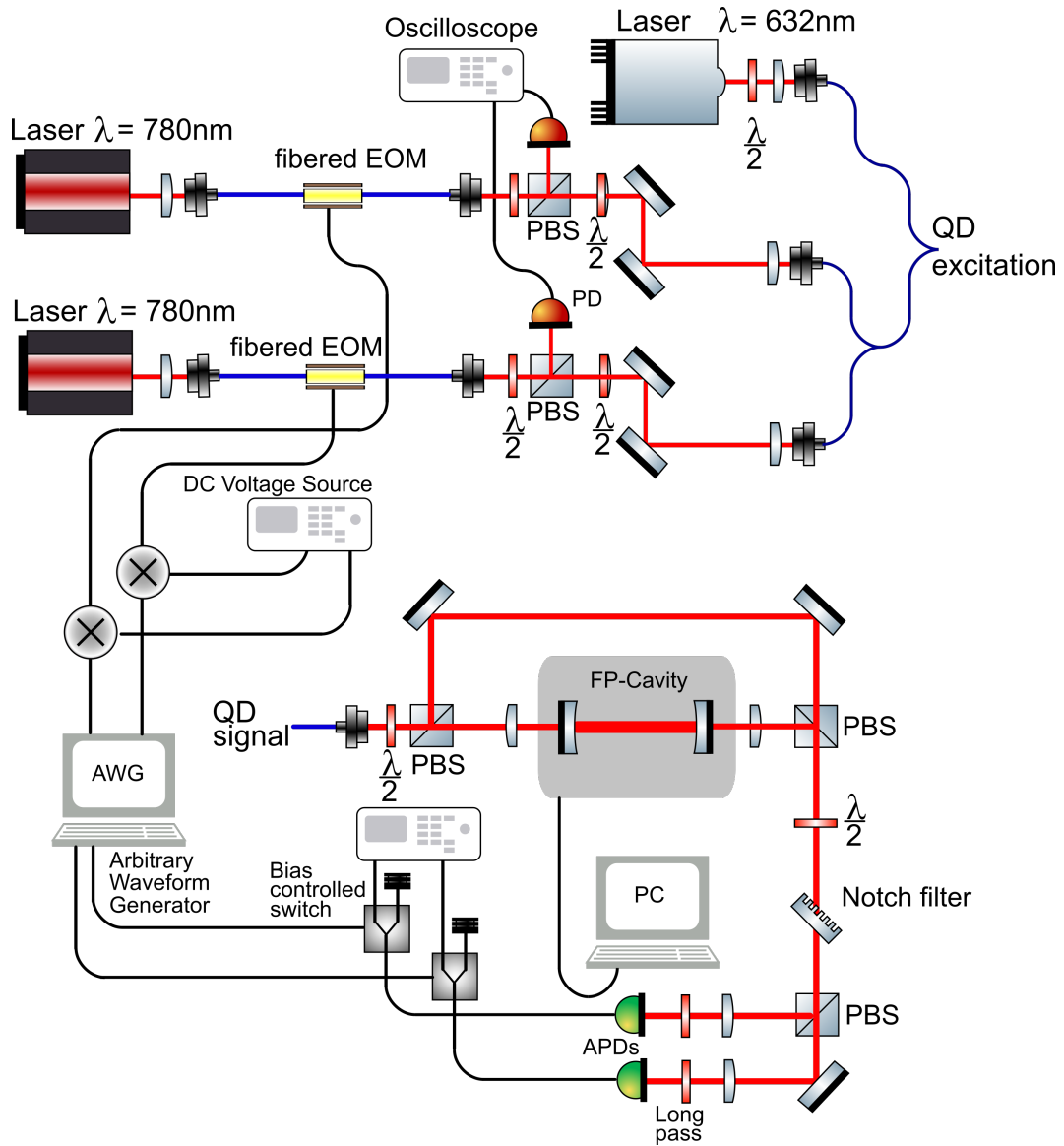


Figure 9.1: Detailed experimental setup for generating and analyzing tailored single QD photons.

---

## Appendix to chapter 7.2: n-i-Schottky diode

The simulated band structure displayed in Fig.7.2 is derived from the following proposed sample layout:

	GaAs	wafer material
7x58 nm	$\text{Al}_{0.2}\text{Ga}_{0.8}\text{As}$	7 pairs of Bragg mirrors for $R = 88\%$
7x67 nm	AlAs	
89 nm	$\text{Al}_{0.35}\text{Ga}_{0.65}\text{As}$	Buffer to place QD in mode maximum
6 nm	$\text{GaAs} (n^+ = 3 \cdot 10^{18} \text{cm}^{-3})$	n-doped QW
27 nm	$\text{Al}_{0.35}\text{Ga}_{0.65}\text{As}$	tunnel barrier
	GaAs QD	emission at $\lambda \approx 795 \text{ nm}$
785.1nm	$\text{Al}_{0.35}\text{Ga}_{0.65}\text{As}$	lever arm
10 nm	GaAs	capping layer

Table 9.1: Proposed n-i-Schottky diode structure for GaAs QDs

Simulated optical mode obtained by transfer-matrix calculation:

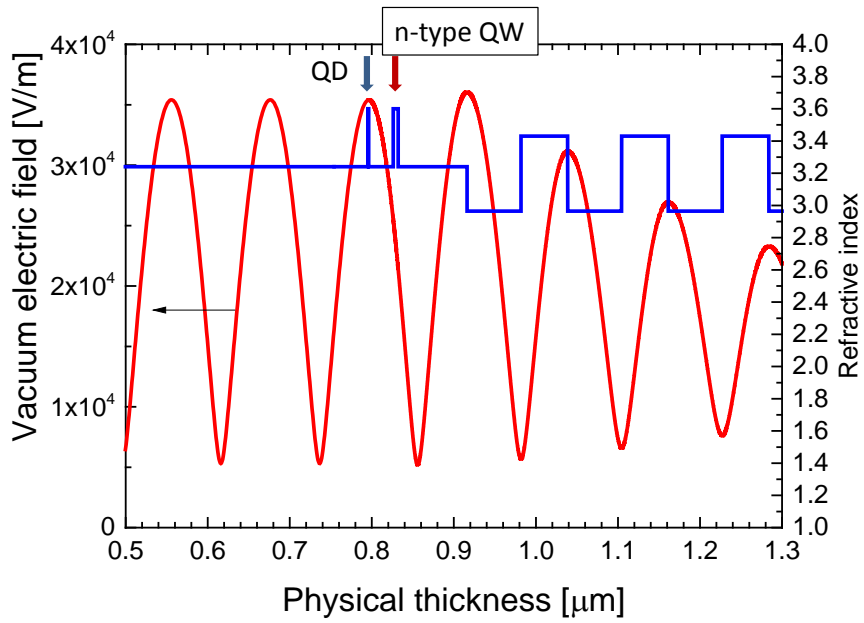


Figure 9.2: Simulated mode distribution for a quantum dot emitting at 795nm (red), refractive index of each layer displayed in blue.



# Bibliography

- [1] L. M. Duan, M. D. Lukin, J. I. Cirac, and P. Zoller, *Nature* **414**, 413 (2001).
- [2] A. J. Shields, *Nature Photonics* **1**, 215 (2007).
- [3] P. Michler, A. Kiraz, C. Becher, W. V. Schoenfeld, P. M. Petroff, L. Zhang, E. Hu, and A. Imamoglu, *Science (New York, N.Y.)* **290**, 2282 (2000).
- [4] C. Santori, D. Fattal, J. Vuckovic, G. S. Solomon, and Y. Yamamoto, *Nature* **419**, 594 (2002).
- [5] R. J. Warburton, C. Schäfflein, D. Haft, F. Bickel, A. Lorke, K. Karrai, J. M. Garcia, W. Schoenfeld, and P. M. Petroff, *Nature* **405**, 926 (2000).
- [6] N. Somaschi, V. Giesz, L. De Santis, J. C. Loredo, M. P. Almeida, G. Hornecker, S. L. Portalupi, T. Grange, C. Antón, J. Demory, C. Gómez, I. Sagnes, N. D. Lanzillotti-Kimura, A. Lemâitre, A. Auffeves, A. G. White, L. Lanco, and P. Senellart, *Nature Photonics* **10**, 340 (2016).
- [7] Y. M. He, Y. He, Y. J. Wei, D. Wu, M. Atatüre, C. Schneider, S. Höfling, M. Kamp, C. Y. Lu, and J. W. Pan, *Nature Nanotechnology* **8**, 213 (2013).
- [8] M. Munsch, N. S. Malik, E. Dupuy, A. Delga, J. Bleuse, J. M. Gérard, J. Claudon, N. Gregersen, and J. Mørk, *Physical Review Letters* **110**, 177402 (2013).
- [9] Z. S. Yuan, Y. A. Chen, B. Zhao, S. Chen, J. Schmiedmayer, and J. W. Pan, *Nature* **454**, 1098 (2008).
- [10] N. Sangouard, C. Simon, H. de Riedmatten, and N. Gisin, *Reviews of Modern Physics* **83**, 33 (2011).
- [11] X.-H. Bao, A. Reingruber, P. Dietrich, J. Rui, A. Duck, T. Strassel, L. Li, N.-L. Liu, B. Zhao, and J.-W. Pan, *Nature Physics* **8**, 517 (2012).

- [12] K. De Greve, L. Yu, P. L. McMahon, J. S. Pelc, C. M. Natarajan, N. Y. Kim, E. Abe, S. Maier, C. Schneider, M. Kamp, S. Höfling, R. H. Hadfield, A. Forchel, M. M. Fejer, and Y. Yamamoto, *Nature* **491**, 421 (2012).
- [13] M. T. Rakher, R. J. Warburton, and P. Treutlein, *Physical Review A* **88**, 53834 (2013).
- [14] C. Matthiesen, M. Geller, C. H. H. Schulte, C. Le Gall, J. Hansom, Z. Li, M. Hugues, E. Clarke, and M. Atatüre, *Nature Communications* **4**, 1600 (2013).
- [15] G. Brassard and A. A. Méthot, *Foundations of Physics* **40**, 463 (2010).
- [16] R. Horodecki, P. Horodecki, M. Horodecki, and K. Horodecki, *Reviews of Modern Physics* **81**, 865 (2009).
- [17] J. S. Bell and Others, *Physics (Long Island City, NY)* **1**, 195 (1964).
- [18] A. Aspect, P. Grangier, and G. Roger, *Physical Review Letters* **47**, 460 (1981).
- [19] A. K. Ekert, *Physical Review Letters* **67**, 661 (1991).
- [20] C. H. Bennett, G. Brassard, and N. D. Mermin, *Physical Review Letters* **68**, 557 (1992).
- [21] H. J. Briegel, W. Dür, J. I. Cirac, and P. Zoller, *Physical Review Letters* **81**, 5932 (1998).
- [22] N. Gisin, G. Ribordy, W. Tittel, and H. Zbinden, *Reviews of Modern Physics* **74**, 145 (2002).
- [23] H. J. Kimble, *Nature* **453**, 1023 (2008).
- [24] N. Sangouard, C. Simon, J. Minář, H. Zbinden, H. de Riedmatten, and N. Gisin, *Physical Review A* **76**, 50301 (2007).
- [25] C. Santori, D. Fattal, J. Vuckovic, G. S. Solomon, and Y. Yamamoto, *New Journal of Physics* **6**, 89 (2004).
- [26] X. Ding, Y. He, Z. C. Duan, N. Gregersen, M. C. Chen, S. Unsleber, S. Maier, C. Schneider, M. Kamp, S. Höfling, C. Y. Lu, and J. W. Pan, *Physical Review Letters* **116**, 20401 (2016).
- [27] J. Claudon, J. Bleuse, N. S. Malik, M. Bazin, P. Jaffrennou, N. Gregersen, C. Sauvan, P. Lalanne, and J. M. Gérard, *Nature Photonics* **4**, 174 (2010).

- [28] D. Huber, M. Reindl, Y. Huo, H. Huang, J. S. Wildmann, O. G. Schmidt, A. Rastelli, and R. Trotta, *Nature Communications* **8**, 15506 (2017).
- [29] J. Wolters, G. Buser, A. Horsley, L. Béguin, A. Jöckel, J.-P. Jahn, R. J. Warburton, and P. Treutlein, *Physical Review Letters* **119**, 60502 (2017).
- [30] H.-K. Lo, M. Curty, and K. Tamaki, *Nature Photonics* **8**, 595 (2014).
- [31] P. Kok, W. J. Munro, K. Nemoto, T. C. Ralph, J. P. Dowling, and G. J. Milburn, *Reviews of Modern Physics* **79**, 135 (2007).
- [32] J. L. O'Brien, A. Furusawa, and J. Vučković, *Nature Photonics* **3**, 687 (2009).
- [33] M. Müller, H. Vural, C. Schneider, A. Rastelli, O. G. Schmidt, S. Höfling, and P. Michler, *Physical Review Letters* **118**, 257402 (2017).
- [34] R. Loudon, *The Quantum Theory of Light* (Oxford University Press, 2000).
- [35] P. Lodahl, S. Mahmoodian, and S. Stobbe, *Reviews of Modern Physics* **87**, 347 (2015).
- [36] C. Santori, D. Fattal, J. Vučković, G. S. Solomon, E. Waks, and Y. Yamamoto, *Physical Review B* **69**, 205324 (2004).
- [37] C. Santori, M. Pelton, G. Solomon, Y. Dale, and Y. Yamamoto, *Phys. Rev. Lett.* **86**, 1502 (2001).
- [38] C. K. Hong, Z. Y. Ou, and L. Mandel, *Physical Review Letters* **59**, 2044 (1987).
- [39] M. D. Eisaman, J. Fan, A. Migdall, and S. V. Polyakov, *Review of Scientific Instruments* **82**, 71101 (2011).
- [40] W. B. Gao, A. Imamoglu, H. Bernien, and R. Hanson, *Nature Photonics* **9**, 363 (2015).
- [41] B. Hensen, H. Bernien, A. E. Dreau, A. Reiserer, N. Kalb, M. S. Blok, J. Ruitenberg, R. F. L. Vermeulen, R. N. Schouten, C. Abellan, W. Amaya, V. Pruneri, M. W. Mitchell, M. Markham, D. J. Twitchen, D. Elkouss, S. Wehner, T. H. Taminiau, and R. Hanson, *Nature* **526**, 682 (2015).
- [42] D. Riedel, I. Söllner, B. J. Shields, S. Starosielec, P. Appel, E. Neu, P. Maletinsky, and R. J. Warburton, *Physical Review X* **7**, 031040 (2017).

- [43] R. J. Warburton, *Nature Materials* **12**, 483 (2013).
- [44] A. V. Kuhlmann, J. H. Prechtel, J. Houel, A. Ludwig, D. Reuter, A. D. Wieck, and R. J. Warburton, *Nature Communications* **6**, 8204 (2015).
- [45] J. H. Prechtel, A. V. Kuhlmann, J. Houel, A. Ludwig, S. R. Valentin, A. D. Wieck, and R. J. Warburton, *Nature Materials* **15**, 981 (2016).
- [46] S. L. Portalupi, M. Widmann, C. Nawrath, M. Jetter, P. Michler, J. Wrachtrup, and I. Gerhardt, *Nature Communications* **7**, 13632 (2016).
- [47] S. K. Kaushal and G. W. Wetherill, *Journal of Geophysical Research* **75**, 463 (1970).
- [48] S. A. Lourenço, I. F. L. Dias, J. L. Duarte, E. Laureto, E. A. Meneses, and I. Mazzaro, *Journal of Applied Physics* **89**, 61596164 (2001).
- [49] H. Deng, *Science* **298**, 199 (2002).
- [50] C. Heyn, A. Stemmann, T. Köppen, C. Strelow, T. Kipp, M. Grave, S. Mendach, and W. Hansen, *Applied Physics Letters* **94**, 183113 (2009).
- [51] A. Ulhaq, Q. Duan, E. Zallo, F. Ding, O. G. Schmidt, A. I. Tartakovskii, M. S. Skolnick, and E. A. Chekhovich, *Physical Review B* **93**, 165306 (2016).
- [52] C. Heyn, A. Stemmann, and W. Hansen, *Applied Physics Letters* **95**, 173110 (2009).
- [53] Y. H. Huo, A. Rastelli, and O. G. Schmidt, *Applied Physics Letters* **102**, 152105 (2013).
- [54] Z. M. Wang, B. L. Liang, K. A. Sablon, and G. J. Salamo, *Applied Physics Letters* **90**, 113120 (2007).
- [55] P. Michler, *Quantum Dots for Quantum Information Technologies*, edited by P. Michler (Springer, 2018).
- [56] D. Sonnenberg, A. Graf, V. Paulava, W. Hansen, and C. Heyn, *Applied Physics Letters* **101**, 143106 (2012).
- [57] A. Högele, M. Kroner, C. Latta, M. Claassen, I. Carusotto, C. Bulutay, and A. Imamoglu, *Physical Review Letters* **108**, 197403 (2012).
- [58] S. Sanguinetti, K. Watanabe, T. Tateno, M. Wakaki, N. Koguchi, T. Kuroda, F. Minami, and M. Gurioli, *Applied Physics Letters* **81**, 613 (2002).

- [59] K. Karrai, R. J. Warburton, C. Schulhauser, A. Hogele, B. Urbaszek, E. J. McGhee, A. O. Govorov, J. M. Garcia, B. D. Gerardot, and P. M. Petroff, *Nature* **427**, 135 (2004).
- [60] N. Koguchi, K. Ishige, and S. Takahashi, *Journal of Vacuum Science & Technology B* **11**, 787 (1993).
- [61] S. Hunklinger, *Festkörperphysik* (Oldenbourg Verlag, 2007).
- [62] J.-W. Luo, G. Bester, and A. Zunger, *Nanodroplets*, Vol. 18 (Springer, 2013).
- [63] M. Bayer, G. Ortner, O. Stern, A. Kuther, A. A. Gorbunov, A. Forchel, P. Hawrylak, S. Fafard, K. Hinzer, T. L. Reinecke, S. N. Walck, J. P. Reithmaier, F. Klopff, and F. Schäfer, *Physical Review B* **65**, 195315 (2002).
- [64] J. D. Plumhof, V. Křápek, F. Ding, K. D. Jöns, R. Hafenbrak, P. Klenovský, A. Herklotz, K. Dörr, P. Michler, A. Rastelli, and O. G. Schmidt, *Phys. Rev. B* **83**, 121302 (2011).
- [65] A. Rastelli, F. Ding, J. D. Plumhof, S. Kumar, R. Trotta, C. Deneke, A. Malachias, P. Atkinson, E. Zallo, T. Zander, A. Herklotz, R. Singh, V. Křápek, J. R. Schröter, S. Kiravittaya, M. Benyoucef, R. Hafenbrak, K. D. Jöns, D. J. Thurmer, D. Grimm, G. Bester, K. Dörr, P. Michler, and O. G. Schmidt, *Physica Status Solidi (B) Basic Research* **249**, 687 (2012).
- [66] L. Bouet, M. Vidal, T. Mano, N. Ha, T. Kuroda, M. V. Durnev, M. M. Glazov, E. L. Ivchenko, X. Marie, T. Amand, K. Sakoda, G. Wang, and B. Urbaszek, *Applied Physics Letters* **105**, 082111 (2014).
- [67] S. Stobbe, T. W. Schlereth, S. Höfling, A. Forchel, J. M. Hvam, and P. Lodahl, *Phys. Rev. A* **82**, 233302 (2010).
- [68] Y. H. Huo, V. Křápek, A. Rastelli, and O. G. Schmidt, *Phys. Rev. B* **90**, 041304 (2014).
- [69] B. R. Mollow, *Physical Review* **188**, 1969 (1969).
- [70] P. Borri, W. Langbein, S. Schneider, U. Woggon, R. L. Sellin, D. Ouyang, and D. Bimberg, *Physical Review Letters* **87**, 157401 (2001).
- [71] A. Thoma, P. Schnauber, M. Gschrey, M. Seifried, J. Wolters, J. H. Schulze, A. Strittmatter, S. Rodt, A. Carmele, A. Knorr, T. Heindel, and S. Reitzenstein, *Physical Review Letters* **116**, 033601 (2016).

- [72] R. Stockill, M. J. Stanley, L. Huthmacher, E. Clarke, M. Hugues, A. J. Miller, C. Matthiesen, C. Le Gall, and M. Atatüre, *Physical Review Letters* **119**, 10503 (2017).
- [73] A. V. Kuhlmann, J. Houel, A. Ludwig, L. Greuter, D. Reuter, A. D. Wieck, M. Poggio, and R. J. Warburton, *Nature Physics* **9**, 570 (2013).
- [74] J. H. Prechtel, A. V. Kuhlmann, J. Houel, L. Greuter, A. Ludwig, D. Reuter, A. D. Wieck, and R. J. Warburton, *Physical Review X* **3**, 04106 (2014).
- [75] M. Munsch, G. Wüst, A. V. Kuhlmann, F. Xue, A. Ludwig, D. Reuter, A. D. Wieck, M. Poggio, and R. J. Warburton, *Nature Nanotechnology* **9**, 671 (2014).
- [76] M. Kroner, K. M. Weiss, B. Biedermann, S. Seidl, S. Manus, A. W. Holleitner, A. Badolato, P. M. Petroff, B. D. Gerardot, R. J. Warburton, and K. Karrai, *Physical Review Letters* **100**, 156803 (2008).
- [77] J.-P. Jahn, M. Munsch, L. Béguin, A. V. Kuhlmann, M. Renggli, Y. Huo, F. Ding, R. Trotta, M. Reindl, O. G. Schmidt, A. Rastelli, P. Treutlein, and R. J. Warburton, *Physical Review B* **92**, 245439 (2015).
- [78] A. V. Gorshkov, T. Calarco, M. D. Lukin, and A. S. Sørensen, *Physical Review A* **77**, 43806 (2008).
- [79] Y.-F. Hsiao, P.-J. Tsai, H.-S. Chen, S.-X. Lin, C.-C. Hung, C.-H. Lee, Y.-H. Chen, Y.-F. Chen, I. A. Yu, and Y.-C. Chen, *Physical Review Letters* **120**, 183602 (2018).
- [80] M. Fleischhauer and M. D. Lukin, *Physical Review Letters* **84**, 5094 (2000).
- [81] M. D. Lukin, *Reviews of Modern Physics* **75**, 457 (2003).
- [82] C. Heyn, C. Strelow, and W. Hansen, *New Journal of Physics* **14**, 053004 (2012).
- [83] H. S. Nguyen, G. Sallen, C. Voisin, P. Roussignol, C. Diederichs, and G. Cassabois, *Appl. Phys. Lett.* **99**, 261904 (2011).
- [84] C. Matthiesen, A. N. Vamivakas, and M. Atatüre, *Physical Review Letters* **108**, 93602 (2012).
- [85] A. Hogele, S. Seidl, M. Kroner, K. Karrai, R. J. Warburton, B. D. Gerardot, and P. M. Petroff, *Phys. Rev. Lett.* **93**, 217401 (2004).

- [86] A. V. Kuhlmann, J. Houel, D. Brunner, A. Ludwig, D. Reuter, A. D. Wieck, and R. J. Warburton, *Review of Scientific Instruments* **84**, 73905 (2013).
- [87] A. I. Lvovsky, B. C. Sanders, and W. Tittel, *Nature Photonics* **3**, 706 (2009).
- [88] F. Bussi eres, N. Sangouard, M. Afzelius, H. de Riedmatten, C. Simon, and W. Tittel, *Journal of Modern Optics* **60**, 1519 (2013).
- [89] A. G. Radnaev, Y. O. Dudin, R. Zhao, H. H. Jen, S. D. Jenkins, A. Kuzmich, and T. A. B. Kennedy, *Nature Physics* **6**, 894 (2010).
- [90] Y.-H. Chen, M.-J. Lee, I.-C. Wang, S. Du, Y.-F. Chen, Y.-C. Chen, and I. A. Yu, *Phys. Rev. Lett.* **110**, 83601 (2013).
- [91] E. Bimbard, R. Boddeda, N. Vitrant, A. Grankin, V. Parigi, J. Stanojevic, A. Ourjoumtsev, and P. Grangier, *Phys. Rev. Lett.* **112**, 33601 (2014).
- [92] P. S. Michelberger, T. F. M. Champion, M. R. Sprague, K. T. Kaczmarek, M. Barbieri, X. M. Jin, D. G. England, W. S. Kolthammer, D. J. Saunders, J. Nunn, and I. A. Walmsley, *New Journal of Physics* **17**, 43006 (2015).
- [93] M. Lettner, M. M ucke, S. Riedl, C. Vo, C. Hahn, S. Baur, J. Bochmann, S. Ritter, S. D urr, and G. Rempe, *Physical Review Letters* **106**, 210503 (2011).
- [94] B. Darqui e, M. P. A. Jones, J. Dingjan, J. Beugnon, S. Bergamini, Y. Sortais, G. Messin, A. Browaeys, and P. Grangier, *Science* **309**, 454 (2005).
- [95] S. M. Ulrich, S. Weiler, M. Oster, M. Jetter, A. Urvoy, R. L ow, and P. Michler, *Physical Review B* **90** (2014).
- [96] H. M. Meyer, R. Stockill, M. Steiner, C. Le Gall, C. Matthiesen, E. Clarke, A. Ludwig, J. Reichel, M. Atat ure, and M. K ohl, *Physical Review Letters* **114** (2015).
- [97] P. Siyushev, G. Stein, J. Wrachtrup, and I. Gerhardt, *Nature* **509**, 66 (2014).
- [98] N. Akopian, L. Wang, A. Rastelli, O. G. Schmidt, and V. Zwiller, *Nature Photonics* **5**, 230 (2011).
- [99] S. Seidl, M. Kroner, A. Hogele, K. Karrai, R. J. Warburton, A. Badolato, and P. M. Petroff, *Appl. Phys. Lett.* **88**, 203113 (2006).
- [100] S. Kumar, R. Trotta, E. Zallo, J. D. Plumhof, P. Atkinson, A. Rastelli, and O. G. Schmidt, *Appl. Phys. Lett.* **99**, 161118 (2011).

## Bibliography

---

- [101] A. Rastelli, S. Stuffer, A. Schliwa, R. Songmuang, C. Manzano, G. Costantini, K. Kern, A. Zrenner, D. Bimberg, and O. G. Schmidt, *Phys. Rev. Lett.* **92**, 166104 (2004).
- [102] H. S. Nguyen, G. Sallen, C. Voisin, P. Roussignol, C. Diederichs, and G. Cassabois, *Physical Review Letters* **108**, 57401 (2012).
- [103] E. B. Flagg, A. Muller, J. W. Robertson, S. Founta, D. G. Deppe, M. Xiao, W. Ma, G. J. Salamo, and C. K. Shih, *Nature Physics* **5**, 203 (2009).
- [104] M. Bayer and A. Forchel, *Phys. Rev. B* **65**, 41308 (2002).
- [105] P. Michler, A. Imamoglu, M. D. Mason, P. J. Carson, G. F. Strouse, and S. K. Buratto, *Nature* **406**, 968 (2000).
- [106] S. Machlup, *J. Appl. Phys.* **25**, 341 (1954).
- [107] P. Siddons, C. S. Adams, C. Ge, and I. G. Hughes, *Journal of Physics B: Atomic, Molecular and Optical Physics* **41**, 155004 (2008).
- [108] R. J. Warburton, B. T. Miller, C. S. Dürr, C. Bödefeld, K. Karrai, J. P. Kotthaus, G. Medeiros-Ribeiro, P. M. Petroff, and S. Huant, *Phys. Rev. B* **58**, 16221 (1998).
- [109] L. C. Andreani, G. Panzarini, and J.-M. Gérard, *Phys. Rev. B* **60**, 13276 (1999).
- [110] J. R. Guest, T. H. Stievater, X. Li, J. Cheng, D. G. Steel, D. Gammon, D. S. Katzer, D. Park, C. Ell, A. Thränhardt, G. Khitrova, and H. M. Gibbs, *Phys. Rev. B* **65**, 241310 (2002).
- [111] S. Chopra and L. Mandel, *Review of Scientific Instruments* **43**, 1489 (1972).
- [112] M. A. Nielsen and I. L. Chuang, *Quantum computation and quantum information* (Cambridge University Press, 2000).
- [113] P. Kómár, E. M. Kessler, M. Bishof, L. Jiang, A. S. Sørensen, J. Ye, and M. D. Lukin, *Nature Physics* **10**, 582 (2014).
- [114] P. Grangier, B. Sanders, and J. Vuckovic, *New Journal of Physics* **6** (2004).
- [115] N. Sangouard and H. Zbinden, *Journal of Modern Optics* **59**, 1458 (2012).
- [116] L. Mandel, *Optics Letters* **16**, 1882 (1991).
- [117] M. G. Raymer and K. Srinivasan, *Physics Today* **65**, 32 (2012).



- [118] H. de Riedmatten, I. Marcikic, W. Tittel, H. Zbinden, D. Collins, and N. Gisin, *Physical Review Letters* **92**, 47904 (2004).
- [119] A. V. Gorshkov, A. André, M. Fleischhauer, A. S. Sørensen, and M. D. Lukin, *Physical Review Letters* **98**, 123601 (2007).
- [120] S. A. Aljunid, G. Maslennikov, Y. Wang, H. L. Dao, V. Scarani, and C. Kurtsiefer, *Physical Review Letters* **111**, 103001 (2013).
- [121] C. Liu, Y. Sun, L. Zhao, S. Zhang, M. M. T. Loy, and S. Du, *Physical Review Letters* **113**, 133601 (2014).
- [122] X.-H. Bao, Y. Qian, J. Yang, H. Zhang, Z.-B. Chen, T. Yang, and J.-W. Pan, *Physical Review Letters* **101**, 190501 (2008).
- [123] A. Haase, N. Piro, J. Eschner, and M. W. Mitchell, *Optics Letters* **34**, 55 (2009).
- [124] J. Fekete, D. Rieländer, M. Cristiani, and H. de Riedmatten, *Physical Review Letters* **110**, 220502 (2013).
- [125] M. Rambach, A. Nikolova, T. J. Weinhold, and A. G. White, *APL Photonics* **1**, 96101 (2016).
- [126] J. McKeever, A. Boca, A. D. Boozer, R. Miller, J. R. Buck, A. Kuzmich, and H. J. Kimble, *Science* **303** (2004).
- [127] M. Hijlkema, B. Weber, H. P. Specht, S. C. Webster, A. Kuhn, and G. Rempe, *Nature Physics* **3**, 253 (2007).
- [128] P. B. R. Nisbet-Jones, J. Dille, D. Ljunggren, and K. Axel, *New Journal of Physics* **13**, 103036 (2011).
- [129] M. Keller, B. Lange, K. Hayasaka, W. Lange, and H. Walther, *Nature* **431**, 1075 (2004).
- [130] H. G. Barros, A. Stute, T. E. Northup, C. Russo, P. O. Schmidt, and R. Blatt, *New Journal of Physics* **11** (2009).
- [131] M. D. Eisaman, L. Childress, A. André, F. Massou, A. S. Zibrov, and M. D. Lukin, *Physical Review Letters* **93**, 233602 (2004).
- [132] R. T. Willis, F. E. Becerra, L. A. Orozco, and S. L. Rolston, *Optics Express* **19**, 14632 (2011).

- [133] D.-S. Ding, Z.-Y. Zhou, B.-S. Shi, X.-B. Zou, and G.-C. Guo, *Optics Express* **20**, 11433 (2012).
- [134] C. Shu, P. Chen, T. K. A. Chow, L. Zhu, Y. Xiao, M. M. T. Loy, and S. Du, *Nature Communications* **7**, 12783 (2016).
- [135] J. Laurat, H. de Riedmatten, D. Felinto, C.-W. Chou, E. W. Schomburg, and H. J. Kimble, *Optics Express* **14**, 6912 (2006).
- [136] D. N. Matsukevich, T. Chanelière, S. D. Jenkins, S.-Y. Lan, T. A. B. Kennedy, and A. Kuzmich, *Physical Review Letters* **97**, 13601 (2006).
- [137] J. K. Thompson, J. Simon, H. Loh, and V. Vuletić, *Science* **313**, 74 (2006).
- [138] S. Du, P. Kolchin, C. Belthangady, G. Y. Yin, and S. E. Harris, *Physical Review Letters* **100**, 183603 (2008).
- [139] B. Srivathsan, G. K. Gulati, B. Chng, G. Maslennikov, D. Matsukevich, and C. Kertsiefer, *Physical Review Letters* **111**, 123602 (2013).
- [140] L. Zhao, X. Guo, Y. Sun, Y. Su, M. M. T. Loy, and S. Du, *Physical Review Letters* **115**, 193601 (2015).
- [141] P. Farrera, G. Heinze, B. Albrecht, M. Ho, M. Chávez, C. Teo, N. Sangouard, and H. de Riedmatten, *Nature Communications* **7**, 13556 (2016).
- [142] C. Kurz, J. Huwer, M. Schug, P. Müller, and J. Eschner, *New Journal of Physics* **15** (2013).
- [143] G. Fernandez, T. Volz, R. Desbuquois, A. Badolato, and A. Imamoglu, *Physical Review Letters* **103**, 87406 (2009).
- [144] M. T. Rakher and K. Srinivasan, *Applied Physics Letters* **98**, 211103 (2011).
- [145] Y. He, Y. M. He, Y. J. Wei, X. Jiang, M. C. Chen, F. L. Xiong, Y. Zhao, C. Schneider, M. Kamp, S. Höfling, C. Y. Lu, and J. W. Pan, *Physical Review Letters* **111**, 237403 (2013).
- [146] T. M. Sweeney, S. G. Carter, A. S. Bracker, M. Kim, C. S. Kim, L. Yang, P. M. Vora, P. G. Brereton, E. R. Cleveland, and D. Gammon, *Nature Photonics* **8**, 442 (2014).
- [147] J. P. Lee, L. M. Wells, B. Villa, S. Kalliakos, R. M. Stevenson, D. J. P. Ellis, I. Farrer, D. A. Ritchie, A. J. Bennett, and A. J. Shields, *Quantum Science and Technology* **3**, 024008 (2018).

- [148] M. Almendros, J. Huwer, N. Piro, F. Rohde, C. Schuck, M. Hennrich, F. Dubin, and J. Eschner, *Physical Review Letters* **103**, 213601 (2009).
- [149] P. Müller, T. Tentrup, M. Bienert, G. Morigi, and J. Eschner, *Physical Review A* **96**, 23861 (2017).
- [150] A. Delteil, Z. Sun, W.-B. Gao, E. Togan, S. Faelt, and A. Imamoglu, *Nature Physics* **12**, 218 (2016).
- [151] D. J. Saunders, J. H. D. Munns, T. F. M. Champion, C. Qiu, K. T. Kaczmarek, E. Poem, P. M. Ledingham, I. A. Walmsley, and J. Nunn, *Physical Review Letters* **116**, 90501 (2016).
- [152] M. Atatüre, J. Dreiser, A. Badolato, A. Högele, K. Karrai, and A. Imamoglu, *Science* **312**, 551 (2006).
- [153] B. D. Gerardot, D. Brunner, P. A. Dalgarno, P. Ohberg, S. Seidl, M. Kroner, K. Karrai, N. G. Stoltz, P. M. Petroff, and R. J. Warburton, *Nature* **451**, 441 (2008).
- [154] C.-Y. Lu, Y. Zhao, A. N. Vamivakas, C. Matthiesen, S. Fält, A. Badolato, and M. Atatüre, *Physical Review B* **81**, 35332 (2010).
- [155] J. Brendel, N. Gisin, W. Tittel, and H. Zbinden, *Physical Review Letters* **82**, 2594 (1999).
- [156] I. Marcikic, H. de Riedmatten, W. Tittel, V. Scarani, H. Zbinden, and N. Gisin, *Physical Review A* **66**, 62308 (2002).
- [157] P. C. Humphreys, B. J. Metcalf, J. B. Spring, M. Moore, X.-M. Jin, M. Barbieri, W. S. Kolthammer, and I. A. Walmsley, *Physical Review Letters* **111**, 150501 (2013).
- [158] H. Jayakumar, A. Predojević, T. Kauten, T. Huber, G. S. Solomon, and G. Weihs, *Nature Communications* **5**, 4251 (2014).
- [159] H. S. Nguyen, G. Sallen, M. Abbarchi, R. Ferreira, C. Voisin, P. Roussignol, G. Cassabois, and C. Diederichs, *Phys. Rev. B* **87**, 115305 (2013).
- [160] X. Li, H. Nakayama, and Y. Arakawa, *Phys. Rev. B* **59**, 5069 (1999).
- [161] Y. Toda, O. Moriwaki, M. Nishioka, and Y. Arakawa, *Physical Review Letters* **82**, 4114 (1999).
- [162] A. Kiraz, M. Atatüre, and A. Imamoglu, *Phys. Rev. A* **69**, 32301 (2004).

- [163] M. N. Makhonin, J. E. Dixon, R. J. Coles, B. Royall, I. J. Luxmoore, E. Clarke, M. Hugues, M. S. Skolnick, and A. M. Fox, *Nano Letters* **14**, 6997 (2014).
- [164] A. Zrenner, E. Beham, S. Stuffer, F. Findeis, M. Bichler, and G. Abstreiter, *Nature* **418**, 612 (2002).
- [165] T. H. Stievater, X. Li, D. G. Steel, D. Gammon, D. S. Katzer, D. Park, C. Piermarocchi, and L. J. Sham, *Physical Review Letters* **87**, 133603 (2001).
- [166] H. Kamada, H. Gotoh, J. Temmyo, T. Takagahara, and H. Ando, *Physical Review Letters* **87**, 246401 (2001).
- [167] P. Tighineanu, R. Daveau, E. H. Lee, J. D. Song, S. Stobbe, and P. Lodahl, *Phys. Rev. B* **88**, 155320 (2013).
- [168] I. Aharonovich, D. Englund, and M. Toth, *Nat Photon* **10**, 631 (2016).
- [169] M. Grundmann and D. Bimberg, *Physical Review B* **55**, 9740 (1997).
- [170] J. Gomis-Bresco, G. Muñoz-Matutano, J. Martínez-Pastor, B. Alén, L. Seravalli, P. Frigeri, G. Trevisi, and S. Franchi, *New Journal of Physics* **13** (2011).
- [171] G. Wang, S. Fafard, D. Leonard, J. E. Bowers, J. L. Merz, and P. M. Petroff, *Applied Physics Letters* **64**, 2815 (1994).
- [172] D. Morris, N. Perret, and S. Fafard, *Applied Physics Letters* **75**, 3593 (1999).
- [173] T. Mano, M. Abbarchi, T. Kuroda, C. A. Mastrandrea, A. Vinattieri, S. Sanguinetti, K. Sakoda, and M. Gurioli, *Nanotechnology* **20**, 395601 (2009).
- [174] C. Heyn, M. Zocher, L. Pudewill, H. Runge, A. Küster, and W. Hansen, *Journal of Applied Physics* **121**, 044306 (2017).
- [175] J. Houel, A. V. Kuhlmann, L. Greuter, F. Xue, M. Poggio, R. J. Warburton, B. D. Gerardot, P. A. Dalgarno, A. Badolato, P. M. Petroff, A. Ludwig, D. Reuter, and A. D. Wieck, *Physical Review Letters* **108**, 107401 (2012).
- [176] F. Ding, R. Singh, J. D. Plumhof, T. Zander, V. Křápek, Y. H. Chen, M. Benyoucef, V. Zwiller, K. Dörr, G. Bester, A. Rastelli, and O. G. Schmidt, *Physical Review Letters* **104**, 067405 (2010).
- [177] X. Yuan, F. Weihausen-brinkmann, J. Martín-Sánchez, G. Piredda, K. Vlastimil, Y. Huo, H. Huang, C. Schimpf, O. G. Schmidt, J. Edlinger, G. Bester, R. Trotta, and A. Rastelli, *arXiv:1710.03962*, 1 (2017).

- [178] E. Ramsay, *Journal of Nanophotonics* **2**, 021854 (2008).
- [179] C. W. Hicks, D. O. Brodsky, E. A. Yelland, A. S. Gibbs, J. A. N. Bruin, M. E. Barber, S. D. Edkins, K. Nishimura, S. Yonezawa, Y. Maeno, and A. P. Mackenzie, *Science* **344**, 283 (2014).
- [180] C. W. Hicks, M. E. Barber, S. D. Edkins, D. O. Brodsky, and A. P. Mackenzie, *Review of Scientific Instruments* **85**, 065003 (2014).
- [181] Y. H. Huo, B. J. Witek, S. Kumar, J. R. Cardenas, J. X. Zhang, N. Akopian, R. Singh, E. Zallo, R. Grifone, D. Kriegner, R. Trotta, F. Ding, J. Stangl, V. Zwiller, G. Bester, A. Rastelli, and O. G. Schmidt, *Nature Physics* **10**, 46 (2013).
- [182] J. M. Smith, P. A. Dalgarno, R. J. Warburton, A. O. Govorov, K. Karrai, B. D. Gerardot, and P. M. Petroff, *Physical Review Letters* **94**, 197402 (2005).
- [183] F. Langer, D. Plischke, M. Kamp, and S. Höfling, *Applied Physics Letters* **105**, 081111 (2014).
- [184] M. C. Löbl, I. Söllner, A. Javadi, T. Pregnolato, R. Schott, L. Midolo, A. V. Kuhlmann, S. Stobbe, A. D. Wieck, P. Lodahl, A. Ludwig, and R. J. Warburton, *Physical Review B* **96**, 165440 (2017).
- [185] E. Muñoz, E. Calleja, I. Izpura, F. García, A. L. Romero, J. L. Sánchez-Rojas, A. L. Powell, and J. Castagné, *Journal of Applied Physics* **73**, 4988 (1993).
- [186] A. M. Fox, *Quantum Optics* (Oxford University Press, 2006).
- [187] K. H. Madsen, S. Ates, J. Liu, A. Javadi, S. M. Albrecht, I. Yeo, S. Stobbe, and P. Lodahl, *Phys. Rev. B* **90**, 155303 (2014).
- [188] L. Sapienza, M. Davanço, A. Badolato, and K. Srinivasan, *Nature Communications* **6**, 7833 (2015).
- [189] L. Greuter, S. Starosielec, D. Najer, A. Ludwig, L. Duempelmann, D. Rohner, and R. J. Warburton, *Applied Physics Letters* **105**, 121105 (2014).
- [190] M. Gschrey, A. Thoma, P. Schnauber, M. Seifried, R. Schmidt, B. Wohlfeil, L. Krüger, J. H. Schulze, T. Heindel, S. Burger, F. Schmidt, A. Strittmatter, S. Rodt, and S. Reitzenstein, *Nature Communications* **6**, 8662 (2015).
- [191] W. Nagourney, *Quantum Electronics for Atomic Physics* (Oxford University Press, 2010).

*Bibliography*

---

- [192] R. J. Barbour, P. A. Dalgarno, A. Curran, K. M. Nowak, H. J. Baker, D. R. Hall, N. G. Stoltz, P. M. Petroff, and R. J. Warburton, *Journal of Applied Physics* **110**, 053107 (2011).
- [193] L. Greuter, S. Starosielec, A. V. Kuhlmann, and R. J. Warburton, *Phys. Rev. B* **92**, 045302 (2015).
- [194] D. Najer, M. Renggli, D. Riedel, S. Starosielec, and R. J. Warburton, *Applied Physics Letters* **110**, 011101 (2017).
- [195] I. Shomroni, S. Rosenblum, Y. Lovsky, O. Bechler, G. Guendelman, and B. Dayan, *Science* **345**, 903 (2014).
- [196] I. Söllner, L. Midolo, and P. Lodahl, *Physical Review Letters* **116**, 234301 (2016).
- [197] S. Stobbe, J. Johansen, P. T. Kristensen, J. M. Hvam, and P. Lodahl, *Phys. Rev. B* **80**, 155307 (2009).

# Acknowledgements

First and foremost I would like to thank Prof. Richard Warburton for giving me the opportunity to work on such an exciting and versatile project. There were always challenges to tackle and his support and the long discussion were invaluable for the success of the project. I want to thank Prof. Armando Rastelli for taking the time to assess the thesis as the co-referee and of course for providing us with exceptional quantum dots. I cannot stress enough how important the quality of the samples was for the successful development over the last years. Furthermore, I would like to thank Prof. Philipp Treutlein for important input on the experiment and the papers, as well as “lending” me one of his post-docs to join me in the lab.

I owe a big thank you to Lucas Béguin, who spent a lot of time with me in the lab measuring, whilst listening to all kinds of music and singing along. Thank you for patiently teaching me a lot and for playing a quick round of Hanabi in between late-night measurements. Thanks to Mathieu Munsch for the guidance especially in the beginning, as well as always having time to discuss. Janik Wolters, thank you for building up the atomic memory for the project and still finding time to greatly contribute to our work on the quantum dot. I have to thank the entire group for always having time to give a helping hand, discuss data, grab a coffee or a beer later in the evening. The great group dynamic creates an awesome working environment, even when work got stressful sometimes.

I want to thank my family, who got me interested in science early on, always encouraging the pursuit of curiosity and supporting me unconditionally. Most of all, I would like to thank my wife Elli for being incredibly patient and understanding with me, especially in the last few months. Your support was vital to this endeavor.

## Contributions to publications

During this thesis, contributions to the following articles were made:

1. J.-P. Jahn, M. Munsch, L. Béguin, , A.V. Kuhlmann, M. Renggli, Y.Huo, F. Ding, R. Trotta, M. Reindl, O.G. Schmidt, A. Rastelli, P. Treutlein, R.J. Warburton. *An artificial Rb atom in a semiconductor with lifetime-limited linewidth*. Phys. Rev. B **92**, 245439 (2015)
2. J. Wolters, G. Buser, A. Horsley, L. Béguin, A. Jöckel, J.-P. Jahn, R.J. Warburton, P. Treutlein.  
*Simple Atomic Quantum Memory Suitable for Semiconductor Quantum Dot Single Photons*  
Phys. Rev. Lett. **119**, 060502 (2017)
3. L. Béguin, J.-P. Jahn, J. Wolters, M. Reindl, Y. Huo, R. Trotta, A. Rastelli, F. Ding, O.G. Schmidt, P. Treutlein, R.J. Warburton. *On-demand semiconductor source of 780 nm single photons with controlled temporal wave packets*. Phys. Rev. B **97**, 205304 (2018)



# Curriculum vitae

## Jan-Philipp Jahn

### Personal information

Mailing address: Eptingerstrasse 17, 4052 Basel, Switzerland  
Email address: JanPhilippJahn@gmail.com  
Date of birth: 14th April 1986  
Place of birth: Goslar, Germany  
Citizenship: German

### Education

2013 – 2018 **PhD in Experimental Physics**  
University of Basel, Switzerland  
Thesis: *An Artificial Rubidium Atom*  
Advisor: Prof. Richard J. Warburton

2010 – 2017 **Bachelor studies of Economics**  
FernUniversität Hagen, Germany  
Bachelor thesis: *Tendering processes for funding of renewable energies in Germany*  
Advisor: Prof. Alfred Endres

2006 – 2012 **Diploma studies in Physics**  
Julius-Maximilians University Würzburg, Germany  
Thesis: *Electric excitation of exciton-polaritons in semiconductor microcavities*  
Advisor: Prof. Martin Kamp

1998 – 2005 **Abitur**  
Werner-von-Siemens Gymnasium Bad Harzburg, Germany